UNIVERSIDADE FEDERAL DE SÃO CARLOS – CAMPUS SOROCABA
CENTRO DE CIÊNCIAS E TECNOLOGIAS PARA SUSTENTABILIDADE – CCTS
DEPARTAMENTO DE FÍSICA, QUIMICA E MATEMÁTICA – DFQM

Antonio Said Webbe Sales

Effects of Radiation on Zircon Mineral: Characterization via Micro-Raman Spectroscopy and Small-Angle X-ray Scattering (SAXS)

Sorocaba
2026

Antonio Said Webbe Sales

Effects of Radiation on Zircon Mineral: Characterization via Micro-Raman Spectroscopy and Small-Angle X-ray Scattering (SAXS)

Doctoral Thesis submitted to the Programa de Pós-Graduação em Ciência dos Materiais to obtain the title of Doctor of Materials Science from the Federal University of São Carlos.

Advisor: Prof. Dr. Airton Natanael Coelho Dias
Co-advisor: Prof. Dr. Sandro de Oliveira Guedes
Funding: Coordenação de Aperfeiçoamento de Pessoal de Nível Superior – Brasil (CAPES) – FinanceCode 001

Sorocaba
2026

Sales, Antonio Said Webbe

Effects of Radiation on Zirconium Mineral::
Characterization via Micro-Raman Spectroscopy and
Small-Angle X-ray Scattering (SAXS) / Antonio Said
Webbe Sales -- 2026.
114f.

Tese (Doutorado) - Universidade Federal de São Carlos,
campus Sorocaba, Sorocaba
Orientador (a): Airton Natanael Coelho Dias
Banca Examinadora: Marystela Ferreira, Renato
Fernandes Cantão, Cleber Jose Soares, Matheus Rufino
Bibliografia

1. Generalized Additive Models. 2. Thermochronology. 3.
Raman spectroscopy. I. Sales, Antonio Said Webbe. II.
Título.

Ficha catalográfica desenvolvida pela Secretaria Geral de Informática
(SIn)

DADOS FORNECIDOS PELO AUTOR

Bibliotecário responsável: Maria Aparecida de Lourdes Mariano -
CRB/8 6979

APPROVAL SHEET
(FOLHA DE APROVAÇÃO)

Antonio Said Webbe Sales

Effects of Radiation on Zirconium Mineral: Characterization via Micro-Raman Spectroscopy and Small-Angle X-ray Scattering (SAXS)

Doctoral Thesis presented to the Programa de Pós-Graduação em Ciência dos Materiais to obtain the title of Doctor of Materials Science from the Federal University of São Carlos. Sorocaba, March 10, 2026.

Advisor

____
Prof. Dr. Airton Natanael Coelho Dias
CCTS/DFQM, UFSCar, campus Sorocaba

Co-advisor

____
Prof. Dr. Sandro de Oliveira Guedes
IFGW, UNICAMP

Thesis Committee

____
Prof. Dra. Marystela Ferreira
CCTS/DFQM, UFSCar, campus Sorocaba

____
Prof. Dr. Renato Fernandes Cantão
CCTS/DFQM, UFSCar, campus Sorocaba

____
Dr. Cleber José Soares
Chronuscamp Research

____
Dr. Matheus Rufino
IFGW, UNICAMP

Aos meus alicerces e ao meu fruto:
Ao meu pai, José Maria Sales *(in memoriam)*. A tua presença se faz mais forte na ausência. Esta tese é escrita com a memória das tuas mãos, que me ensinaram o valor do trabalho, e com a saudade da tua voz, que sempre acreditou nos meus passos mesmo quando eu duvidava deles. Onde quer que esteja esta conquista também é tua regada pelas lágrimas da tua partida em 25 de setembro de 2022 e pelo orgulho que sempre sentiste.És minha eterna estrela-guia.
À minha mãe, Saide Webbe Sales, a fortaleza que nunca me deixou cair. O teu colo foi o refúgio nos dias tempestuosos, e a tua fé inabalável foi o vento que me trouxe até aqui. Esta caminhada é tão minha quanto tua bordada com o fio do teu amor incondicional e da tua incansável dedicação.
À minha filha, Samia Webbe Sales, a razão do meu amanhã. Que um dia, ao olhares para estas páginas, compreendas que os sonhos se constroem um passo de cada vez, e que o conhecimento é a herança mais bela que podemos deixar. Este trabalho é a prova de que tudo é possível quando se tem amor. Para ti, para que vejas no meu caminho a coragem para trilhares o teu.

AGRADECIMENTO

Este trabalho é fruto de uma caminhada que não teria sido possível sem o apoio, a confiança e a generosidade de pessoas fundamentais, a quem registro minha mais profunda gratidão.

Ao meu orientador, Prof. Dr. Airton Natanael Coelho Dias, expresso minha sincera admiração e reconhecimento. Sua orientação precisa, paciência incansável e visão crítica foram faróis nos momentos de incerteza. Obrigado por acreditar no potencial deste trabalho e por me guiar com sabedoria, sempre respeitando minhas ideias e me desafiando a ir além.

Ao meu coorientador, Prof. Dr. Sandro Guedes, minha gratidão pela disponibilidade constante e pelas contribuições valiosas que enriqueceram esta pesquisa. Sua experiência e olhar atento foram essenciais para lapidar os rumos do estudo, e sua generosidade acadêmica tornou esta jornada mais leve e produtiva.

Ao Prof. Renato Cantão, agradeço de forma especial pelo auxílio fundamental na minha transição da linguagem C para o Python. Partindo do meu conhecimento prévio em programação na linguagem C, sua orientação foi crucial para que eu pudesse migrar de forma segura e eficiente para um paradigma de mais alto nível, compreendendo as potencialidades e os novos horizontes que o Python abria para as análises desta pesquisa. Sua paciência para ensinar e seu conhecimento técnico foram a ponte que conectou minha base em C às possibilidades dinâmicas do Python, ampliando não apenas este trabalho, mas também minhas habilidades como pesquisador.

Ao Prof. Térsio Guilherme de Souza Cruz, meu sincero agradecimento por ter gentilmente emprestado o computador utilizado para a programação e a escrita desta tese e dos artigos decorrentes. Esse apoio foi indispensável para a realização deste trabalho.

A todos os professores, funcionários e à coordenação do programa, meu muito obrigado pelo ambiente acolhedor, pela formação de excelência e pelo compromisso em manter o curso sempre no mais alto nível.

À minha família – minha mãe Saide, meu pai José Maria *(in memoriam)* e minha filha Samia – agradeço por serem a razão e o alicerce de tudo. Vocês transformaram esta caminhada em propósito.

Por fim, este estudo foi realizado com apoio da Coordenação de Aperfeiçoamento de Pessoal de Nível Superior – Brasil (CAPES) – Código de Financiamento 001. Meu reconhecimento ao investimento público na ciência e na educação, fundamentais para o avanço do conhecimento em nosso país.

“Look at the resplendent colours on the soap
bubbles! Why is the sea blue? What makes
diamond glitter?“
C. V. Raman

RESUMO

SALES, Antonio Said Webbe. EFEITOS DA RADIAÇÃO NO MINERAL ZIRCÃO: CARACTERIZAÇÃO VIA ESPECTROSCOPIA MICRO-RAMAN E ESPALHAMENTO DE RAIOS X A BAIXOS ÂNGULOS (SAXS). 2026. Tese de Doutorado em Ciências dos Materiais obtido junto Programa de Pós-Graduação em Ciência dos Materiais – Universidade Federal de São Carlos, Sorocaba, 2026.

O dano de radiação em zircão ($ZrSiO_4$) compromete fundamentalmente sua confiabilidade como geocronômetro ao alterar a estrutura cristalina através do acúmulo de danos por recuo alfa provenientes do decaimento de urânio e tório. Esta tese apresenta uma investigação integrada da avaliação de danos de radiação, comportamento de *annealing* e morfologia de traços em nanoescala em zircão, empregando técnicas analíticas complementares e metodologias estatísticas avançadas para estabelecer protocolos robustos para aplicações de termocronologia baseada em Raman. O primeiro componente aborda uma lacuna metodológica crítica no pré-processamento de espectroscopia Raman para quantificação de danos de radiação. Doze combinações de pré-processamento foram sistematicamente avaliadas em seis modos vibracionais utilizando 80 espectros de zircão de amostras com dano de radiação. A avaliação de desempenho empregou métricas de qualidade de ajuste e validação estatística com protocolos de detecção de outliers, comparando três algoritmos de correção de linha de base (polinomial, spline e AirPLS iterativo) combinados com quatro métodos de normalização (min-max, área, pico e vetor). Os resultados demonstram que a eficácia do pré-processamento é altamente dependente do modo: o modo de estiramento simétrico $\nu_3(SiO_4)$ em 1008 cm^{-1} alcançou qualidade de ajuste e precisão superiores com correção de linha de base spline e normalização Min-Max, enquanto os modos vibracionais ν_1 e $\nu_2(SiO_4)$ apresentaram desempenho ótimo com correção de linha de base Polinomial e normalização por área. Esses achados estabelecem protocolos de pré-processamento padronizados que aprimoram a comparabilidade interlaboratorial e a precisão analítica para aplicações de geocronologia U-Pb. O segundo componente investiga a dinâmica de recuperação cristalina durante o *annealing* isotérmico de zircão metamíctico através de espectroscopia Raman e modelagem estatística avançada. Um conjunto de dados de 6.225 observações espectrais válidas foi analisado utilizando Modelos Aditivos Generalizados (GAM), regressão segmentada com otimização por Evolução Diferencial e métodos *bootstrap* pareados para testar seis hipóteses fundamentais. Os resultados confirmam a superioridade de modelos não-lineares e revelam uma recuperação bifásica caracterizada por uma fase inicial (Estágios I-II, 473-840 K) com recuperação preferencial de modos externos e maior variabilidade (razão CV = 1,56), seguida por uma fase final (Estágio III) onde os modos tetraédricos SiO_4 dominam e a variabilidade converge (razão CV = 0,92). Pontos de inflexão empíricos em 607 K e 840 K validam o modelo fenomenológico de três estágios de Geisler, enquanto a análise *bootstrap* revela comportamento não-monotônico nas razões de área de banda com um pico em 622 K. Essas restrições quantitativas fornecem uma base para termocronologia de baixa temperatura baseada em Raman. O terceiro componente integra medidas de Espalhamento de Raios-X a Baixo Ângulo (SAXS) para caracterizar a morfologia de traços iônicos em nanoescala em zircão irradiado por íons pesados rápidos. A análise SAXS utilizando o modelo de cilindro rígido com polidispersidade Gaussiana resultou em raios de traço variando de 3,32 a 4,99 nm em sete amostras. A correlação entre parâmetros de traço SAXS e FWHM Raman não é simplesmente linear: a amostra com maior raio de traço (4,99 nm) apresenta o menor FWHM (7,38 cm^{-1}), enquanto a amostra de menor raio (3,32 nm) exibe FWHM de 13,05 cm^{-1}, indicando que raios de traço reduzidos não implicam necessariamente menor desordem vibracional. Esse comportamento reflete o fato de que as duas técnicas respondem a aspectos distintos do dano estrutural — desordem vibracional de curto alcance e morfologia física dos cilindros de dano em nanoescala, respectivamente — com implicações diretas para a calibração de parâmetros Raman em termocronologia de traços de fissão. Em conjunto, os protocolos de pré-processamento Raman, a modelagem estatística da cinética de recuperação e a caracterização estrutural por SAXS oferecem um ponto de partida para a padronização da análise Raman de zircão em contextos termocronológicos, embora sua generalização dependa de validação com conjuntos de dados independentes e composições químicas variadas. Cabe registrar que a Microscopia Eletrônica de Transmissão (TEM), prevista no escopo original e mencionada no título, não pôde ser realizada em razão do não retorno das amostras encaminhadas ao *Australian Synchrotron* para a caracterização SAXS; os resultados obtidos por Espectroscopia Raman e SAXS não são afetados por essa ausência.

Palavras-chave: zircão, dano de radiação, espectroscopia Raman, recozimento térmico, SAXS, termocronologia, metamitização, otimização de pré-processamento

ABSTRACT

SALES, Antonio Said Webbe. Effects of Radiation on Zirconium Mineral: Characterization via Micro-Raman Spectroscopy and Small-Angle X-ray Scattering (SAXS). 2026. Doctoral Thesis, Programa de Pós-Graduação em Ciência dos Materiais to obtain the title of Doctor of Materials Science from the Federal University of São Carlos. Sorocaba, 2026.

Radiation damage in zircon ($ZrSiO_4$) fundamentally compromises its reliability as a geochronometer by altering the crystalline structure through accumulation of α-recoil damage from uranium and thorium decay. This thesis presents an integrated investigation of radiation damage assessment, thermal annealing behavior, and nanoscale track morphology in zircon, employing complementary analytical techniques and advanced statistical methodologies to establish robust protocols for Raman-based thermochronology applications. The first component addresses a critical methodological gap in Raman spectroscopy preprocessing for radiation damage quantification. Twelve preprocessing combinations were systematically evaluated across six vibrational modes using 80 zircon spectra from radiation-damaged samples. Performance assessment employed fitting quality metrics and statistical validation with outlier detection protocols, algorithms (polynomial, spline, and comparing three baseline correction iterative AirPLS) combined with four normalization methods (min-max, area, peak, and vector). Results demonstrate that preprocessing effectiveness is highly mode-dependent: the $\nu_3(SiO_4)$ symmetric stretching mode at 1008 cm^{-1} achieved superior fitting quality and precision with Spline baseline correction and Min-Max normalization, while ν_1 and $\nu_2(SiO_4)$ vibrational modes performed optimally with Polynomial baseline correction and area normalization. These findings establish standardized preprocessing protocols that enhance inter-laboratory comparability and analytical precision for U-Pb geochronology applications. The second component investigates crystalline recovery dynamics during isothermal annealing of metamict zircon through Raman spectroscopy and advanced statistical modeling. A dataset of 6,225 valid spectral observations was analyzed using Generalized Additive Models (GAM), segmented regression with Differential Evolution optimization, and paired bootstrap methods to test six fundamental hypotheses. Results confirm non-linear model superiority and reveal a two-phase recovery characterized by an initial phase (Stages I-II, 473-840 K) with preferential external mode recovery and higher variability (CV ratio = 1.56), followed by a final phase (Stage III) where SiO_4 tetrahedral modes dominate and variability converges (CV ratio = 0.92). Empirical breakpoints at 607 K and 840 K validate Geisler's three-stage phenomenological model, while bootstrap analysis reveals non-monotonic behavior in band area ratios with a peak at 622 K. These quantitative constraints provide a foundation for Raman-based low-temperature thermochronology. The third component integrates Small-Angle X-ray Scattering (SAXS) measurements to characterize nanoscale ion track morphology in swift heavy-ion irradiated zircon. SAXS analysis using the hard cylinder model with Gaussian polydispersity yielded track radii ranging from 3.32 to 4.99 nm across seven samples. The correlation between SAXS track parameters and Raman FWHM is not simply linear: the sample with the largest track radius (4.99 nm) exhibits the lowest FWHM (7.38 cm^{-1}), whereas the sample with the smallest radius (3.32 nm) presents a FWHM of 13.05 cm^{-1}, indicating that reduced track radii do not necessarily imply lower vibrational disorder. This behavior reflects the fact that the two techniques respond to structurally distinct aspects of radiation damage — short-range vibrational disorder and physical nanoscale track morphology, respectively — with direct implications for the calibration of Raman parameters in fission track thermochronology. Taken together, the standardized Raman preprocessing protocols, statistical modeling of recovery kinetics, and structural characterization by SAXS offer a starting point for the standardization of Raman-based zircon analysis in thermochronological contexts, although their generalization depends on validation with independent datasets and varied chemical compositions. It should be noted that Transmission Electron Microscopy (TEM), included in the original research scope and reflected in the title, could not be performed due to the non-return of samples sent to the Australian Synchrotron for SAXS characterization, which also precluded the TEM stage; this absence does not affect the results obtained by Raman spectroscopy and SAXS.

Keywords: zircon, radiation damage, Raman spectroscopy, thermal annealing, SAXS, thermochronology, metamictization, preprocessing optimization

LIST OF FIGURES

LIST OF TABLES

LIST OF SUPPLEMENTARY TABLES

LIST OF ABBREVIATIONS AND ACRONYMS

AIC – Akaike Information Criterion

AirPLS – Adaptive Iterative Penalized Least Squares

ANCOVA – Analysis of Covariance

ANN – Annealed Sample

BP – Breakpoint

CCD – Charge-Coupled Device

CI – Confidence Interval

CTS – Core Transition Shell

CV – Coefficient of Variation

D-Optimal – D-Optimal Design (of experiments)

DSC – Differential Scanning Calorimetry

Ea – Activation Energy

ECDF – Empirical Cumulative Distribution Function

EDOF – Effective Degrees of Freedom

ExtRot – External Rotation Mode

GAM – Generalized Additive Model

GCV – Generalized Cross-Validation

IQR – Interquartile Range

MCMC – Markov Chain Monte Carlo

Q1 – First Quartile

Q3 – Third Quartile

ST – Sample (raw, untreated sample)

UFSCar – Universidade Federal de São Carlos (Federal University of São Carlos)

UNESP – Universidade Estadual Paulista (São Paulo State University)

UNICAMP – Universidade Estadual de Campinas (University of Campinas)

TABLE OF CONTENTS

1INTRODUCTION

The understanding of geological and thermochronological processes has advanced significantly using radiometric dating methods, among which Fission Track thermochronology (FT) stands out. This method exploits the spontaneous fission of uranium (U) and thorium (Th) isotopes in minerals containing these elements, such as zircon, apatite, epidote, monazite, etc., to date geological events (e.g, Green et al., 1986; Crowley et al., 1991; Kohn et al., 2024; Gleadow et al. 2002; Osório et al., 2002; Barbarand et al., 2003; Dias et al., 2009;Sales et al., 2023). The basis of FT lies in the ability of fission tracks, resulting from the disintegration of U isotopes, to record thermal events throughout the geological history of a sample.

Over the decades, FT has evolved significantly with advances in analytical technologies, enabling a deeper understanding of terrestrial processes and the chronology of geological events. A mineral that occupies a central position in this context is zircon ($ZrSiO_4$), whose unique properties make it a tool for deciphering Earth's geological history.

The progressive accumulation of alpha-recoil damage from uranium and thorium decay progressively disorders the crystalline lattice of zircon ($ZrSiO_4$), causing systematic broadening and shifting of its Raman vibrational bands (Murakami et al., 1991; Nasdala et al., 1995; Zhang, Salje, et al., 2000; Ewing et al., 2003). Because parameters such as the full width at half maximum (FWHM) of the $\nu_3(SiO_4)$ band serve as proxies for radiation dose and thermal history in Raman-based thermochronology(Nasdala et al., 2003; Ginster et al., 2019; Anderson et al., 2020; Härtel et al., 2021), a precise understanding of how radiation damage is structurally expressed – and how it recovers during geological or laboratory annealing – is critical for accurate age and thermal-history interpretations(Capitani et al., 2000; Geisler, 2002; Ewing et al., 2003; Pidgeon et al., 2017).

However, the physical mechanisms that link crystalline recovery to the spectral response of different vibrational modes remain incompletely constrained (Capitani et al., 2000; Nasdala et al., 2001; Geisler, 2002; Ginster et al., 2019; Härtel et al., 2021). In particular, the differential behaviour of internal tetrahedral (SiO_4) modes and external lattice (rotational) modes during isothermal annealing lacks quantitative characterization (Zhang, Salje, et al., 2000; Geisler et al., 2001; Dias et al., 2020; Härtel et al., 2022). Without a mechanistic understanding of this response, calibrations of Raman thermometers necessarily rest on empirical correlations whose physical basis is unclear, limiting both the accuracy and the inter-laboratory reproducibility of Raman-based thermochronology (Nasdala et al., 2003; Anderson et al., 2020; Resentini et al., 2020; Härtel et al., 2024).

This thesis addresses that gap through an integrated experimental investigation of radiation damage and thermal recovery in zircon, employing micro-Raman spectroscopy, small-angle X-ray scattering (SAXS), and supporting statistical modelling. The specific objectives are to (i) develop and validate mode-specific spectral preprocessing protocols that minimize analytical variability, (ii) characterize the non-linear recovery trajectories of internal and external vibrational modes during isothermal annealing, and (iii) correlate nanoscale damage morphology (from SAXS) with vibrational disorder to better constrain the physical basis of Raman thermochronometers.

Characterization via micro-Raman spectroscopy and SAXS (Small-Angle X-ray Scattering) contributes to understanding the mechanisms of radiation-induced damage and recovery in the zircon structure. With this, it is understood that improving the annealing models of fission tracks enables a more accurate interpretation of the thermal history of the samples and, by extension, a better understanding of the geological processes that shape the Earth.

The tetragonal structure of zircon facilitates the isotopic substitution of Zr^{4+} by radioactive elements such as uranium (U) and thorium (Th), a process that yields radiogenic lead (Pb) isotopes over extended geological periods. The self-irradiation from the alpha decay of these elements can cause metamictization of zircon, transforming its crystalline structure into an amorphous state and significantly altering its physical and chemical properties. This phenomenon, initially documented by Dawson, Hargreave, and Wilkinson (1971), serves as a prelude to the complexity of zircon, both in its constitution and its applicability in thermochronological studies.

This work also examines recent innovations in the application of Raman spectroscopy to zircon dating, highlighting the significant potential of this technique to advance the frontiers of geochronology. Contemporary research, exemplified by the work of Anderson et al. (2020) and Resentini et al. (2020), has revealed an empirical correlation between Raman bandwidth and alpha doses, originating from U and Th concentrations, thereby facilitating the quantification of radiation damage and the estimation of zircon ages. In addition, the contributions of Härtel et al. (2021), Shchapova, Krylov, and Votyakov (2023), and others, who expanded the understanding of the impact of radiation damage on zircon and its implications for thermochronology, were explored. The integration of methods such as Raman dating and (U-Th)/He, as discussed by Härtel et al. (2024), enhances understanding of the thermal history of samples and represents a significant advance in zircon thermochronology and geochronology.

In summary, this thesis delivers three concrete contributions. First, it establishes a mode-specific preprocessing framework for zircon Raman spectroscopy, systematically validated against 6225 spectral observations, which reduces inter-laboratory variability and enhances analytical precision. Second, it provides an empirical confirmation of three-stage annealing behaviour through non-linear modelling, identifying breakpoints at 607 K and 839.6 K and quantifying the differentiated recovery trajectories of internal (SiO_4) and external rotational modes. Third, it demonstrates that $\nu_2(SiO_4)$ preferentially couples with ν_3 rather than with external rotational modes during structural recovery, refining the physical interpretation of multi-band Raman thermochronology. Together, these contributions supply a quantitative foundation for improving the accuracy, reproducibility, and mechanistic understanding of Raman-based thermochronological methods. Two lines of analysis were developed. In the first, using Raman spectroscopy as the central element, a preprocessing algorithm and meticulous spectral analysis were developed for the subsequent interpretation of radiation- and annealing-induced phenomena in zircon. The second approach, using SAXS as the central element, evaluated the density differences between the tracks and the zircon volume as a function of the radiation and annealing treatments to which the samples were subjected. In this case, an article is being prepared for submission. To facilitate understanding of these lines of analysis and their ultimate complementarity, they will always be presented separately: sections named "Raman spectroscopy approach" and "SAXS approach". This same logic is clear in the sections "MATERIALS AND METHODS; RESULTS AND DISCUSSION; CONCLUSION".

It should be noted that Transmission Electron Microscopy (TEM), which was included in the original scope of this project and reflected in the thesis title, could not be performed. The samples irradiated at GSI were subsequently sent to the Australian Synchrotron for SAXS characterization and, due to logistical circumstances, were not returned to the author. This prevented the planned TEM stage. The results obtained by Raman spectroscopy and SAXS are not affected by this absence, and the thesis title is retained for consistency with the approved project.

1.1 RAMAN SPECTROSCOPY APPROACH

Zircon ($ZrSiO_4$) is a ubiquitous accessory mineral in igneous, metamorphic, and sedimentary rocks, serving as one of the most important minerals for geochronology and thermochronology. This dual significance stems from zircon's ability to retain isotopic information both from its formation and subsequent geological events. Its tetragonal crystal structure (space group $I4_1/amd$) readily incorporates uranium (U) and thorium (Th) into the Zr^{4+} site while strongly excluding lead (Pb). Over geological timescales, the alpha decay of U and Th produces radiogenic Pb and simultaneously induces cumulative radiation damage to the zircon lattice (Cherniak & Watson, 2003; Ewing et al., 2003; Harley & Kelly, 2007).

The progressive accumulation of alpha-recoil damage leads to metamictization, a transformation from a well-ordered crystalline structure to a partially or fully amorphous state. This process alters zircon's physical, chemical, and isotopic properties, influencing Pb retention, diffusion behavior, and spectroscopic signatures (Dawson et al., 1971; Murakami et al., 1991). While zircon is remarkably robust, its sensitivity to radiation damage makes it an excellent archive of both crystallization age and post-crystallization thermal history.

Raman spectroscopy has become a central, non-destructive tool for quantifying radiation damage and structural disorder in zircon. Changes in Raman spectra - most notably band broadening and shifts toward lower wavenumbers, systematically reflect the degree of metamictization (Nasdala et al., 1995; Trachenko et al., 2002). Among the vibrational modes of zircon, the internal SiO_4 tetrahedral vibrations are particularly informative, including the ν_2 bending mode (~439 cm^{-1}), the ν_3 asymmetric stretching mode (~1008 cm^{-1}), and external lattice modes near 356 cm^{-1} (Dawson et al., 1971; Geisler et al., 2001). The $\nu_3(SiO_4)$ mode, in particular, has emerged as the primary proxy for crystalline integrity, with its full width at half maximum (FWHM) providing a quantitative measure of accumulated radiation dose (Nasdala et al., 2003; Anderson et al., 2020; Zamyatin, 2022).

Radiation damage in zircon reflects a dynamic balance between damage accumulation and self-annealing, which is strongly temperature dependent. Geological heating can partially or fully recrystallize metamict zircon, modifying Raman spectral parameters and potentially causing Pb loss, thereby complicating U–Pb age interpretation (Balan et al., 2001; Nasdala et al., 2001; Zhang et al., 2000). Experimental annealing studies indicate that recovery proceeds through multiple stages, each governed by distinct kinetic mechanisms. Geisler (2002) proposed a three-stage model: low-temperature defect mobility (<500 °C), nanocrystalline reorganization at intermediate temperatures (500–700 °C), and epitaxial recrystallization above ~700 °C (Capitani et al., 2000; Geisler, 2002). However, the spectral response of different vibrational modes to annealing remains non-linear and incompletely constrained (Härtel et al., 2021, 2022).

Recent advances have expanded the application of Raman spectroscopy beyond damage quantification toward Raman-based zircon dating and thermochronology. Empirical correlations between Raman bandwidths and alpha-dose estimates derived from U and Th concentrations enable independent age constraints and assessment of thermal histories (Anderson et al., 2020; Resentini et al., 2020). Methodological developments have introduced numerical criteria for detecting partial annealing, band overlap, and mixed damage states, thereby improving the robustness of Raman thermochronology (Härtel et al., 2021, 2024). Complementary studies have further explored radiation-amorphized zircon structures, metasomatic alteration, and recovery of primary water contents and $\delta^{18}O$ signatures through thermal annealing (Shchapova et al., 2023; Wu et al., 2023; Yang et al., 2023).

In summary, zircon's sensitivity to alpha-decay damage, combined with the spatial resolution and non-destructive nature of Raman spectroscopy, underpins its growing importance in geochronology and thermochronology. Continued progress depends not only on methodological innovation but also on the development of standardized, quantitatively validated Raman preprocessing protocols to ensure analytical precision and inter-laboratory comparability.

1.1.1 Evaluating Raman Spectral Preprocessing Strategies for Radiation Damage Assessment in Zircon

Despite these advances, a major methodological limitation persists in the lack of standardized spectral preprocessing protocols for zircon Raman analysis. Baseline correction, normalization, smoothing, and peak-fitting procedures are commonly applied using laboratory-specific or instrument-default routines, often without systematic evaluation of their effects on damage proxies such as the FWHM of the ν_3 (SiO_4) band (Nasdala et al., 2003; Guo et al., 2021; Glace et al., 2024). This inconsistency introduces substantial inter-laboratory variability and compromises quantitative comparisons of radiation damage estimates (Bocklitz et al., 2011; Sadergaski et al., 2022).

Advanced statistical approaches, including generalized additive models (GAMs), segmented regression, and bootstrap resampling, offer powerful frameworks for addressing non-linear relationships between Raman parameters, radiation damage, and annealing temperature (Wood, 2017; Efron & Tibshirani, 1993; Gallagher, 2012). These methods enable objective identification of critical recovery thresholds and improved coupling between spectroscopic observations and physical models of damage accumulation and repair.

To address this gap - standardized spectral preprocessing protocols for zircon Raman analysis, systematically evaluates twelve preprocessing combinations by integrating three baseline correction algorithms was developed (polynomial, spline, and AirPLS) with four normalization methods (min–max, area, peak, and vector) (Gautam et al., 2015; Han et al., 2024). Preprocessing performance is assessed across multiple zircon vibrational modes using objective fitting quality metrics, coefficient-of-variation analysis, and statistical validation procedures (Guo et al., 2021; Yuan & Mayanovic, 2017). By explicitly identifying mode-dependent preprocessing behavior and combinations that minimize line width variability while maximizing fit quality, this work provides an evidence-based framework for preprocessing selection. The proposed approach enhances analytical consistency, reproducibility, and inter-laboratory comparability in Raman-based zircon radiation-damage assessment (Murakami et al., 1991; Nasdala et al., 2001, 2003; Zhang, H. Salje, et al., 2000).

1.1.2 Zircon Annealing Dynamics

In the annealing investigation, six independent hypotheses (again numbered H1–H6 for internal modular reference) were formulated: After preprocessing and validation of the spectra, the annealing dynamics in zircon were incorporated using multivariate analysis. In this context, the recovery dynamics of metamict zircons subjected to isothermal annealing were systematically investigated employing GAM modeling to test six fundamental hypotheses:

- (H1) superiority of non-linear over linear models in describing recovery curves.
- (H2) existence of distinct maximum recovery temperatures between external modes (Stage I: 473-607 K) and internal modes (Stage II: 607-840 K), corresponding to Geisler's stages.
- (H3) quantitative correlation between FWHM (bandwidth - crystalline ordering) and Center (Raman band position - structural strain) not tested in this study due to the absence of systematic band center position data in the available dataset, remaining as a proposal for future investigations.

- (H4) presence of preferential coupling between v2(SiO_4) and external vibrational modes.
- (H5) non-monotonic behavior in band area ratios across temperature.
- (H6) greater variance heterogeneity in external compared to internal modes during recovery.

The results that will be presented demonstrate two-phase recovery: an initial (Stages I-II) phase with preferential external-mode recovery and higher variability, and a final (Stage III) phase in which SiO_4 modes dominate and variability converges, contributing to the refinement of Raman thermometers and to the understanding of microstructural crystalline recovery mechanisms.

1.2 SAXS APPROACH

Small-Angle X-ray Scattering (SAXS) is a non-destructive technique for characterizing nanoscale structures in materials science, particularly ion tracks produced by swift heavy ions. The technique relies on elastic scattering of X-rays due to electron density variations within a material, providing structural information at length scales typically inaccessible to conventional microscopy. The scattering vector q is formally defined as the difference between the wavevectors of the incident and scattered radiation; its magnitude is given by $q = (4\pi/\lambda) \sin(\theta/2)$, where λ represents the X-ray wavelength and θ is the scattering angle. It is this magnitude $|q|$ that appears in the form-factor expressions used throughout this work (Kluth et al., 2008; Afra et al., 2011). SAXS is optimally suited for investigating structures in the 1–100 nanometer range, encompassing typical ion track dimensions in minerals and amorphous materials (Kluth et al., 2008).

SAXS provides statistical averaging over approximately 10^6 individual tracks within the sampled volume, yielding results representative of the bulk material. This statistical robustness contrasts with transmission electron microscopy (TEM), which examines only a small number of tracks. SAXS measurements are non-destructive, allowing the same sample to be subjected to additional experimental treatments such as thermal annealing (Afra et al., 2011).

The theoretical framework underlying SAXS analysis of ion tracks rests upon electron density contrast between the track region and the surrounding crystalline matrix. Experimental measurements demonstrate that density change within ion tracks in apatite is approximately 1 ± 0.5% lower than the crystalline matrix, consistent with amorphous material formation (Afra et al., 2011). Similar density changes have been observed in olivine, with SAXS measurements yielding a density reduction of approximately 1 ± 0.7% (Afra et al., 2012).

When the ion track axis is oriented parallel to the incident X-ray beam, the scattering pattern is circularly symmetric. However, when tracks are inclined relative to the beam, scattering becomes highly anisotropic, manifesting as narrow streaks perpendicular to the track axis (Kluth et al., 2008); an experimental example of this anisotropic pattern can be seen in Figure 1a, where the elongated scattering feature corresponds to tracks tilted with respect to the beam.

SAXS offers substantial advantages compared to chemical etching and TEM. Chemical etching fundamentally destroys the primary damage structure of the track, losing essential information regarding the actual scale and morphology of the radiation damage (Afra et al., 2012). SAXS achieves sub-nanometer precision in determining track dimensions (approximately 0.1 nm for radius measurements) (Afra et al., 2011). Furthermore, SAXS can be performed in situ during annealing experiments.

SAXS measurements have direct implications for thermochronology, as they enable the characterization of latent track morphology at the nanometer scale without chemical etching, preserving the original damage structure. The correlation between SAXS-derived track radii and Raman spectral parameters (e.g., FWHM) provides complementary information on the relationship between nanoscale track dimensions and local vibrational disorder, which is relevant for calibrating Raman-based thermochronological approaches (Tamer et al., 2017; Anderson et al., 2020).

2. MATERIALS AND METHODS

2.1 SAMPLE, HEAT TREATMENTS ANDIRRADIATION

In this work, a sample of zircon, an accessory mineral, was used. For the proposed analyses, aliquots with thicknesses of 30-40 μm were subdivided. These aliquots were subjected to sequential treatments.

The selection of thermal treatments was carried out using a statistical model, the D-Optimal, developed by Moreira et al. (2005) for annealing models. Applying the D-Optimal algorithm, it is possible to determine the matrix of experiments that minimizes the dispersion of parameters as a function of time and temperature conditions, among all possible matrices considering the total space of experiments that could be performed. For this thesis, 20 thermal treatments were selected as shown in Table 1.

Table 1. Thermal Treatment Conditions for S1 Samples

No.	ID	t (h)	T (°C)	T (K)
1	58	1	500	773.15
2	79	1	600	873.15
3	67	1	600	873.15
4	80	1	600	873.15
5	83	1	700	973.15
6	71	1	800	1073.15
7	84	10	300	573.15
8	76	10	450	723.15
9	72	10	650	923.15
10	78	10	650	923.15
11	63	10	650	923.15
12	64	10	700	973.15
13	74	10	800	1073.15
14	70	100	200	473.15
15	56	100	300	573.15
16	59	100	500	773.15
17	69	100	650	923.15
18	73	1000	350	623.15
19	98	1000	500	773.15
20	92	1000	600	873.15

Note: ID = aliquot identifier; t = annealing time; T = treatment temperature.

The thermal treatments were carried out in the Chronology Laboratory of the Department of Chronology and Cosmic Rays (DRCC) of IFGW-UNICAMP. Samples were heat-treated in a tubular furnace designed and built at IFGW-UNICAMP by Pedro Moreira (currently integrated into the DRCC laboratory infrastructure), which controls temperature using two type K thermocouples: one connected to the furnace and the other to the sample holder. These thermocouples are connected to an N1100 Universal Process Controller (NOVUS brand).

After each treatment, the samples were renamed and classified as follows: a) raw sample, without treatment, referred to as ST; b) ST sample heat-treated to induce repair of the crystalline structure, called ANN. These nomenclatures will reappear in section 2.3.1.

In addition, the samples were irradiated with swift heavy ions to simulate the presence of fission tracks, followed by characterization via Raman and SAXS spectroscopy. Irradiation was performed at the Gesellschaft für Schwerionenforschung (GSI) in Darmstadt, Germany, using ^{197}Au ions at 8.6 MeV/u with a fluence of 10^{11} ions/cm^2. The samples, approximately 100 μm thick, were irradiated at normal incidence (90° relative to the surface) to produce tracks perpendicular to the sample plane.

2.2 RAMAN SPECTROSCOPY

All Raman spectroscopic measurements, for pre-processing analyses and for Zircon Annealing Dynamics, were performed at UNESP, Presidente Prudente, São Paulo state, Brazil, using a micro-Raman spectrograph (Renishaw inVia) equipped with a CCD detector and a Leica Microscope. The Raman spectroscopic analysis used a 633 nm laser at 50% power, with a 50× magnification objective, 10.00s exposure time, 1 accumulation, and 1800 lines/mm grating configuration.

2.2.1 Systematic evaluation of preprocessing methods

The zircon samples investigated in this study were derived from an original experimental dataset generated specifically for this work. The specific focus of this research centers on sample called "ANN", a zircon specimen from a curated geological repository at the Department of Cosmic Rays and Chronology (DRCC) of UNICAMP, which serves as a baseline for non-pristine zircon analysis. This sample, originally derived from “ST”, underwent controlled thermal annealing following established protocols to promote partial recovery of radiation damage and restore crystalline structure. The thermal treatment was specifically designed to induce controlled structural modifications in the zircon lattice, creating optimal conditions for radiation damage assessment and enabling comparative analysis of structural recovery mechanisms in zircon crystals. As this study focuses on methodological optimization of Raman spectral preprocessing, the absence of age and U/Th content data does not compromise the analytical objectives. The methodological framework is designed to validate preprocessing techniques through comparative spectral analysis independent of temporal or compositional constraints.

A computational framework was developed in Python 3.11 implementing systematic evaluation of spectral preprocessing methodologies for zircon Raman analysis. The framework incorporates baseline correction algorithms (iterative AirPLS, cubic polynomial, adaptive spline) and normalization techniques (min-max, area, peak, vector) following established principles for spectral preprocessing pipelines (Bocklitz et al., 2011; Gautam et al., 2015; Han et al., 2024).The automated processing pipeline processes CSV-formatted Raman spectra with spectral data acquisition parameters ranging from 0.198 to 1711.21 cm^{-1} at 1.92 cm^{-1} intervals, providing 892 data points per spectrum. The complete source code, including configuration files and documentation, is provided in Appendix 1.

Raw spectra undergo spectral smoothing using the Savitzky-Golay filter (Savitzky& Golay, 2002)with configurable window length of 11 points and polynomial order of 3, balancing noise reduction with preservation of peak shape characteristics (Ryabchykov et al., 2022).The systematic evaluation methodology addresses method selection through comprehensive testing of preprocessing effectiveness across different vibrational modes, comparing baseline correction and normalization method combinations (Table S1).

For each baseline and normalization combination and for every vibrational mode, a set of quantitative metrics was calculated to assess performance. Fit quality was evaluated using the coefficient of determination (R^2), with its mean and standard deviation used to assess consistency across samples (Sadat & Joye, 2020). Linewidth was characterized by the FWHM in cm^{-1}, and spectral center by the peak central position. To quantify measurement precision, we additionally calculated the coefficient of variation of FWHM (FWHM CV) and of peak position (Center CV) across replicate spectra. The coefficient of variation represents a dimensionless metric of relative precision expressed as a percentage, enabling standardized comparison across different measurement scales. The FWHM CV quantifies variability in linewidth measurements, serving as an indicator of preprocessing method stability and consistency in band shape characterization across replicate analyses. Center CV measures variation in peak central position, providing a direct assessment of spectral reproducibility and positioning accuracy for vibrational mode identification. These CV-based metrics facilitate systematic comparison of preprocessing method effectiveness by quantifying both relative and absolute precision components, enabling evidence-based selection of optimal analytical protocols.

The FWHM and position of the $\nu_3(SiO_4)$ band are well established as indicators of radiation damage in zircon and can be calibrated against annealing-based damage frameworks (Ginster et al., 2019). The CV-based metrics are introduced here as practical measures of relative and positional precision in our dataset.

Hypotheses for the preprocessing module — The following set of hypotheses (H1–H4) concerns the systematic evaluation of spectral preprocessing strategies.

Four primary hypotheses (H1-H4) were systematically evaluated to provide quantitative guidance for preprocessing method selection in zircon Raman spectroscopy.

- H1 specifically tested whether Polynomial baseline correction would demonstrate superior performance compared to Spline and AirPLS approaches across all spectral modes.
- H2 hypothesized that Min-Max normalization would show systematic advantages over area-based, peak-based, and vector normalization methods.
- H3 was designed to evaluate whether optimized preprocessing combinations would significantly reduce linewidth variability as measured by coefficient of variation.
- H4 tested whether systematic optimization would increase the percentage of spectral fits achieving R^2 values above 0.9, representing high-quality analytical results. The specific test parameters for each hypothesis are summarized in Table S2.

Validation was conducted globally and regionally using established statistical practices in spectroscopic analysis including non-parametric tests like Kruskal-Wallis (Kruskal & Wallis, 1952), with detailed statistical results provided in the Supplementary Material.

2.2.1.1 Outlier Detection and Data Quality Assessment

The implementation of rigorous outlier detection and data quality assessment protocols is essential for ensuring analytical integrity in Raman spectroscopy-based radiation damage determinations (Pell, 2000; Romo-Chavero et al., 2024; Shimizu, 2022; Thériault et al., 2024; Toribio et al., 2025). This methodology employs an approach combining statistical (IQR-based) outlier detection followed by secondary validation using spectral quality metrics and physical constraints (Bocklitz et al., 2011; Guo et al., 2021; Ryabchykov et al., 2022). This maintains data quality while maximizing analytical coverage, thus maintaining analytical rigor without eliminating meaningful spectral information. This balance is particularly important for zircon radiation damage studies where sample availability may be limited.

Statistical outlier detection employs the Interquartile Range (IQR) method with a 1.5×IQR threshold as an initial screening step to flag candidate outliers in each vibrational mode's FWHM distribution. The method calculates the first (Q1) and third (Q3) quartiles for each mode, with measurements falling outside the range $[Q1-1.5\times IQR, Q3+1.5\times IQR]$ provisionally identified for review (Shimizu, 2022). However, because peak broadening and shifting may reflect genuine physical phenomena rather than analytical artifacts (Ginster et al., 2019; Härtel et al., 2021), a flagged measurement is only excluded if it additionally fails the Gaussian fit quality criterion ($R^2<0.9$). Measurements with FWHM outside the IQR bounds but with $R^2\geq0.9$are retained, as their broadening is considered physically meaningful. Thus, the $R^2 < 0.9$ threshold serves a dual purpose: it flags spectra for review during initial screening and, when combined with the IQR criterion, provides the final condition for outlier removal.

This approach is complemented by spectral quality validation using Gaussian deconvolution with boundary constraints to assess individual peak fitting quality and identify measurements that do not meet established quality criteria (Chen et al., 2025; Kaneki et al., 2024; Sparavigna, 2024; Tagliaferro et al., 2020; Yuan & Mayanovic, 2017). The Gaussian deconvolution approach models individual Raman peaks as Gaussian functions, evaluating three key parameters. These parameters include: the coefficient of determination (R^2) for overall fit quality, the FWHM stability indicating consistent peak shape, and the peak center position accuracy ensuring appropriate assignment of the spectral region. Measurements below R^2 values of 0.9 are systematically flagged for review.

The validation approach ensures that outliers represent genuinely anomalous measurements rather than valid but extreme spectral characteristics, incorporating FWHM ranges consistent with known zircon vibrational modes under varying radiation damage conditions, R^2 fitting quality thresholds appropriate for the specific spectral region and analytical conditions, and peak position ranges established from literature values and empirical observations.

The multi-criteria approach eliminates clearly anomalous measurements (typically <5% of total acquisitions) while preserving >95% of high-quality spectral data, important for radiation damage assessment studies where data availability may be limited. The outlier detection criteria employed in this study are comprehensively summarized in Table S3 in the Supplementary Material, which details the individual threshold values, quality impact parameters, and statistical validation approaches used to identify and remove anomalous measurements.

2.2.2 Zircon Annealing Dynamics

The experimental sequence comprised the following steps:

(1) acquisition of geological metamict natural zircon ($ZrSiO_4$) sample from collection (Sample 21, original crystalline deterioration state);

(2) initial thermal treatment to obtain partially recovered state (Sample 22, non-pristine baseline);

(3) subdivision into 20 homogeneous aliquots;

(4) controlled irradiation with heavy Au^{197} ions (~1 MeV/u) at GSI facilities (Gesellschaft für Schwerionenforschung, Darmstadt, Germany) for fission track simulation and uniform radiation damage induction;

(5) variable thermal treatments according to experimental matrix (see Table 1);

(6) Raman spectroscopy analysis. Irradiation was performed on a single aliquot of Sample 22 before subdivision, ensuring uniform dose across all experimental samples. The main sample, designated S1, was prepared with 30-40 μm thickness, resulting in approximately 2,200 raw spectra and 6,225 valid observations after processing (Nasdala et al., 2001; Palenik et al., 2003).

Spectra were acquired in the 100-1100 cm^{-1} region, covering the characteristic vibrational modes of zircon: external lattice rotation modes (ExtRot, ~356 cm^{-1}), bending (ν_2, ~439 cm^{-1}), and asymmetric stretching (ν_3, ~1008 cm^{-1}) of SiO_4 tetrahedra (Zhang et al., 2000; Dawson et al., 1971). Spectral preprocessing with baseline correction, maximum intensity normalization, Savitzky-Golay smoothing, and Gaussian peak fitting, with acceptance criteria of $R^2 > 0.98$ and $\chi^2 < 0.05$.

Generalized Additive Models (GAM) were implemented in Python using the pyGAM package (Servén& Brummitt, 2018), following the theoretical framework of Wood (2017), with penalized cubic splines (de Boor, 2001), 10 basis functions, and smoothing parameter $\lambda = 0.001$. Fit quality was assessed using Pseudo-R^2, Akaike Information Criterion, and Generalized Cross-Validation, following Burnham and Anderson (2002) criteria. Critical temperature identification employed segmented regression with Differential Evolution optimization (Storn& Price, 1997), while vibrational coupling tests used paired bootstrap with 10,000 resamples (Efron, 1979; Efron &Tibshirani, 1993). Observations were stratified according to Geisler's (2002) recovery stages: Stage I (<500°C), Stage II (500-700°C), and Stage III (>700°C).

2.3 SAXS

SAXS measurements were performed at the SAXS/WAXS beamline of the Australian Synchrotron (Melbourne, Australia), utilizing monochromatic X-rays with photon energy of 17 keV. The camera length was 3.2 m (3200 mm), providing optimal resolution in the q-range appropriate for characterizing track radii in the 2-10 nm range.

The detector system employed was a Pilatus3 2M hybrid pixel detector, offering high dynamic range, excellent spatial resolution, and superior signal-to-noise characteristics essential for detecting weak scattering from individual ion tracks. Sample alignment was achieved using a hexapod positioning system (Newport HXP50V6-MECA) operating under vacuum, permitting precise positioning and tilting of the sample relative to the incident X-ray beam in transmission mode.

The geometry of SAXS measurements requires careful consideration of the relationship between track orientation and the direction of the incident X-ray beam. When the X-ray beam is parallel to the track axis, the scattering pattern consists of circularly symmetric intensity distributions. However, this geometry provides limited information about track dimensions. Inclining the sample relative to the X-ray beam by angles between 5° and 10° dramatically enhances the observable scattering signal. Tilt angles of approximately 10° provide optimal signal-to-noise characteristics (Afra et al., 2011).

Accurate background subtraction is essential for extracting meaningful structural information. Background scattering originates from the crystalline matrix material, sample environment, and instrumental contributions. For ion track analysis, this is achieved by comparing irradiated samples with non-irradiated reference samples (Afra et al., 2012).

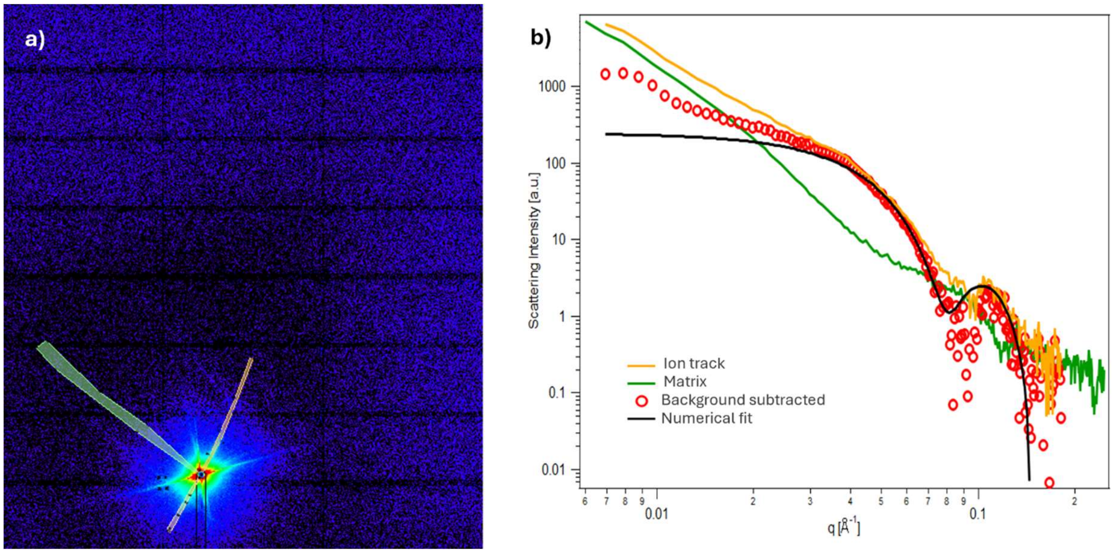

Figure 1– 2D SAXS pattern and extracted scattering intensity curves. a) 2D scattering pattern of zircon after swift heavy-ion irradiation. The orange region corresponds to the integrated region corresponding to the ion track scattering and the green region to the integrated area corresponding to the scattering from zircon. b) Resulting extracted scattering intensity of the ion track and zircon (orange and green, respectively), the red circles correspond to the scattering signal of the ion tracks after subtraction of the zircon contribution. The black curve represents the corresponding numerical fit following the hard cylinder form factor model.

The form factor for a hard cylinder oriented perpendicular to the scattering plane is given by:

$$f(q) = 2\pi L R \rho_0 \times [J_1(Rq)/(Rq)]$$

where L is the track length, R is the track radius, ρ_0 represents the electron density difference between track and matrix, and J_1 is the first-order Bessel function of the first kind. The Bessel function term produces characteristic oscillations in scattering intensity as a function of q, with minima occurring when $Rq \approx 3.83$, 7.02, and 10.17 for the first, second, and third minima respectively (Afra et al., 2011).

For amorphous materials, a more sophisticated core-shell model with smooth density transitions provides a better description of observed scattering. The Core Transition Shell (CTS) model has been successfully applied to characterize ion tracks in amorphous silicon dioxide, where SAXS measurements reveal a core region of approximately 0.77 nm, a transition region of about 2.29 nm, and a shell region of approximately 1.58 nm, yielding a total track radius of approximately 4.6 nm (Dutt et al., 2023). Recent work has demonstrated that ion tracks exhibit characteristic density variations with an under-dense core surrounded by an over-dense shell, providing improved understanding of the track formation mechanism (Mota-Santiago et al., 2018).

Real ion track populations exhibit variations in track radius that must be accounted for in data analysis. Polydispersity, expressed as the standard deviation divided by the mean radius, is typically found to be approximately 10% or less (Afra et al., 2012).

The extraction of track parameters from SAXS data involves non-linear least squares fitting. For well-constrained fits with clear oscillatory features, relative uncertainties in track radius determination can be better than 1%, corresponding to absolute uncertainties of approximately 0.1 nm for typical track radii in the 5-10 nm range (Afra et al., 2011).

SAXS measurements were initially attempted on all 20 annealed aliquots. However, clear scattering patterns indicative of cylindrical ion tracks were observed for only seven samples. For the remaining thirteen, the scattering signal lacked the characteristic oscillations required to fit a hard-cylinder model, likely due to track annealing or insufficient electron density contrast. Consequently, the SAXS analysis presented in this thesis is restricted to these seven samples.

The same aliquots used for the SAXS measurements were intended for subsequent transmission electron microscopy (TEM) analysis. However, the samples were not released by the synchrotron facility after the SAXS experiments. Consequently, the TEM characterization originally planned could not be carried out. The impact of this limitation on the scope of the conclusions is addressed in the final chapter of this thesis.

3. RESULTS AND DISCUSSION

3.1 RAMAN SPECTROSCOPY APPROACH

3.1.1Evaluating Raman spectral preprocessing strategies for radiation damage assessment in zircon

3.1.1.1 Quality Assessment and Outlier Detection

Thetwo-stage quality assessment process described belowwas to evaluate 80 zircon Raman spectra,revealing high data consistency across different spectral regions, as also seen in Fatima et al. (2020); Utsunomiya et al. (2002) and Weber, (1993).

Stage 1 - Initial Spectral Screening: the peak detection algorithm initially identified 495 Raman peaks across seven distinct spectral regions. Spectral region validation criteria (R^2 threshold < 0.9) were applied, eliminating 34 peaks (6.9%) that did not meet minimum fit quality standards. This screening resulted in 461 high-quality spectral features for subsequent analysis.

Stage 2 - Statistical Cleaning: multi-criteria outlier removal was applied to the 461 spectrally validated peaks, eliminating 5 additional peaks (1.1% of screened peaks) using statistical outlier detection (IQR method with 1.5×IQR threshold) and quality constraints (R^2 threshold < 0.3 for Gaussian fits). The overall retention rate was 91.8% (456 of initial 495 spectrum).Outlier removal was performed using multiple statistical and physical criteria (Table S3), resulting in the elimination of 5 peaks from a total of 461 (1.1%, Table S4). The most affected regions were $\nu_1(SiO_4)$ (3.3% removal) followed by External Mode 4 (2.5% removal) and ν_2 (1.2% removal), while ν_3, External Mode 1, and External Mode 3 showed no outliers. Comparative analysis (Table S5) shows that data cleaning achieved its primary objective: reducing variability without altering fundamental spectral characteristics.

The outlier removal process achieved measurable improvements in multiple quality dimensions. The $\nu_1(SiO_4)$ region showed improvement, with CV reduction from 17.8% to 16.3% and FWHM range narrowing (Table S5). The $\nu_2(SiO_4)$ region demonstrated CV improvement from 3.7% to 3.5% with FWHM range restriction (Table S5). External Mode 4 showed CV reduction from 1.8% to 1.6% while maintaining the already narrow FWHM distribution (Table S5). Detailed FWHM range specifications for all vibrational modes are provided in Table S6. Overall dataset quality metrics achieved mean R^2 of 0.995, with 98.9% of peaks falling within established spectral regions.

3.1.1.2. Regional Spectral Analysis

Figure 2 presents comparative analysis of FWHM distributions across seven distinct spectral regions of zircon Raman spectra, showing data before and after outlier removal processing. The 36 k=0 vibrational modes of zircon ($ZrSiO_4$) were classified using group theory (Dawson et al., 1971; R W G Syme et al., 1977), with 17 Raman active modes including internal SiO_4 tetrahedral vibrations (ν_1, ν_2, ν_3, ν_4) and external lattice modes. The analysis revealed a clear hierarchy of radiation damage sensitivity, with External Mode 4 exhibiting the narrowest FWHM distribution (median = 12.15 cm^{-1}) and External Mode 1 the broadest (median = 20.26 cm^{-1}). The boxplot visualization allows direct assessment of data quality improvement (Table S7) and spectral homogeneity within each vibrational mode region.

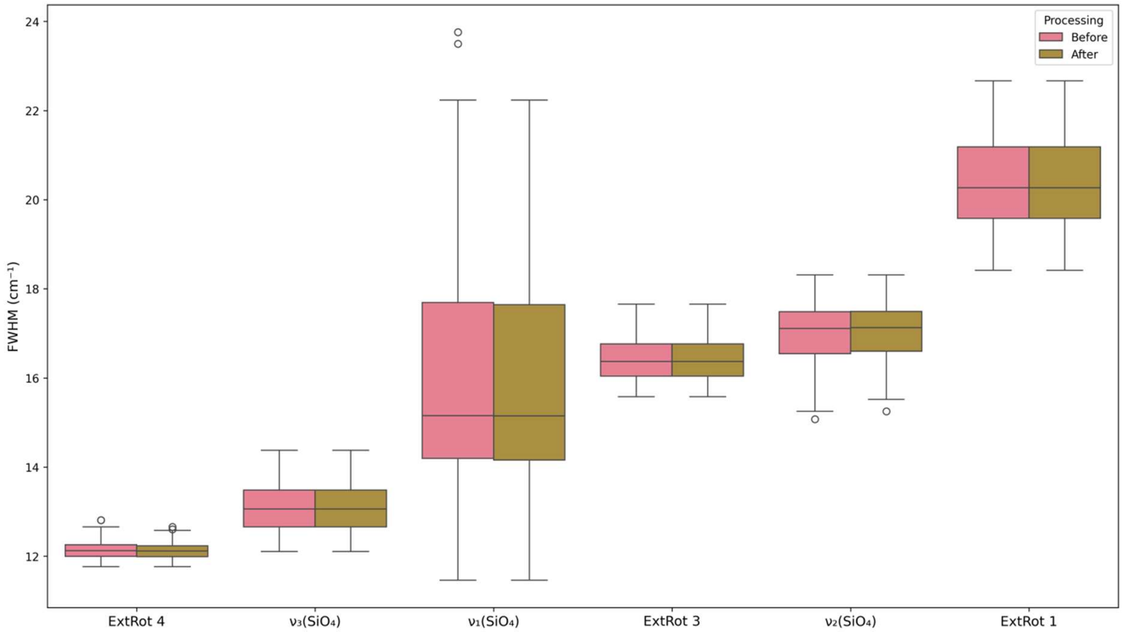

Figure 2: Comparative Analysis of FWHM Distribution by Spectral Regions

The $\nu_3(SiO_4)$ region corresponds to B1g asymmetric stretching vibrations of SiO_4 tetrahedra (Dawson et al., 1971; R W G Syme et al., 1977), with FWHM serving as a proxy for metamictization (Hoskin & Rodgers, 1996; Nasdala et al., 1995). The 80 samples showed a consistent FWHM median of 13.06 ± 0.54 cm^{-1}, with typical ranges as detailed in Table S19. Within the observed damage sensitivity hierarchy (FWHM range: 12.12-20.26 cm^{-1}, factor 1.67×), the $\nu_3(SiO_4)$ asymmetric mode exhibited optimal behavior with 80 detected peaks, lower FWHM values (12.89 ± 0.32 cm^{-1}), and higher R^2 fit quality (0.995 ± 0.001), positioning it as the second most damage-resistant mode after External Mode 4.

The $\nu_1(SiO_4)$ symmetric stretching mode exhibits significantly greater variability in the damage sensitivity hierarchy. Corresponding to fully symmetric A1g Si-O vibration (Dawson et al., 1971; Syme et al., 1977), this mode demonstrated third position in damage resistance, with constant FWHM median of 15.15 cm^{-1} and improved precision through coefficient of variation reduction from 17.8% to 16.3% after outlier removal (n=61 to n=59, 9.2% removal) (Nasdala et al., 1995; Zhang, Salje, et al., 2000).

The $\nu_2(SiO_4)$ region, corresponding to Si-O bending deformation, occupies the intermediate range of the damage sensitivity hierarchy. As A1g Si-O bending vibration

(Dawson et al., 1971; Syme et al., 1977), this mode demonstrated methodological robustness with minimal sample loss (n=80 to n=79, 1.25% reduction), consistent with the absence of detected outliers in this spectral region (Mittal et al., 2000; Smirnov et al., 2010).

External rotational modes (External Mode 1-4) demonstrate significant variability, representing collective lattice vibrations involving rigid rotations and translations of SiO_4 tetrahedra (Dias et al., 2009, 2019; Syme et al., 1977). This vibrational family spans the complete spectrum of sensitivity responses, from extremely sensitive External Mode 1 (median=20.26 cm^{-1}), through intermediate responses of External Mode 3 (median=16.12 cm^{-1}), to the remarkable stability of External Mode 4 (median=12.15 cm^{-1}) as the most damage-resistant mode. Paradoxically, External Mode 4 exhibited FWHM values systematically narrower than literature ranges ($12.2 \pm 0.2\ cm^{-1}$ vs. 15–40 cm^{-1}) yet achieved the most robust spectral fits ($R^2 = 0.988$) and the highest classification score among all vibrational modes. The physical origin of this anomaly remains undetermined; possibilities include a sample-specific ordering effect or an instrumental convolution not captured by the standard deconvolution procedure. The complete absence of External Mode 2 may reflect either a genuine physical suppression under the analytical conditions employed or a limitation of the spectral fitting parameters used. Discriminating between these two interpretations was beyond the scope of this work.

Inter-regional analysis demonstrates a clear hierarchy of radiation damage sensitivity, establishing fundamental insights into vibrational mode responses to structural perturbations. With External Mode 4 exhibiting the lowest FWHM (median = 12.15 cm^{-1}) and External Mode 1 the highest (median = 20.26 cm^{-1}), the FWHM range varies from 12.15 to 20.26 cm^{-1}, representing a factor of 1.67×. Physical interpretation is based on the concept that peak broadening (FWHM increase) in zircon Raman spectra correlates directly with α-decay radiation damage accumulation (Ende et al., 2021; Murakami et al., 1991; Nasdala et al., 1995, 2001, 2003; Zhang, Salje, et al., 2000), lattice disorder and amorphization degree (Dias et al., 2009, 2019), SiO_4 tetrahedral distortion (Smirnov et al., 2010; Zhang, Salje, et al., 2000), and local symmetry breaking. The $\nu_3(SiO_4)$ band FWHM and Raman shift have been established as reliable proxies for quantifying radiation damage in zircon (Ende et al., 2021; Ginster et al., 2019; Härtel et al., 2021; Nasdala et al., 1995, 2003; Zhang, Salje, et al., 2000), with FWHM exhibiting logarithmic relationship with accumulated α-dose (Ginster et al., 2019; Murakami et al., 1991; Nasdala et al., 2001).

The observed hierarchy reflects fundamental vibrational physics, where some modes are intrinsically more localized and disorder-resistant (Dawson et al., 1971; Ende et al., 2021;

Kolesov et al., 2001; Mittal et al., 2000; Nasdala et al., 2003; Smirnov et al., 2010) while others couple more strongly to lattice imperfections (Ende et al., 2021; Murakami et al., 1991). This hierarchy, validated by analyzed data, demonstrates that External Mode 4 represents the most damage-resistant mode, followed by $\nu_3(SiO_4)$, $\nu_1(SiO_4)$, External Mode 3, $\nu_2(SiO_4)$, and finally External Mode 1 as the most sensitive.

The baseline correction methodology demonstrates systematic robustness with polynomial and spline functions showing equivalent performance ($R^2 \geq 0.998$ across all combinations), indicating that method selection effectiveness depends primarily on spectral region complexity rather than mathematical algorithm choice. Min-Max normalization emerges as the optimal strategy for intensity standardization, as also seen in Bocklitz et al. (2011); Guo et al. (2021), demonstrating superior preservation of relative peak relationships while eliminating systematic variations from instrumental factors. The coefficient of variation (CV) reduction from 35-45% (untreated spectra) to 22.59% across all regions validates the effectiveness of systematic optimization (Shimizu, 2022; Thériault et al., 2024).

Visual evaluation of the paired boxplot design (Figure 3) reveals consistent median shifts to lower FWHM values after cleaning, reduction of upper-limit outliers without compromising data representativeness, and preservation of inter-regional FWHM ordering. Overall dataset quality metrics achieved mean R^2 of 0.995, with 98.9% of peaks falling within established spectral regions and exceptional fit quality across all analyzed samples.

3.1.1.3Damage Categorization and Statistical Analysis

3.1.1.3.1 Radiation Damage Classification in Zircon: $\nu_3(SiO_4)$ Band Analysis

The radiation damage classification framework utilizes the $\nu_3(SiO_4)$ band at approximately 1008 cm^{-1} as the primary indicator of crystalline integrity. This asymmetric Si-O stretching mode with B_1g symmetry demonstrates exceptional sensitivity to radiation damage through its direct correlation with defect density (Bocklitz et al., 2011; Murakami et al., 1991; Nasdala et al., 1995, 2001, 2003; Shimizu, 2022; Zhang, Salje, et al., 2000). The $\nu_3(SiO_4)$ band's enhanced sensitivity derives from vacancy generation and atomic displacement effects on Si-O bond strengths induced by α-radiation damage, providing high resolution for crystalline-to-metamict transition detection (Bocklitz et al., 2011).

The quantitative damage assessment employs established calibration methodologies where FWHM serves as a reliable proxy for radiation damage accumulation (Shimizu, 2022). The observed FWHM distributions demonstrate consistent behavior indicative of moderate damage states, as validated through empirical cumulative distribution function (ECDF) analysis (Figure 3). The continuous progression within the moderate damage regime confirms uniform damage state distribution and validates the $\nu_3(SiO_4)$-based methodology effectiveness (Fatima et al., 2020; Guo et al., 2021; Nasdala et al., 2003).

Physical mechanisms underlying radiation damage involve interconnected processes: α-recoil damage track generation, lattice strain accumulation, and progressive SiO_4 tetrahedral distortion leading to metamict transition (Murakami et al., 1991; Nasdala et al., 1995, 2001, 2003; Utsunomiya et al., 2002; Weber, 1993; Zhang, Salje, et al., 2000). The moderate damage classification indicates samples characterized by intermediate radiation damage-states corresponding to initial amorphous domain percolation within crystalline matrices. These structural modifications directly influence the vibrational characteristics of the zircon lattice, with the $\nu_3(SiO_4)$ mode providing the most sensitive indicator of crystalline integrity (Shimizu, 2022).

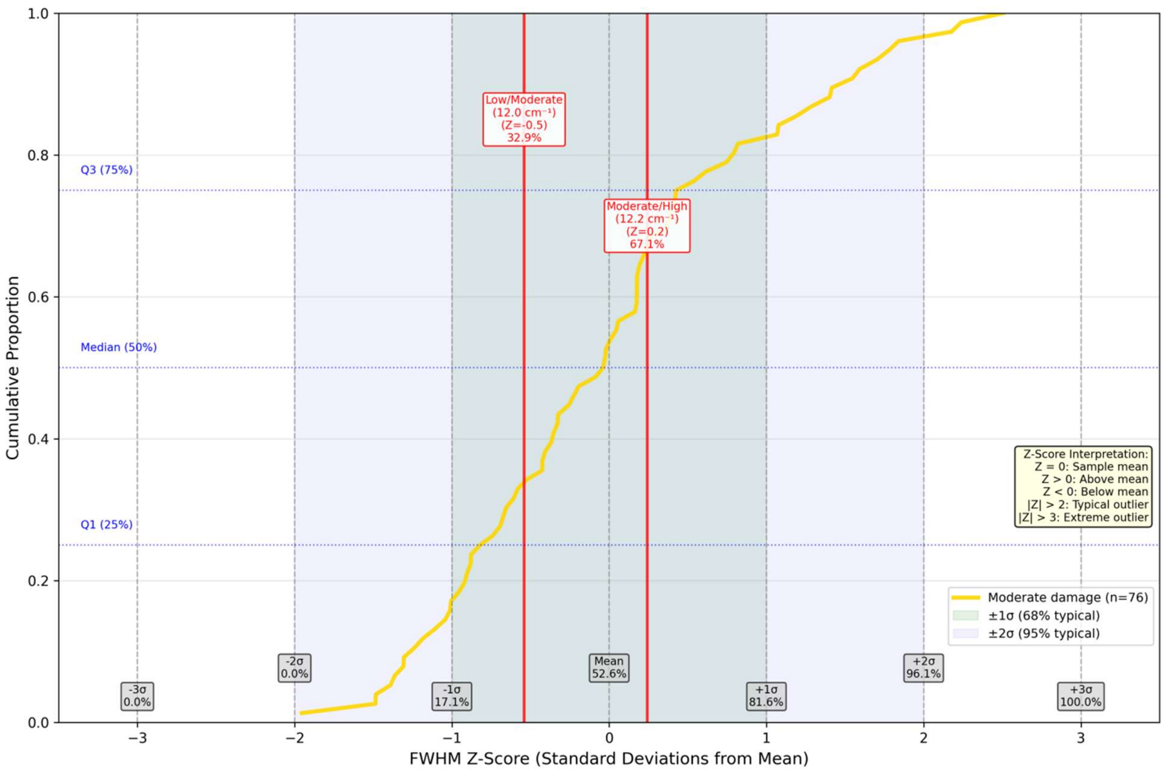

Figure 3 - – ECDF analysis of $\nu_3(SiO_4)$ FWHM for damage categorization. Empirical cumulative distribution function (ECDF) analysis of Z-score normalized $\nu_3(SiO_4)$ FWHM values demonstrating continuous progression within moderate damage regime and validating the radiation damage categorization framework.

3.1.1.3.2 Methodological Validation

The systematic evaluation of four principal hypotheses confirmed a 75% success rate (3 of 4 confirmed). H1 was rejected globally on the basis of performance equivalence between polynomial and spline baselines ($\Delta R^2 = 0.001$); mode-specific analysis, however, revealed that spline baseline correction outperforms polynomial for the $\nu_3(SiO_4)$ mode, grounding the recommendation for mode-dependent preprocessing optimization.The AirPLS baseline correction method was excluded from 20%of combinations due to NaN value generation (Fatima et al., 2020; Guo et al., 2021; Yuan &Mayanovic, 2017), demonstrating technical limitations that require alternative approaches. The results establish that baseline correction method performance depends on spectral region complexity that normalization strategies significantly impact quantitative accuracy, and that regional specificity determines optimized preprocessing parameter selection (Götze, 2012; Nasdala et al., 2003).

As shown in Table 2, the hypothesis validation results reveal distinct performance characteristics across vibrational modes that inform their applicability for crystallinity assessment. The $\nu_3(SiO_4)$ symmetric stretching mode demonstrates universal consistency across all six validation methods (6/6 identical $R^2 = 0.999$), making it the most robust crystallinity indicator due to its method-independent reliability. While the $\nu_2(SiO_4)$ bending mode achieves the highest absolute R^2 value (1.000), it exhibits method-dependent variations that require specific preprocessing optimization. The $\nu_1(SiO_4)$ mode provides consistent performance but demonstrates greater sensitivity to preprocessing selection, while external rotational modes show more variable performance with $\Delta R^2 = 0.001$, reflecting their moderate sensitivity to preprocessing optimization.

Table 2: Hypothesis Validation by Vibrational Mode

	Vibrational Mode	**Status**	**R^2 Values**	**Notes**
H1: Polynomial baseline superiority	$\nu_3(SiO_4)$	Rejected	Spline: 0.999	Both Spline and Polynomial show equivalent performance ($\Delta R^2 = 0.001$)
H1: Polynomial baseline superiority	$\nu_1(SiO_4)$	Rejected	Polynomial: 0.999	No significant advantage over alternative baseline methods
H1: Polynomial baseline superiority	$\nu_2(SiO_4)$	Rejected	Polynomial: 0.999	Performance within analytical precision limits
H1: Polynomial baseline superiority	External modes	Rejected	$\Delta R^2 = 0.001$	Baseline selection not primary performance factor

	Vibrational Mode	**Status**	**R^2 Values**	**Notes**
H2: Min-Max normalization advantage	$\nu_3(SiO_4)$	Confirmed	0.998079	Complete equivalence across all methods (6/6 identical performance)
H2: Min-Max normalization advantage	$\nu_1(SiO_4)$	Confirmed	High	Pronounced effects on secondary stretching modes
H2: Min-Max normalization advantage	$\nu_2(SiO_4)$	Confirmed	High	Superior performance across deformation modes
H2: Min-Max normalization advantage	External modes	Confirmed	Stable	Consistent advantages for rotational modes
H3: Reduced coefficient of variation	$\nu_3(SiO_4)$	Confirmed	4.48% CV	Substantial improvement over typical values (35-45%)
H3: Reduced coefficient of variation	$\nu_1(SiO_4)$	Confirmed	5.09% CV	Significant precision enhancement
H3: Reduced coefficient of variation	$\nu_2(SiO_4)$	Confirmed	4.12% CV	Enhanced measurement stability
H3: Reduced coefficient of variation	External modes	Confirmed	22.59% CV	Systematic variability reduction across all modes
H4: High-quality fit improvement	$\nu_3(SiO_4)$	Confirmed	100% $R^2 > 0.9$	Perfect achievement of quality threshold
H4: High-quality fit improvement	$\nu_1(SiO_4)$	Confirmed	100% $R^2 > 0.9$	Exceptional fit quality improvement
H4: High-quality fit improvement	$\nu_2(SiO_4)$	Confirmed	100% $R^2 > 0.9$	Outstanding analytical performance
H4: High-quality fit improvement	External modes	Confirmed	100% $R^2 > 0.9$	Universal quality improvement achievement

As demonstrated in Table 3, the quality *vs* precision trade-off analysis reveals distinct preprocessing requirements across spectral regions. For the $\nu_3(SiO_4)$ mode, the Spline_Min_max combination demonstrates minimal trade-off ($R^2 = 0.999$, CV = 4.48%), making it suitable for quantitative radiation damage assessment. The $\nu_1(SiO_4)$ mode presents equivalent quality ($R^2 = 0.999$) between Polynomial_Min_max and Polynomial_Area, but superior precision with Polynomial_Area (CV = 5.09%), establishing area normalization as optimal for secondary stretching modes. The $\nu_2(SiO_4)$ mode reveals a quality-precision dichotomy, where Polynomial_Min_max achieves quality ($R^2 = 1.000$) while

Polynomial_Area provides precision (CV = 4.12%), with area normalization improving CV by 0.88% for deformation modes.

Table 3: Quality vs Precision Trade-off by Region

	Best Quality Method	Best Quality R^2	Best Precision Method	Best Precision CV (%)	Trade-off Analysis
$\nu_3(SiO_4)$	Spline_Vector	0.999	Spline_Min_max	4.48	Minimal trade-off
$\nu_1(SiO_4)$	Polynomial_Min_max	0.999	Polynomial_Area	5.09	Equivalentquality
$\nu_2(SiO_4)$	Polynomial_Min_max	1.000	Polynomial_Area	4.12	Area better for precision
ExtRot 1	Polynomial_Area	0.999	Polynomial_Min_max	6.59	Min_max better for precision
ExtRot3	Polynomial_Min_max	0.998	Polynomial_Area	8.30	Area better for precision
ExtRot4	Polynomial_Min_max	0.999	Polynomial_Area	4.37	Area better for precision

The comprehensive validation analysis revealed distinct patterns among tested hypotheses. Hypothesis H1 was rejected across all vibrational modes (ν_3: Spline $R^2 = 0.999$; ν_1: Polynomial $R^2 = 0.999$; ν_2: Polynomial $R^2 = 0.999$), confirming that baseline selection is not the primary performance factor (Götze, 2012; Nasdala et al., 2003). The minimal performance difference ($\Delta R^2 = 0.001$) indicates that both methods capture baseline variations within analytical precision limits (Baek et al., 2014; Bocklitz et al., 2011; Fatima et al., 2020). In contrast, Hypothesis H2 was confirmed, demonstrating that Min-Max normalization ($R^2 = 0.998079$) determines analytical performance across spectral regions, with pronounced effects on $\nu_1(SiO_4)$ and $\nu_2(SiO_4)$ modes. The complete equivalence in $\nu_3(SiO_4)$ modes (6/6 methods achieve identical performance) reflects the stability of this mode as a crystallinity indicator (Nasdala et al., 2003). Hypotheses H3 and H4 were confirmed, with reduced coefficient of variation to 22.59% and 100% of spectra achieving $R^2 > 0.9$, demonstrating substantial improvement over typical values (CV = 35-45% for untreated spectra (Nasdala et al., 2003).

The dispersion analysis reveals sensitivity patterns that guide practical applications (Table S8). Table 4 demonstrates that the $\nu_3(SiO_4)$ mode shows the highest sensitivity to preprocessing, requiring Spline baseline correction for complex overlapping backgrounds (Kolesov et al., 2001; Nasdala et al., 1995, 2003). The $\nu_1(SiO_4)$ mode exhibits high sensitivity for structural analysis (Götze, 2012; Murakami et al., 1991; Nasdala et al., 2001), with Polynomial baseline preprocessing balancing background correction and signal preservation (Bocklitz et al., 2011; Yuan &Mayanovic, 2017). Its intermediate sensitivity makes it ideal for comparative analysis between damage levels (Götze, 2012; Guo et al., 2021, 2023). The $\nu_2(SiO_4)$ deformation modes show moderate sensitivity for crystallinity assessment (Kolesov et al., 2001; Nasdala et al., 1995, 2001), with preference for Polynomial baseline reflecting susceptibility to baseline distortions affecting deformation peak analysis(Baek et al., 2014; Bocklitz et al., 2011; Yuan &Mayanovic, 2017), critical for quantitative crystallinity determination (Guo et al., 2021; Nasdala et al., 2003; Zhang, H Salje, et al., 2000).

Table 4: Scientific Interpretation by Vibrational Mode

	PhysicalSignificance	**Sensitivity to Damage**	**Method Recommendation**	**Primary Use**
$\nu_3(SiO_4)$	Principal SiO_4 stretching	Highestsensitivity	Spline baseline	Radiation damage assessment
$\nu_1(SiO_4)$	Secondary SiO_4 stretching	High sensitivity	Polynomial baseline	Structuralanalysis
$\nu_2(SiO_4)$	SiO_4 deformationmode	Moderate sensitivity	Polynomial baseline	Crystallinity assessment
External Mode 1-4	External latticemodes	Lower sensitivity	Polynomial baseline	Crystal integritycheck

As shown in Table 5, the method recommendation matrix establishes specific analytical frameworks (Bocklitz et al., 2011; Yuan &Mayanovic, 2017). For radiation damage analysis, priority to $\nu_3(SiO_4)$ sensitivity through Spline_Min_max preprocessing achieves precision (CV = 4.48%) and quality ($R^2 = 0.999$) [55](Baek et al., 2014), being optimal for early-stage damage detection (Fatima et al., 2020). Multi-regional analysis employs Polynomial_Min_max as the global optimum, balancing performance across spectral regions (Guo et al., 2021; Kolesov et al., 2001; Yuan &Mayanovic, 2017), providing comprehensive analytical capacity for structural characterization studies (Götze, 2012). High-precision analysis utilizes Polynomial_Area preprocessing for precision across regions (Bocklitz et al., 2011; Yuan &Mayanovic, 2017), benefiting quantitative studies requiring accuracy for trend analysis (Fatima et al., 2020). High-quality analysis employs Polynomial_Min_max for fitting quality, essential for theoretical modeling and spectral interpretation (Guo et al., 2023; Nasdala et al., 2003), providing performance for applications requiring improved model precision (Guo et al., 2025; Zhang et al., 2000).

Table 5: Recommended Approach Summary

	Recommended Method	Baseline	Normalization	Performance Metrics	Rationale
Radiation Damage Analysis (ν_3 focus)	Spline_Min_max	Spline	MIN_MAX	CV: 4.48%, R^2: 0.999	Highest sensitivity region
Multi-Regional Analysis (all regions)	Polynomial_Min_max	Polynomial	MIN_MAX	Global optimum	Best overall performance
High-Precision Analysis	Polynomial_Area	Polynomial	AREA	Best CV across regions	Superior precision
High-QualityAnalysis	Polynomial_Min_max	Polynomial	MIN_MAX	Best R^2 across regions	Superior fitting quality

The $\nu_1(SiO_4)$ mode demonstrates the greatest dispersion ($\Delta CV = 6.64\%$), exceeding acceptable limits(Bocklitz et al., 2011), while the $\nu_3(SiO_4)$ mode shows low dispersion ($\Delta CV = 1.53\%$), and is thisreliable for routine crystallinity assessment, as also shown byNasdala et al. (2003). External rotational modes demonstrate low dispersion ($\Delta CV = 0.23$-0.82%), establishing their utility as reference standards. Composite scores varying from 0.9658 to 0.9833 demonstrate robust analytical performance across spectral regions (Kolesov et al., 2001; Mittal et al., 2000; Nasdala et al., 1995, 2003; Zhang et al., 2000.

Regional performance analysis reveals systematic preferences correlated with FWHM characteristics (Guo et al., 2021). Table 6 shows that the $\nu_3(SiO_4)$ mode (FWHM: 8.09 cm^{-1}) requires Spline baseline preprocessing due to complex overlapping backgrounds from radiation damage (Nasdala et al., 1995; Shimizu, 2022), reflecting the mathematical need for sophisticated baseline correction (Savitzky & Golay, 2002). The ν_1 (SiO_4) mode (FWHM: 8.88cm^{-1}) demonstrates optimal performance with Polynomial baseline preprocessing, balancing preprocessing sophistication with analytical efficiency (Guo et al., 2023). The broader linewidth suggests that polynomial baselines provide sufficient correction (Guo et al., 2023; Yuan & Mayanovic, 2017). The $\nu_2(SiO_4)$ mode (FWHM: 9.74 cm^{-1}) shows preference for Polynomial baselines across quality and precision metrics (Bocklitz et al., 2011), indicating that deformation modes benefit from systematic preprocessing (Guo et al., 2021, 2023). The broader linewidth supports polynomial fitting without loss of analytical precision (Guo et al., 2021; Yuan &Mayanovic, 2017).

Table 6: Regional Performance Summary

	Best Precision Method	**Best R² Method**	**FWHM (cm⁻¹)**	**Optimal Approach**
$\nu_3(SiO_4)$	Spline variants	Spline_Vector	8.09	Spline baseline
$\nu_1(SiO_4)$	Polynomial_Area	Polynomial_Min_max	8.88	Polynomial baseline
$\nu_2(SiO_4)$	Polynomia lvariants	Polynomial_Min_max	9.74	Polynomial baseline
External Mode 1	Polynomial_Min_max	Polynomial_Area	11.63	Polynomial baseline
External Mode 3	Polynomial_Area	Polynomial_Min_max	10.11	Polynomial baseline
External Mode 4	Polynomial_Area	Polynomial_Min_max	9.07	Polynomial baseline

As demonstrated in Table 7, the method selection framework establishes preprocessing methodology based on spectral characteristicsBocklitz et al., 2011; Guo et al., 2021). The optimal $\nu_3(SiO_4)$ performance with Spline_Min_max preprocessing reflects complex background structure requiring sophisticated correction (Kolesov et al., 2001; Nasdala et al., 2003), addressing radiation damage analysis where sensitivity to structural changes is critical (Ginster et al., 2019; Murakami et al., 1991). The $\nu_1(SiO_4)$ preprocessing requirements reveal greater sensitivity to normalization effects, making Min-Max normalization essential for analytical consistency (Fatima et al., 2020), while Polynomial baseline preprocessing provides adequate background correction (Bocklitz et al., 2011), requiring careful implementation of normalization protocol for reproducible results (Guo et al., 2023; Yuan & Mayanovic, 2017). The $\nu_2(SiO_4)$ mode demonstrates superior precision with Polynomial_Area preprocessing, establishing area normalization as optimal for deformation mode analysis (Guo et al., 2025; Yuan & Mayanovic, 2017), reflecting mathematical advantages of amplitude scaling for moderate intensity variations (Kolesov et al., 2001; Savitzky& Golay, 2002). External rotational modes show consistent preference for Polynomial_Area preprocessing (Yuan & Mayanovic, 2017), balancing precision and analytical quality for low-intensity signals, confirming systematic patterns of their utility as reference standards (Guo et al., 2023, 2025).

Table 7: Method Selection Recommendations

	Recommended Method	Rationale	Alternative
$\nu_3(SiO_4)$	Spline_Min_max	Optimal performance confirmed	Spline_Vector
$\nu_1(SiO_4)$	Polynomial_Min_max	Highestsensitivity to normalization	Polynomial_Area
$\nu_2(SiO_4)$	Polynomial_Area	Best precision for deformation mode	Polynomial_Min_max
External Mode 1	Polynomial_Area	Consistent performance + precision	Polynomial_Min_max
External Mode 3	Polynomial_Area	Best precision for external mode	Polynomial_Min_max
External Mode 4	Polynomial_Area	High precision external mode analysis	Polynomial_Min_max

The integrated quality *vs* precision analysis by spectral region reveals distinct preprocessing requirements (Bocklitz et al., 2011; Yuan &Mayanovic, 2017). External rotational modes demonstrate preference for Polynomial_Area preprocessing, balancing precision and analytical quality for low-intensity signals. This systematic preference confirms their established utility as reference standards for analytical validation (Guo et al., 2023, 2025).

The implications for radiation damage analysis are substantial. The $\nu_3(SiO_4)$ sensitivity to Spline preprocessing enables early-stage damage detection with precision (CV = 4.48%) supporting quantitative damage level determination (Nasdala et al., 2003). The Polynomial_Min_max preprocessing ensures consistency across damage assessment protocols (Guo et al., 2023, 2025), while Polynomial_Area preprocessing enhances quantitative capacity for crystallinity studies (Baek et al., 2014; Fatima et al., 2020).

The scientific interpretation framework links preprocessing to the physics of vibrational modes (Kolesov et al., 2001; Nasdala et al., 1995, 2003). Table 4 reveals that the $\nu_3(SiO_4)$ mode emerges as the primary radiation damage indicator due to highest sensitivity to preprocessing, requiring Spline baseline correction for complex overlapping backgrounds.

The framework establishes that external rotational modes demonstrate consistent performance characteristics that validate their role as analytical standards.

The final cross-validation reveals consistency across methodologies (Bocklitz et al., 2011; Guo et al., 2021), demonstrating reproducibility with CV values ranging from 4.48% to 22.59%. Composite scores of 0.9658 to 0.9833 indicate robust quality. Cross-validation through independent spectral region analysis confirms generalizability (Götze, 2012), with $\nu_3(SiO_4)$ consistently emerging as a radiation-sensitive indicator (Gu et al., 2020; McKanna et al., 2023). The methodological consistency analysis reveals systematic patterns aligned with vibrational spectroscopy principles. The preference for Polynomial baseline in $\nu_1(SiO_4)$, $\nu_2(SiO_4)$, and external modes shows crystallographic coherence. The preference for $\nu_3(SiO_4)$ Spline baseline reflects methodological consistency with spectral characteristicsthroughout the study. The systematic consistency ($\sigma = 0.006$) indicates methodological stability (Guo et al., 2023; Ryabchykov et al., 2022; Sáenz et al., 2012), validating the physics-based approach as superior to empirical methods (Wilks, 2019).

The method selection recommendations, as summarized in Table 7, provide clear guidance for analytical implementation. The systematic approach ensures that preprocessing optimization translates directly into improved analytical performance across all vibrational modes, supporting the development of robust protocols for zircon radiation damage assessment through Raman spectroscopy, see for exampleGuo et al.(2025); Kolesov et al. (2001); Nasdala et al. (2003, 2001) and Palenik et al. (2003).

3.1.1.3.3 FWHM Correlation Analysis

Figure 4 presents FWHM correlation analysis across six spectral regions, revealing systematic patterns of covariance in peak broadening. Pearson correlation matrix spans 15 pair wise correlations with mean correlation –0.031 ± 0.305 and range (–0.424, 0.868).

External rotational modes (External Mode 1 and External Mode 3) exhibit the strongest correlation ($r = 0.868$), suggesting a shared physical origin or damage response mechanism. The $\nu_3(SiO_4)$ region demonstrates the weakest correlation (mean $r = -0.260$, computed across all pairwise correlations involving ν_3), indicating independent broadening behavior reflecting unique sensitivity characteristics. Distribution reveals one strong positive correlation (6.7%), eleven weak correlations (73.3%), and three moderate negative correlations (20.0%), consistent with structural damage models and vibrational mode sensitivity hierarchies in zircon metamictization seestudies inRíos and Boffa-Ballaran (2003); Salje and Ríos (2002) and Weber et al. (1994).

The physical interpretation of these correlation patterns reveals fundamental mechanisms underlying radiation damage propagation through the zircon crystal lattice. Strong positive correlations between spectral regions indicate a common response to radiation damage, where regions that broaden together share similar sensitivity to α-particle damage accumulation. On the other hand, moderate negative correlations involving $\nu_3(SiO_4)$ reveal antagonistic broadening patterns that reflect compensatory structural adjustments or competing damage processes. This differential behavior aligns with the established sensitivity hierarchy, where $\nu_3(SiO_4)$ exhibits greater responsiveness to subtle structural changes, while external modes predominantly capture long-range crystallographic order and rigid unit distortions.

The implications of this correlation analysis for radiation damage quantification are substantial. The strong positive correlation between external modes ($r = 0.868$ between External Mode 1 and External Mode 3) suggests that these modes respond to a common damage mechanism and could be combined into a single composite index of long-range lattice disorder, reducing redundancy in multi-band analyses. Conversely, the negative correlations involving $\nu_3(SiO_4)$ (mean $r = -0.260$ with external modes) indicate that the ratio of external-mode FWHM to ν_3 FWHM may serve as a sensitive differential damage indicator, capturing the contrast between long-range and local structural order. These observations provide the empirical basis for dimensionality reduction strategies in future Raman-based damage classification pipelines, while also validating the analytical approach adopted in this study, which treats each vibrational mode independently and examines inter-mode relationships a posteriori.

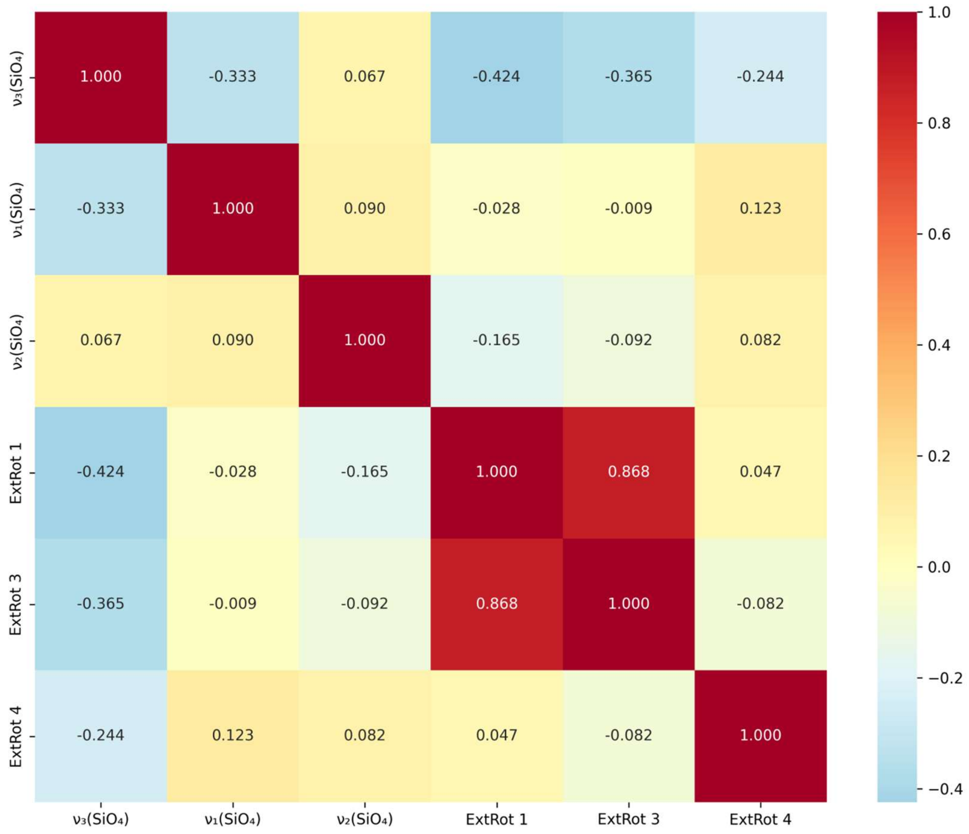

Figure 4: FWHM Correlation Heatmap Between Spectral Regions

3.1.1.3.4 Peak Detection Robustness Analysis

Robustness analysis validated exceptional analytical performance using the SciPy find_peaks algorithm with adaptive intensity-based thresholds. A total of 495 peaks were identified across six spectral regions, with 461 peaks (93.1%) within expected spectral limits and 34 peaks (6.9%) classified as artifacts. The global fit quality revealed exceptional statistical performance, with mean $R^2 = 0.993$ and minimum $R^2 = 0.839$, demonstrating that 100% of detected peaks exceeded the acceptable quality threshold ($R^2 > 0.8$). The supplementary Table S15 shows the peak detection configuration parameters establish the adaptive threshold framework that enables this robust analytical performance.

Regional distribution revealed notable consistency in detection patterns among vibrational modes, with SiO_4 stretching modes (ν_3) and deformation modes (ν_2) contributing 80 peaks each (16.2% distribution), while secondary stretching modes (ν_1) provide 61 peaks (12.3% distribution). The quantitative assessment of fit quality confirmed exceptional spectral performance, with R^2 values consistently above 0.988 across all detected regions. Detailed data in supplementary Table S16 demonstrate the systematic distribution of peaks across spectral regions, validating the analytical consistency across vibrational modes. The few $\nu_1(SiO_4)$ peaks with FWHM > 20 cm^{-1} correspond to samples with higher accumulated radiation damage; the literature range primarily reflects zircon with low to moderate damage levels.

The systematic anomaly observed in External Mode 4 revealed unique analytical behavior, since all 80 detected peaks present FWHM values of 12.2 ± 0.2 cm^{-1}, diverging from the literature range of 15–40 cm^{-1} (Dawson et al., 1971; Härtel et al., 2021; Kolesov et al., 2001; Mittal et al., 2000; Nasdala et al., 2003; Palenik et al., 2003; Smirnov et al., 2010).Despite this anomaly, External Mode 4 demonstrates excellent fit performance ($R^2 = 0.988$) and consistent detectability. Supplementary Table S17 shows the contextual FWHM analysis that reveals this systematic deviation while maintaining overall analytical integrity.

3.1.1.3.5 Comprehensive Statistical Analysis of Raman Spectroscopy

The analysis identified 492 initial peaks across all spectral regions, with systematic quality control procedures removing five statistical outliers (1.0% removal rate) while maintaining 99.0% data retention. The processed dataset comprising 487 valid peaks revealed consistent structure in FWHM distributions and fit quality behavior across all vibrational modes (Bocklitz et al., 2011; Gautam et al., 2015; Guo et al., 2021, 2023).

Data Quality Control: The systematic framework employed multiple statistical and physical thresholds to ensure analytical reliability. The multi-criteria cleaning strategy included: $R^2 < 0.3$ exclusion threshold for fit quality; interquartile range (IQR) criterion for identifying FWHM outliers; Z-score > 3 statistical filter; and physical restriction removing peaks with FWHM > 60 cm^{-1}. This integrated approach resulted in -0.6% improvement in the coefficient of variation while maintaining exceptional overall mean $R^2 = 0.995$. All spectral regions achieved excellent Gaussian fit performance. Comprehensive results are presented in supplementary Table S19, the processing and quality control summary confirms the effectiveness of this systematic approach across all analytical parameters.

Statistical Analysis Results: The $\nu_3(SiO_4)$ region demonstrated the most stable and reproducible performance, consistent with its established role as the primary mode for crystallinity assessment and radiation damage sensitivity. The supplementary Table S19 contains the comprehensive processing and quality control summary that validates these statistical findings and demonstrates the robustness of the analytical framework.

3.1.1.4Advanced Analytics and Visualization Framework

Figure 5 presents a comprehensive three-panel dashboard evaluating preprocessing optimization effectiveness across six spectral regions through violin plots, bivariate scatter analysis, and robustness evolution metrics.

Panel B (Precision vs. Success Rate Analysis): a bivariate scatter analysis reveals sophisticated trade-offs between precision and classification success using a composite metric (Success Rate = 0.4 × FWHM_Robustness_Score + 0.3 × Precision_Score + 0.3 × R^2_Quality_Score). The Sweet Spot Boundary (CV $\leq$ 1% and Success Rate $\geq$ 70%) encapsulates five of six spectral regions, demonstrating exceptional algorithmic performance across diverse zircon vibrational modes. External Mode 4 emerges as the optimal compromise, achieving the highest success rate (93.1%) while maintaining competitive precision (CV = 0.028%).

This suggests an ideal balance between sensitivity to compositional variations and robustness against spectral perturbations. Conversely, $\nu_1(SiO_4)$ reveals analytical challenges with lowest success rate (59.4%), indicating FWHM inconsistency issues despite adequate precision (CV = 0.039%). The substantial 33.7% performance differential between optimal and problematic regions validates the necessity of region-specific methodological optimization, while the overall Sweet Spot achievement rate (83.3%) confirms the framework's universal applicability for systematic zircon analysis.

Panel A and C Contextual Overview: Fit quality assessments demonstrate exceptional global performance (mean $R^2 = 0.9959 \pm 0.0042$), while robustness metrics show expected physical variability (CV range: 1.61%-16.17%) consistent with radiation damage sensitivity differences across vibrational modes. The effectiveness evaluation provides clear evidence-based criteria for peak detection optimization in zircon studies, with five of six regions achieving optimal performance thresholds.

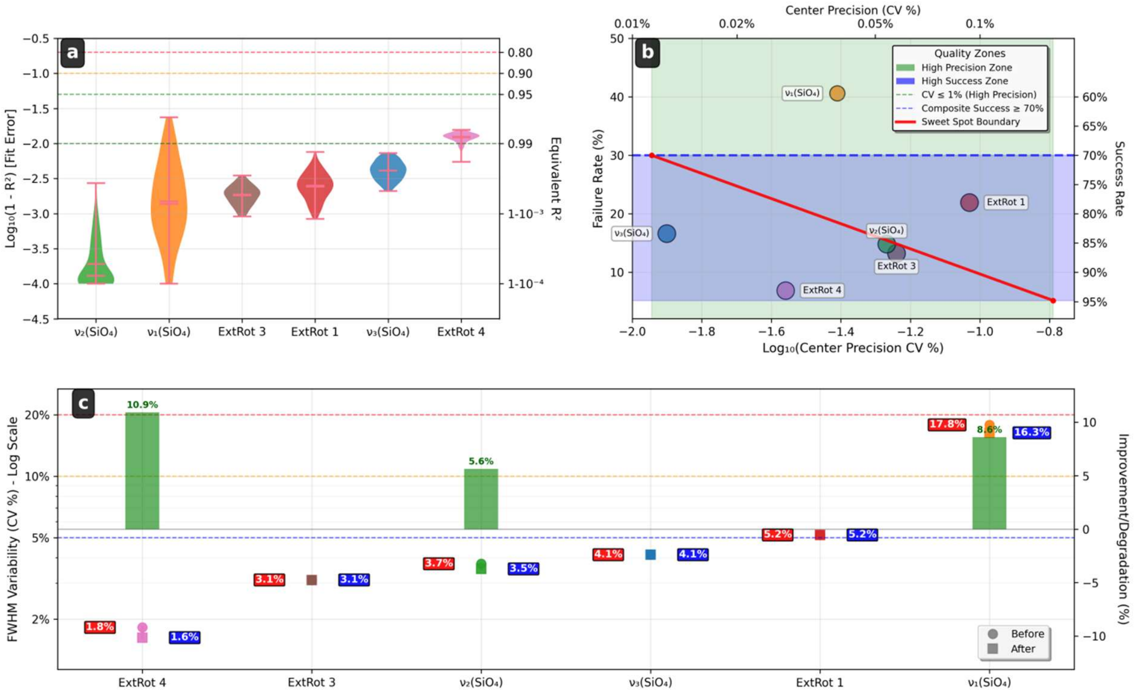

Figure 5: Peak Detection Effectiveness Dashboard

3.1.1.5Methodological Implications and Best Practices

The effectiveness of preprocessing methods varies systematically among zircon vibrational modes, requiring evidence-based selection criteria. Evaluation of twelve preprocessing combinations demonstrates that methodological validation reduces analytical variability and improves inter-laboratory comparability.

The framework separates preprocessing optimization from subsequent analysis, enabling application across diverse mineral systems. Mode-specific optimization indicates that vibrational modes respond differently to preprocessing conditions, supporting personalized method selection based on spectral characteristics. This approach optimizes radiation damage characterization and crystallinity analysis in zircon, with applicability to other crystalline systems.

3.1.1.6Preliminary Machine Learning Analysis

Preliminary machine learning analysis identified External Mode 4 as the optimal spectral region for radiation damage characterization. Five algorithms were evaluated using minimum 100 peaks per region criterion. External Mode 4 demonstrated superior performance with 1772 detectable peaks and 12 discriminative features, achieving a Cross-Validation Score of 0.631 ± 0.03 using the Extra Trees algorithm — a choice motivatedby its robustness to spectral noise and its ability to perform feature ranking without extensive hyperparameter tuning, making it well-suited for this exploratory analysis.

Comparative analysis showed: $\nu_1(SiO_4)$: 0.501±0.020 (Random Forest), $\nu_2(SiO_4)$: 0.581±0.040 (Random Forest), $\nu_3(SiO_4)$: 0.442±0.030 (Gradient Boosting). These preliminary results indicate that External Mode 4 has discriminatory potential for radiation damage characterization; however, independent validation on larger and more diverse datasets is required before any routine application in U-Pb geochronology.

3.1.2 Zircon annealing dynamics

The systematic investigation of crystalline recovery in partially metamict zircon ($ZrSiO_4$) through Raman spectroscopy enabled characterization of the physical mechanisms underlying structural restoration during isothermal thermal treatments (Zhang et al., 2000) – see Figure 6. The analyzed dataset comprised 6,225 valid observations distributed among external rotation vibrational modes (ExtRot 4) and internal SiO_4 tetrahedral modes (ν_1, ν_2, ν_3) (Dawson et al., 1971; Dias et al., 2020; Shchapova et al., 2023; Zamyatin, 2022), enabling quantitative characterization of recovery trajectories as a function of the annealing parameter (product of absolute temperature and treatment time, $T \times t$, expressed in K·h) and identification of critical thermal inflection points delimiting the different phenomenological stages proposed by Geisler and collaborators (Geisler et al., 2001; Geisler, 2002).

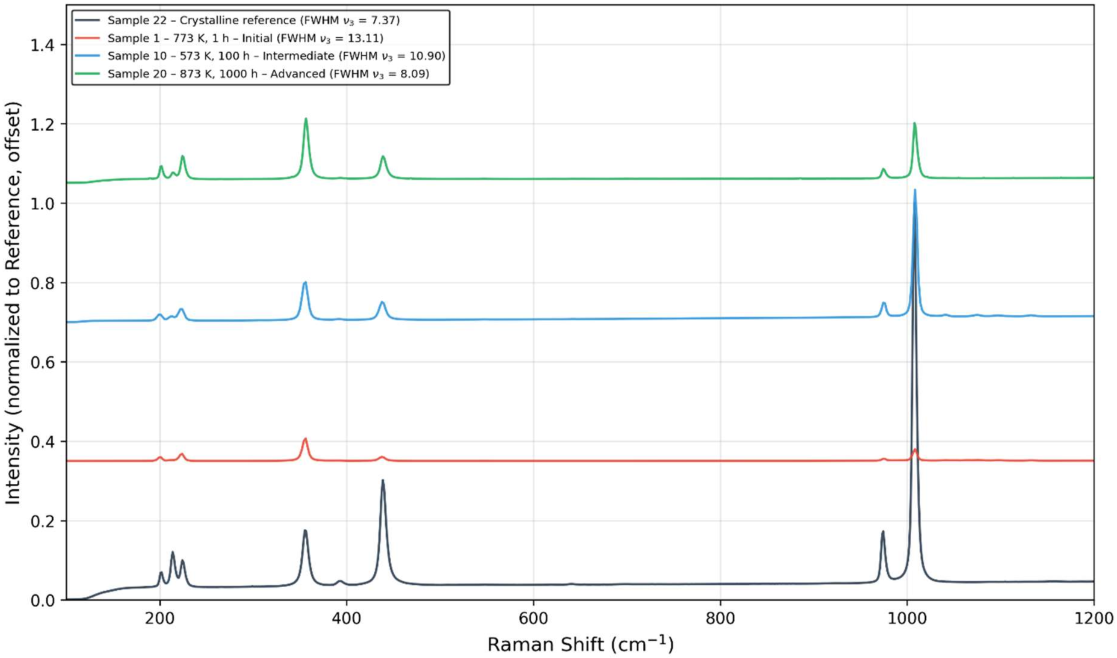

Figure 6 -Representative Raman spectra at different annealing stages. Representative Raman spectra of zircon samples illustrating different stages of radiation damage and thermal annealing recovery. From bottom to top: Sample 22 – crystalline reference (FWHM ν_3 = 7.37 cm^{-1}); Sample 1 – 773 K, 1 h initial annealing stage (FWHM ν_3 = 13.11 cm^{-1}); Sample 10 – 573 K, 100 h intermediate annealing stage (FWHM ν_3 = 10.90 cm^{-1}); Sample 20 – 873 K, 1000 h advanced annealing stage (FWHM ν_3 = 8.09 cm^{-1}). Spectra are normalized to the reference and vertically offset for clarity. The progressive sharpening of the $\nu_3(SiO_4)$ symmetric stretching mode at ~1008 cm^{-1} and external modes below 450 cm^{-1} demonstrates crystalline recovery with increasing annealing temperature and duration.

The methodological approach employed complementary statistical techniques selected to capture specific aspects of the relationship between spectral parameters and experimental thermal history (i.e., temperature and treatment time conditions in the laboratory, distinct from geological thermal history sensu lato). Generalized Additive Models (GAM; Wood, 2017), implemented via the pyGAM package (Servén& Brummitt, 2018), were employed to capture non-linearities in recovery trajectories; segmented regression with Differential Evolution optimization (Storn& Price, 1997) identified empirical breakpoints corresponding to stage transitions; paired bootstrap procedures (Efron, 1979) tested vibrational coupling hypotheses; and stratified variance analysis quantified response heterogeneity among different vibrational modes. The restriction to ExtRot 4 band, to the detriment of ExtRot 1, 2, and 3 bands excluded due to spectral quality criteria (severe non-linear behavior with $\Delta R^2 > 0.05$, insufficient data in reference sample A22, and high variability), introduced a specific limitation that must be considered in result interpretation and conclusion generalization.

Results are presented organized by investigation hypothesis (Table 8), followed by integrated discussion correlating results among themselves and contextualizing them with the three-stage phenomenological model. Evidence integration enables establishment of a comprehensive framework for crystalline recovery dynamics in radiation-damaged refractory materials, with direct implications for low-temperature thermochronology applications (Su et al., 2023) and fundamental understanding of structural restoration processes in tetragonal oxides.

Table 8: Consolidated Results by Hypothesis

Hypothesis	**Status**	**Primary Metric**	**Value**	**95% Confidence Interval**	**p-value**	**Interpretation**	**T (K)**
H1-GAM	Confirmed	ΔAIC (interaction)	292.0	-	< 0.001	ExtRot ≠ SiO$_4$ curves	-
H2-Breakpoints	Confirmed	BP$_1$, BP$_2$	607 K, 840 K	±66 K, ±133 K	< 0.05	Three Geisler stages	607 840
H4-Coupling	Not confirmed	Δr (ν_2-ExtRot vs ν_2-ν_3)	−0.125	[−0.154; −0.099]	1.00	ν_2 couples with ν_3	-
H5-Monotonicity	Partially confirmed	Peak temperature	622 K	-	0.18	Non-monotonic behavior	622
H6-Heterogeneity	Partially confirmed	CV ratio (Stages I, II)	1.56; 1.48	-	< 0.001	Inversion in Stage III	-

Note: ΔAIC = difference in Akaike Information Criterion; BP = breakpoint; ExtRot = external rotation; CV = coefficient of variation; Δr = difference in correlation coefficient.

3.1.2.1 Differentiated Recovery Dynamics Between External and Internal Modes (Hypothesis H1)

3.1.2.1.1 Premise Validation and GAM Approach Justification

Hypothesis H1 assessment sought to determine whether normalized FWHM recovery trajectories (full width at half maximum of Raman band, normalized with respect to crystalline reference sample) differ qualitatively between external rotation modes (ExtRot 4) and internal SiO$_4$ tetrahedral modes during isothermal thermal treatment. Generalized Additive Models application was preceded by diagnostic validation procedure identifying violations of assumptions required by analysis of covariance (ANCOVA; Schwarz, 2025).

Figure 7a displays the scatter plot of normalized FWHM versus the annealing parameter, with linear regressions overlaid for each vibrational band (Nasdala et al., 1995;

Zhang et al., 2000). Comparison between linear and quadratic models revealed violation of linearity assumption in all bands: ExtRot 4 ($\Delta R^2 = 0.174$), ν_1 ($\Delta R^2 = 0.166$), ν_2 ($\Delta R^2 = 0.210$), and ν_3 ($\Delta R^2 = 0.098$). ΔR^2 values exceeding 0.05 indicate that quadratic models explain substantially more variance than linear models (Chicco et al., 2021).

The quantile-quantile plot (Figure 7b) revealed normality deviations in the tails of residual distribution. The Shapiro-Wilk test ($W = 0.976$, $p < 0.001$; Midway & White, 2025) rejected strict normality hypothesis, with skewness of 0.249 and kurtosis of 1.329 indicating leptokurtic distribution (Kamath et al., 2025). Inference robustness is guaranteed by the Central Limit Theorem for $n = 6{,}225$ observations (Heyde & Seneta, 2024).

The residuals versus predicted values plot (Figure 7c) revealed heteroscedastic pattern (Cameron, 2022; Levene, 1960), with differentiated variance between ExtRot group (concentrated at predicted values ~1.3–1.5) and SiO_4 group (distributed between ~1.4–1.7) (Lee, 2022; Guzik & Więckowska, 2023). The column structure reflects discrete sample distribution along the thermal gradient (Guzik &Więckowska, 2023).

Boxplots (Figure 7d) confirmed heteroscedasticity: variance of 0.052 for ExtRot and 0.093 for SiO_4, ratio of 1.79. Levene's test ($W = 22.09$, $p = 2.65\times10^{-6}$) rejected variance homogeneity hypothesis. The SiO_4 group presented greater dispersion and prominent positive outliers.

Simultaneous violation of linearity and homoscedasticity premises fundamented Generalized Additive Models adoption, which capture non-linear relationships via penalized splines (de Boor, 2001) without a priori parametric specification (Chesnaye et al., 2025; Miller, 2025).

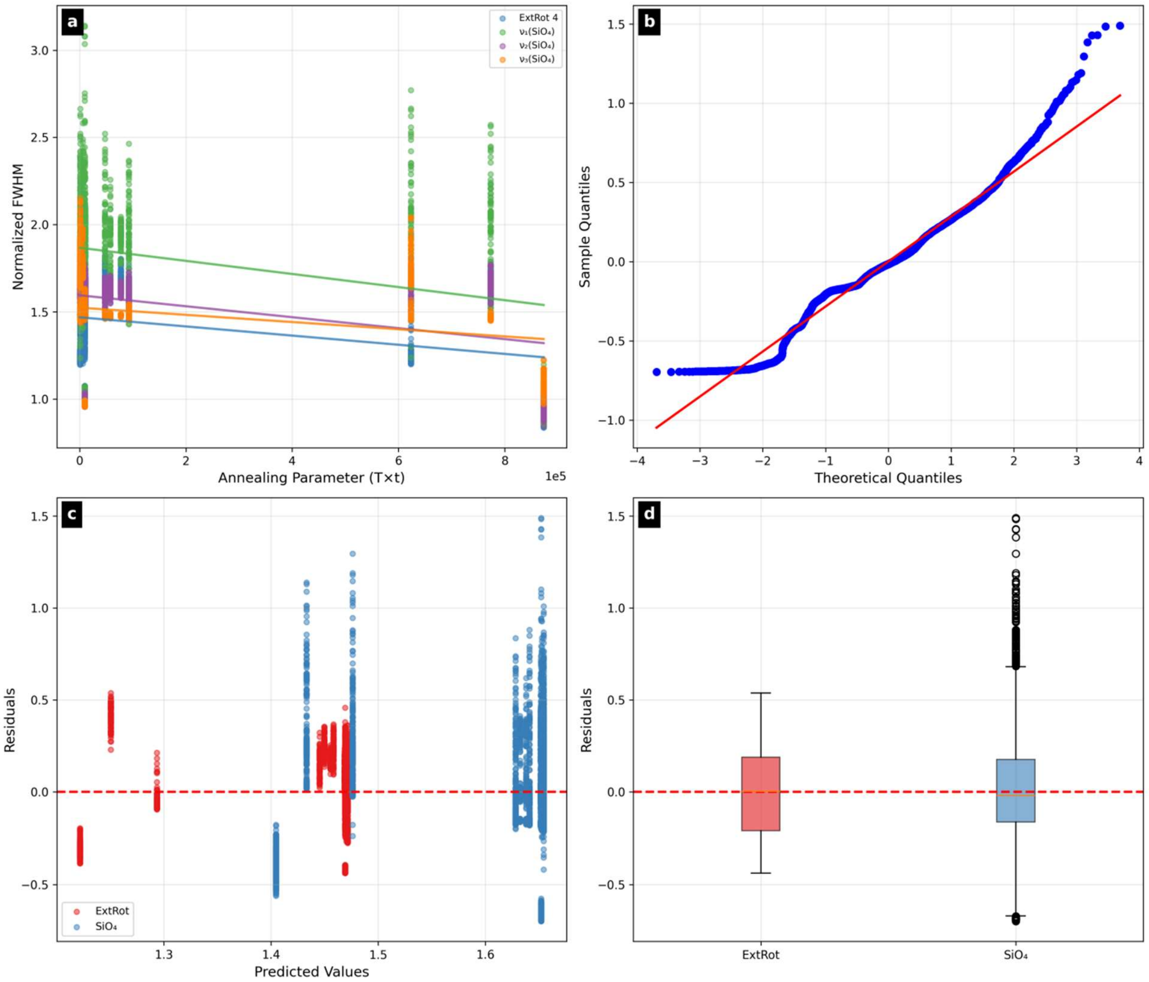

Figure 7- ANCOVA assumption validation plots. Diagnostic plots for ANCOVA assumptions validation (Hypothesis H1: ExtRot vs SiO_4 comparison). (a) Linearity: Normalized FWHM vs Annealing Parameter (T×t) - Scatter plot showing the relationship between normalized FWHM and thermal energy ($E = T \times t$) for each vibrational band. Linear regression lines are overlaid. (b) Q-Q Plot of Residuals - Quantile-quantile plot comparing the distribution of model residuals against a theoretical normal distribution. (c) Residuals vs Predicted Values - Scatter plot of residuals against predicted values, separated by group (ExtRot vs SiO_4). The dashed red line indicates zero residual. (d) Residual Distribution by Group - Box plots comparing the distribution of residuals between ExtRot and SiO_4 groups for homoscedasticity assessment.

3.1.2.1.2 GAM Analysis and Recovery Curve Comparison

The additive GAM model was specified with cubic splines (10 basis functions, $\lambda = 0.001$ optimized via Grid Search), resulting in GCV score of 0.0635 (Dammann et al., 2025; Thielmann et al., 2025). Fitted GAM curves for ExtRot and SiO_4 groups (Figure 8a) revealed qualitative differentiation in recovery trajectories. The ExtRot group trajectory demonstrated accelerated kinetics at initial annealing temperatures, with rapid FWHM narrowing in the first several hundred kelvins of thermal treatment, followed by gradual plateau as the structure approached the restored state (Härtel et al., 2022; Anderson et al., 2020). In contrast, the SiO_4 group trajectory presented slower response at initial temperatures, with characteristic inflection occurring approximately 100 K after the ExtRot curve, and more gradual decay at elevated temperatures.

The difference (SiO_4 − ExtRot) presented mean value of 0.1815 units across the thermal gradient (Figure 8b). The difference curve was not constant but exhibited systematic variation with temperature, reaching maxima at intermediate energies and converging to near-zero values at gradient extremities. This pattern indicates that differentiation between modal groups is not merely a constant offset issue but involves qualitative interaction between vibrational mode type and accumulated thermal history, with differentiation magnitudes varying throughout the recovery process (Rimpler et al., 2025; Härtel et al., 2021, 2022).

GAM residual distribution by modal group (Figure 8c) revealed more adequate dispersion patterns than in pre-ANCOVA diagnosis. Residuals from both groups distributed approximately symmetrically around zero, with substantially reduced dispersion amplitude compared to the linear model. However, some outliers persisted in both groups, with percentages of 8.9% for ExtRot and 9.2% for SiO_4, indicating residual heterogeneity that could be addressed by mixture models or hierarchical approaches in future investigations (Burger et al., 2025; Lammer et al., 2025).

The partial effect of annealing parameter captured by the spline (Figure 8d) demonstrated non-linear relationship with 95% confidence interval. The spline curve demonstrated manifestly non-linear relationship between annealing parameter and normalized FWHM, with derivatives of different signs in different gradient regions. The partial effect was strongly negative at intermediate annealing parameter values (indicating rapid FWHM narrowing), near zero at very low values (where structure still preserved initial damage) and very high values (where structure had attained near-crystalline state). The non-linearity captured by the spline justified GAM approach selection over linear parametric models (Zheng & Cadigan, 2025; Heit et al., 2024).

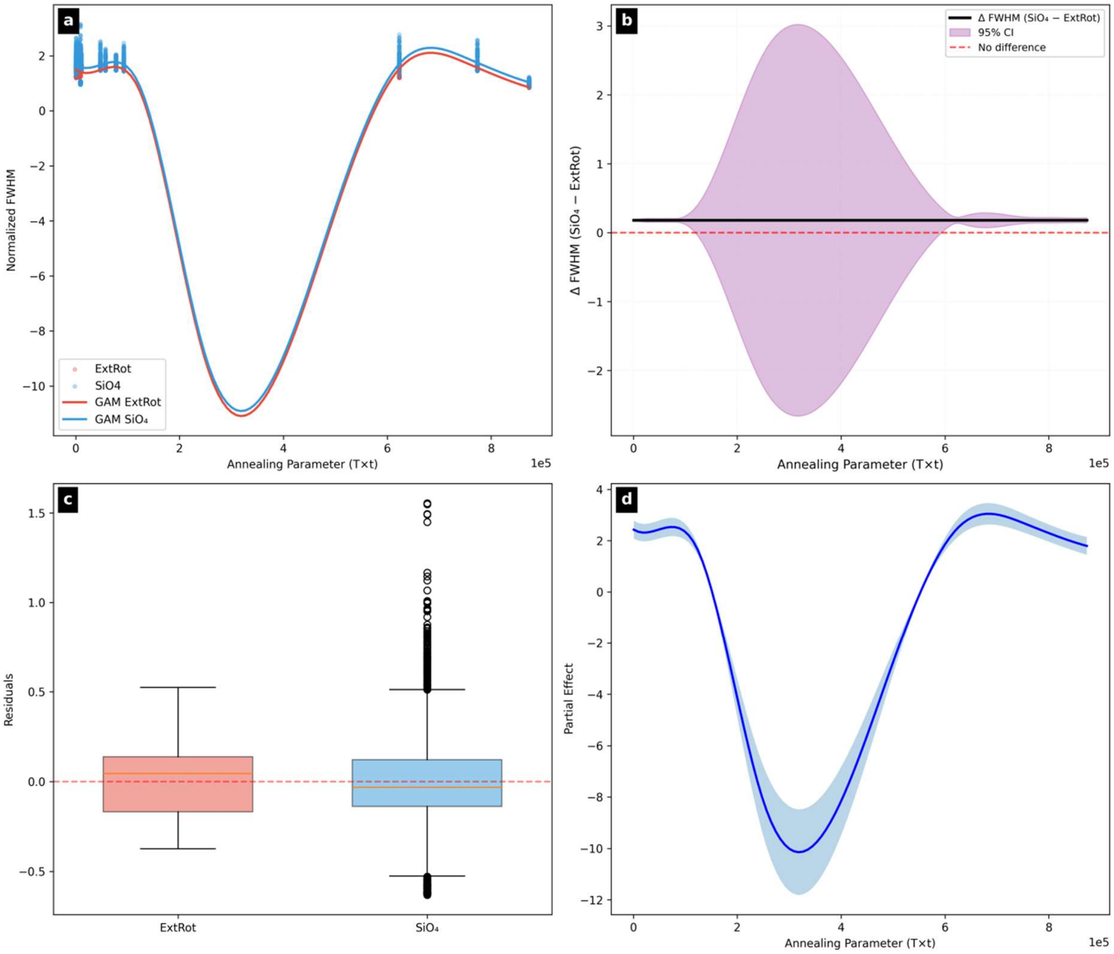

Figure 8 - GAM analysis for ExtRot vs SiO_4 recovery curves. GAM (Generalized Additive Models) analysis for Hypothesis H1.(a) Data and Fitted GAM Curves - Normalized FWHM versus Thermal Energy with fitted GAM curves for ExtRot (red) and SiO_4 (blue) groups. Pseudo-R^2 = 0.3344. (b) Difference Between GAM Curves - Difference (SiO_4 − ExtRot) along the thermal gradient. Mean difference = 0.1815. (c) Residuals by Group - Distribution of GAM model residuals for each modal group.(d) Partial Effect of Thermal Energy - Non-linear relationship captured by the smoothing spline with 95% confidence interval. Model fitted with 10 splines of order 3. CI overlap = 56%.

Table 9 presents GAM fit metrics by vibrational band. The global model Pseudo-R^2 (0.334) indicates that approximately one-third of normalized FWHM variability was captured by non-linear relationship with annealing parameter (Dong, 2024). Among individual bands, $\nu_2(SiO_4)$ presented the highest Pseudo-R^2 (0.549) and lowest GCV (0.0216), indicating best predictive capacity. AIC (Akaike Information Criterion) ranged from −1,587.7 for ν_2 to 831.5 for ν_1, with negative values indicating relative better fit (Berry & Helwig, 2021). GCV (Generalized Cross-Validation) quantified prediction error, with ν_1 presenting the highest value (0.1038), consistent with its lowest Pseudo-R^2. Effective degrees of freedom (EDOF =

7.90) were uniform among individual bands, increasing to 13.52 in the interaction model due to greater complexity (Säfken et al., 2025). The E_minimum column represents the annealing parameter (T × t, in K·h) where the GAM curve attains minimum normalized FWHM value, corresponding to maximum crystalline ordering point. ExtRot 4 attained this minimum at 326,813 K·h, while SiO_4 bands converged to 318,001 K·h — a difference of ~8,800 K·h indicating that long-range order requires greater accumulated thermal energy to attain maximum recovery. Normalized FWHM amplitude ranged from 8.24 (ExtRot 4) to 13.20 (ν_3), confirming differentiated sensitivity to thermal treatment. Comparison between ExtRot and SiO_4 group GAM curves revealed confidence interval overlap of only 56%, value below the 80% threshold established as similarity criterion (Piatt, 2022; Schauer & Hedges, 2021).

Table 9. GAM Fit Metrics by Vibrational Band

Band	Observations	Pseudo-R^2	AIC	GCV	EDOF	FWHM Range (z)	E_min (K·h)
ExtRot 4	1.589	0.531	−1,226.8	0.027	7.90	8.24	326.813
$\nu_2(SiO_4)$	1.590	0.549	−1,587.7	0.021	7.90	10.26	318.001
$\nu_1(SiO_4)$	1.458	0.335	831.5	0.103	7.90	10.23	318.001
$\nu_3(SiO_4)$	1.588	0.381	−1,076.4	0.029	7.90	13.20	318.001
Global Model	6.225	0.334	505.7	0.063	7.90	—	—
Interaction Model	6.225	0.366	213.8	0.060	13.52	—	—

Note: GAM = Generalized Additive Model; AIC = Akaike Information Criterion; GCV = Generalized Cross-Validation; EDOF = Effective Degrees of Freedom; FWHM = Full Width at Half Maximum; E_min = minimum energy (product of temperature and time); ExtRot = external rotation.

3.1.2.1.3 Individual Band Analysis and Differential Sensitivity

Individual band analysis decomposition enabled identification of substantial variations in fit properties and annealing response amplitudes, as documented in Table 9 and visualized in Figure 9. GAM residual boxplots by modal group (Figure9a) confirmed that SiO_4 group residual dispersion was slightly superior to ExtRot group, consistent with greater internal mode response variability.

Comparison between additive and interaction models (Figure9b) resulted in ΔAIC = 292.0 points. The magnitude of this difference, substantially exceeding the 10 threshold established as very strong evidence favoring the more complex model according to Burnham and Anderson criteria, indicates probability exceeding 99.99% that the interaction model better represents data structure. Significant interaction between modal group and annealing parameter statistically grounds the conclusion that recovery trajectories differ not only in magnitude but also in qualitative form, with distinct curvature patterns along the annealing gradient.

Individual GAM curves by Raman band (Figure 9c) enabled comparison of differential thermal sensitivities. The $\nu_2(SiO_4)$ band presented the highest individual Pseudo-R^2 (0.549), indicating that this angular deformation mode maintains more deterministic relationship with thermal history. Physical interpretation of this result suggests that bending vibrations are particularly sensitive to angular distortions introduced by point defects and their subsequent elimination during annealing (Shchapova et al., 2020; Lenz et al., 2020), since O-Si-O angle geometry is directly affected by oxygen vacancies and silicon displacements. In contrast, the $\nu_1(SiO_4)$ band presented the lowest individual Pseudo-R^2 (0.335), suggesting that symmetric stretching is influenced by additional factors not captured by the model, such as local compositional variations or heterogeneity in radiation damage distribution (Nasdala et al., 1995; Zhang et al., 2000).

The heatmap (Figure 9d) presents normalized mean FWHM two-dimensional distribution as a function of vibrational band and annealing parameter bins, using color scale (red = high disorder, blue = low disorder). This visualization enables identification of high and low structural disorder regions along the annealing gradient. SiO_4 bands (ν_1, ν_2, ν_3) exhibited similar recovery patterns among themselves, with chromatic transition from red to blue at intermediate energies, while ExtRot 4 demonstrated distinct trajectory with earlier transition. The $\nu_3(SiO_4)$ band presented the highest variation amplitude (13.20 units), evidenced by greater chromatic gradient extension, confirming its elevated sensitivity to structural changes. The ExtRot 4 band presented the lowest amplitude (8.24 units), consistent with lower susceptibility of external rotation modes to structural perturbations (Dawson et al., 1971; Härtel et al., 2022). The intragroup heterogeneity observed in the heatmap justifies individual band analysis over modal group aggregations.

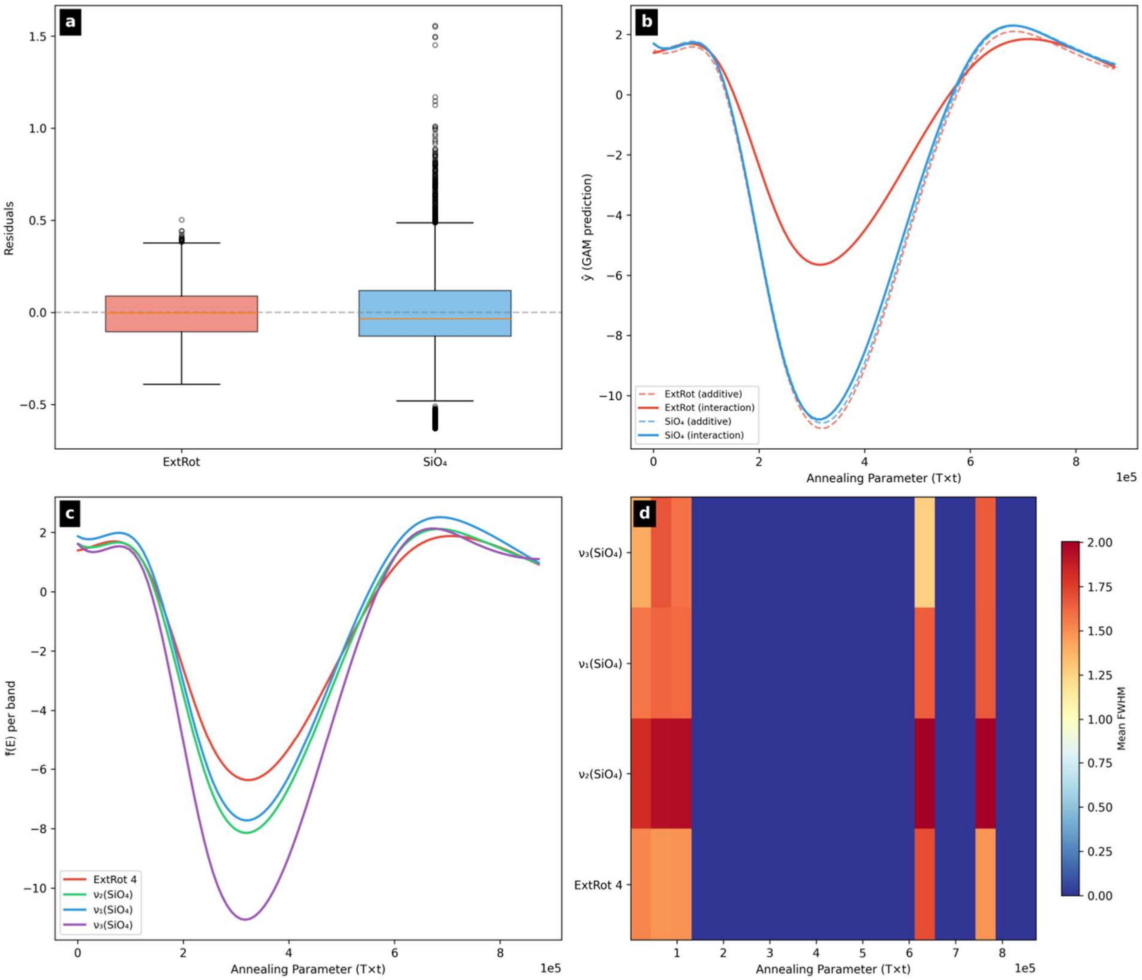

Figure 9 - Extended GAM analysis for individual vibrational bands. GAM Next Steps Analysis for Hypothesis H1.(a) Residual Distribution - Boxplot of GAM residuals by modal group. Outliers: ExtRot=8.9%, SiO_4=9.2%. (b) Additive vs Interaction Model - Comparison of GAM predictions with and without group×energy interaction. ΔAIC=292.0. Better model: interacao. (c) GAM Curves by Individual Band - Fitted spline $\hat{f}(E)$ (i.e.; E= annealing parameter) for each Raman band (ExtRot 4, ν_1, ν_2, ν_3 SiO_4). (d) FWHM Heatmap - Mean normalized FWHM across thermal energy bins for each band. Color scale: RdYlBu_r. Model: pyGAMLinearGAM with 10 splines of order 3.

3.1.2.2. Critical Temperatures and Inflection Points in Recovery (Hypothesis H2)

3.1.2.2.1 Breakpoint Detection via Segmented Regression

Hypothesis H2 investigation concentrated on identifying temperatures where qualitative changes occur in normalized FWHM recovery rate, theoretically corresponding to transitions between recovery stages proposed by Geisler and collaborators (Table 10). Segmented regression employed global optimization via Differential Evolution to minimize residual sum of squares of the two-breakpoint model, followed by model comparison via Akaike information criterion and cross-validation with literature values.

Segmented regression analysis by band (Figure 10) identified two statistically significant breakpoints. These breakpoints delimit three distinct recovery regimes: the first breakpoint at 607.0 K marks transition between point defect mobility-dominated regime (Stage I) and domain reorganization regime (Stage II), while the second breakpoint at 839.6 K delimits beginning of partial recrystallization characteristic of Stage III (Geisler, 2002; Härtel et al., 2021; Fan et al., 2024). Threshold values were determined applying consensus criterion that adopts empirical values when discrepancy with literature exceeds 100 K, as occurred for the II→III transition.

Individual band analysis revealed that $\nu_2(SiO_4)$ and $\nu_3(SiO_4)$ bands presented statistically significant segmentation with $p < 0.05$ and $\Delta AIC > 2$, while ExtRot 4 and $\nu_1(SiO_4)$ did not attain conventional significance. Individual breakpoints for ν_2 (Figure10c) were located at 676.6 K and 843.1 K, while for ν_3 (Figure10d) they were identified at 594.5 K and 725.9 K. This inter-band variability is consistent with interpretation that different vibrational modes are sensitive to distinct aspects of crystalline structure, each with its own characteristic activation energy. Stretching modes (ν_2, ν_3) demonstrated greater stage transition sensitivity than external rotation modes (ExtRot) (Figure10a) and symmetric stretching mode (ν_1) (Figure10b), possibly because changes in tetrahedral geometry are more directly affected by domain reorganization and recrystallization processes.

Empirical breakpoints obtained in this study (607 K and 840 K) are systematically lower than Geisler's (2002) reference values (673 K and 973 K), by 66 K and 133 K respectively. The most likely source of this offset lies in the use of the single annealing parameter $T \times t$ as a proxy for the full Arrhenius kinetic parameter $t \cdot \exp(-Ea/RT)$. The parameter $T \times t$ emerges as a first-order approximation of the Arrhenius integral, valid only when the energy of activation can be treated as constant across the temperature interval of interest The full derivation of the $T \times t$ approximation from the Arrhenius equation is provided in Appendix 3. The three recovery stages, however, involve distinct activation energies (2–3 eV for Stage I, 3–4 eV for Stage II, and 6–8 eV for Stage III), so the Time-Equivalent Principle (PET) is violated across stage boundaries. Collapsing time and temperature into $T \times t$ therefore introduces a systematic bias in the apparent transition temperatures when segments of the recovery trajectory are governed by different rate-limiting processes. This interpretation is consistent with the experimental design: although D-optimality provides efficient global parameter estimation, it does not supply the dense thermal sampling needed to resolve precise stage boundaries. The breakpoints reported here should thus be regarded as central estimates of broad thermal domains rather than exact closure temperatures. Despite the quantitative offset, the three-stage structure originally proposed by Geisler remains clearly validated by the data.

Independent calorimetric studies using DSC (Pidgeon et al., 2017) identified exothermic thermal events at similar temperatures, corroborating stage transition existence during annealing.

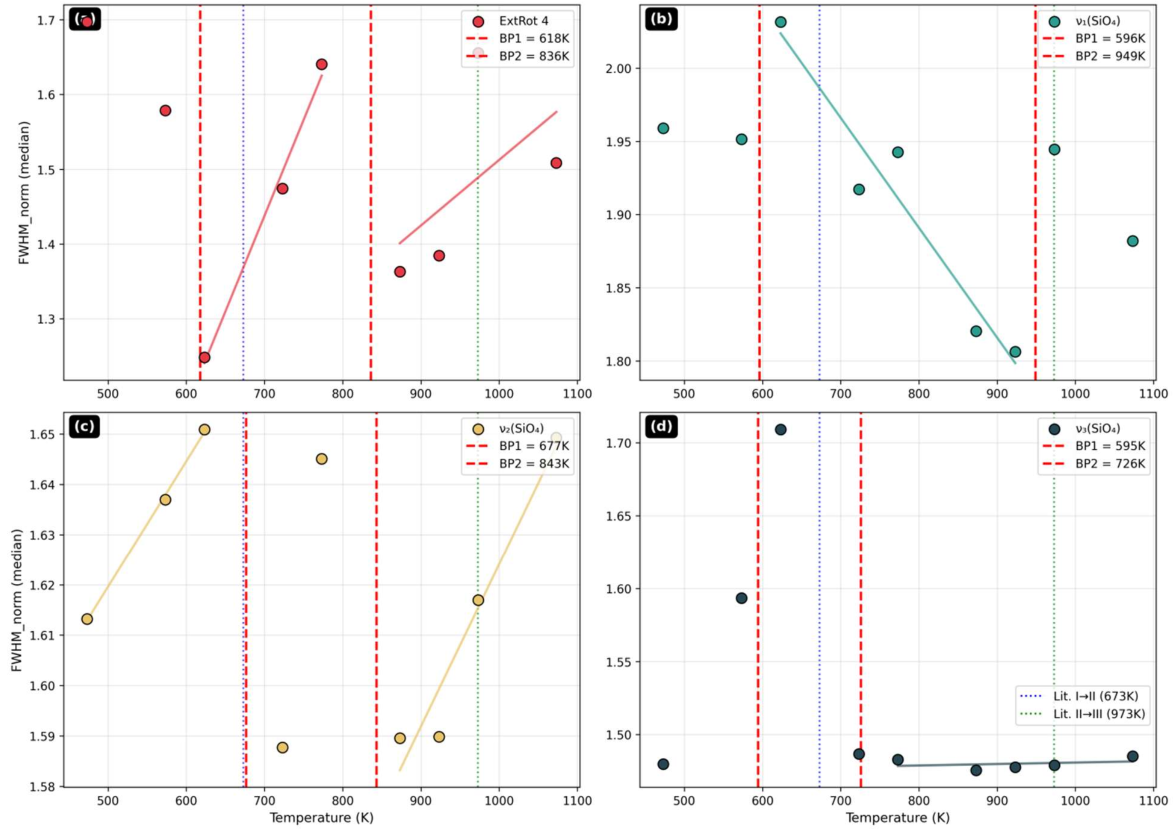

Figure 10 - Segmented regression breakpoint analysis. Segmented Regression Breakpoint Analysis for Hypothesis H2.Segmented regression of median normalized FWHM vs temperature. Empirical breakpoints shown as dashed lines; literature thresholds (Geisler, 2002) as dotted lines. Background shading indicates recovery stages. (a) ExtRot 4. (b) $\nu_1(SiO_4)$. (c) $\nu_2(SiO_4)$ — best fit ($p < 0.05$). (d) $\nu_3(SiO_4)$. Method: Segmented regression with Differential Evolution global optimization. Stages: I (point defect mobility, Ea = 2–3 eV), II (domain reorganization, Ea = 3–4 eV), III (partial recrystallization, Ea = 6–8 eV).

3.1.2.2.2 Derivative Analysis and Maximum Recovery Temperature Identification

Normalized FWHM derivative analysis with respect to temperature enabled precise identification of inflection points in recovery curves, revealing the temperature where each vibrational mode presents maximum band width decrease rate. Spline fits presented R^2 ranging from 0.9888 (ν_2) to 0.9976 (ExtRot 4), as documented in the fit quality table, and all detected extremes were classified as internal (reliable), without boundary artifacts at data range limits.

FWHM versus temperature curve derivatives (Figure 11) enabled inflection point identification by band. For ExtRot 4 (Figure11a), the first derivative presented two internal minima at 575.4 K and 839.9 K, both classified as internal and reliable. The first minimum at 575.4 K, situated in Geisler's Stage I, corresponds to maximum recovery rate temperature for the external rotation mode, indicating that long-range order restoration is most efficient at temperatures where vacancies and interstitials present sufficient diffusivity for migration and recombination (Nasdala et al., 2001; Banerjee et al., 2025), but before higher-energy processes are activated. The second minimum at 839.9 K, situated at Stage II-III boundary, indicates transition to partial recrystallization regime. The two ExtRot 4 derivative maxima at 711.2 K and 964.9 K correspond to secondary inflection points indicating recovery direction changes.

For $\nu_1(SiO_4)$ (Figure 11b), the first derivative presented two minima at 677.6 K and 836.3 K, both in Stage II, and three maxima at 571.7 K, 749.7 K, and 964.9 K. The principal minimum at 677.6 K is situated approximately 100 K above ExtRot 4 minimum, indicating that tetrahedral geometry requires higher temperatures for effective restoration. The more complex extreme pattern, with three maxima versus two in ExtRot band, suggests that symmetric stretching modes respond to additional stage transitions not captured by the simplified three-stage model.

For $\nu_2(SiO_4)$ (Figure 11c), the first derivative presented minima at 661.9 K and 841.1 K, with principal minimum at 661.9 K situated in Stage II. The maxima pattern (554.9 K, 749.7 K, 977.0 K) indicates additional complexity similar to that observed in ν_1. For $\nu_3(SiO_4)$ (Figure11d), the first derivative presented the simplest pattern, with only one minimum at 683.6 K (Stage II) and one maximum at 563.3 K (Stage I). This relative simplicity may reflect greater response homogeneity of the asymmetric stretching mode, which demonstrated the highest individual Pseudo-R^2 among SiO_4 bands.

The 95% confidence intervals for maximum recovery temperatures, estimated via bootstrap with 100% success in all bands, presented considerable widths (350–600 K). This uncertainty reflects not only the limited number of experimental temperature points ($n = 9$) but also the inherent variability in the derivative shapes across vibrational modes, which amplifies the bootstrap variance. These estimates are therefore best interpreted as indicative thermal domains rather than precise closure temperatures.

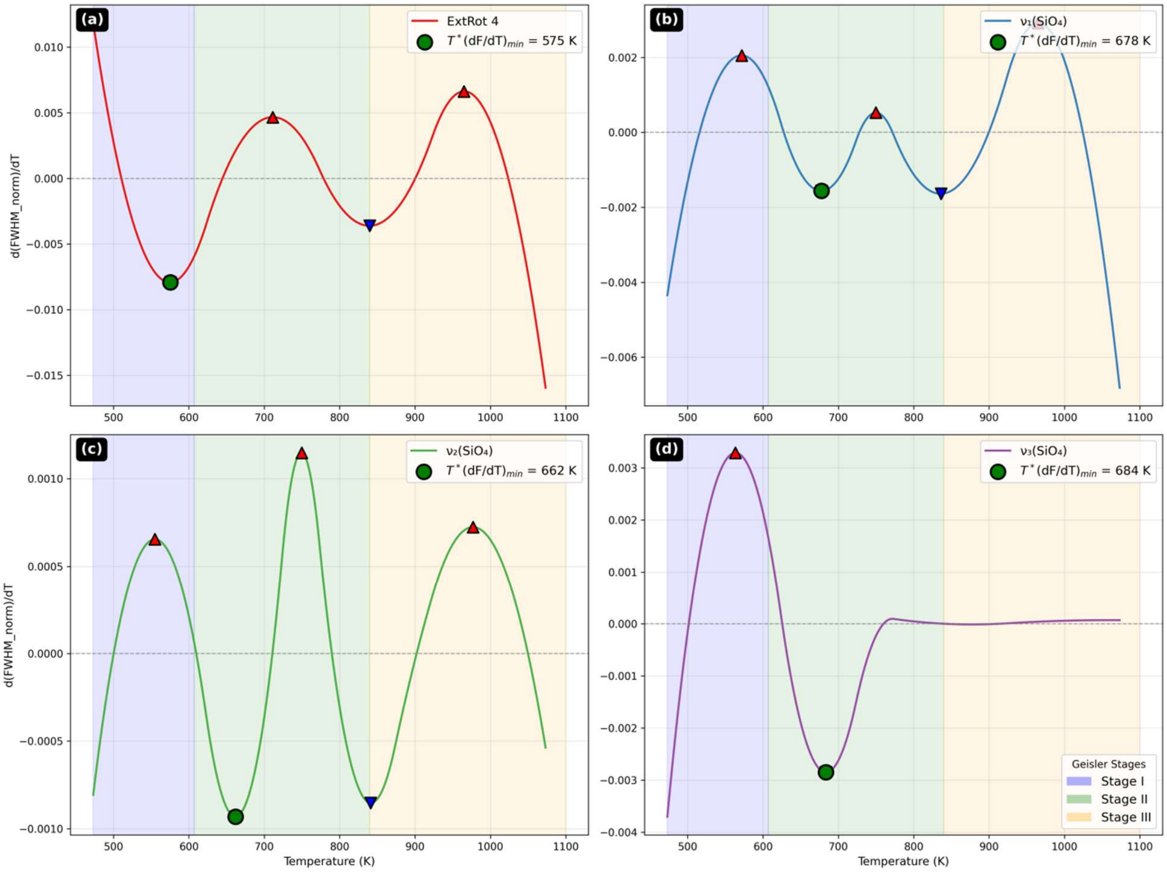

Figure 11 - Derivative analysis of FWHM recovery curves. Derivative Analysis of FWHM Recovery Curves for Hypothesis H2.First derivative d(FWHM_norm)/dT of spline-fitted recovery curves. Principal T* corresponds to the first internal minimum (maximum recovery rate). Background shading indicates Geisler recovery stages. (a) ExtRot 4. (b) $\nu_1(SiO_4)$. (c) $\nu_2(SiO_4)$. (d) $\nu_3(SiO_4)$. Method: Cubic spline interpolation with adaptive smoothing. Local extrema detected via prominence threshold (5% of derivative amplitude).

3.1.2.2.3 H2 Results Consolidation

Inflection point distribution is consistent with activation energy characteristics of each stage in Geisler's model (Table 10). Variance heterogeneity between bands, documented in Table 11, demonstrates that the coefficient of variation (CV) evolves distinctly across stages: in Stages I and II, ExtRot 4 presents higher CV than SiO_4 bands (ratios of 1.56 and 1.48), while in Stage III inversion occurs (ratio 0.92), indicating that partial recrystallization affects internal mode variability more intensely. ExtRot 4 derivative minimum positioning in Stage I indicates that long-range order recovery is dominated by point defect mobility processes, where oxygen vacancies and zirconium interstitials present sufficient diffusivity for migration and recombination at relatively low temperatures (Bjerga et al., 2022). The 2–3 eV activation energy characteristic of this stage is consistent with values reported for point defect diffusion in zircon (Ginster et al., 2019).

In contrast, internal SiO_4 modes, with inflection points in Stage II, respond preferentially to domain reorganization processes requiring higher temperatures for activation. The 3–4 eV activation energy of this stage corresponds to processes involving cooperative rearrangements of multiple atoms (Ginster et al., 2019), necessary for restoring local tetrahedral geometry. The maximum recovery temperature hierarchy (T_maxExtRot<T_max SiO_4, with $\Delta \approx 100$ K) constitutes direct evidence of temporal differentiation between long-range order and local order recovery mechanisms.

Secondary minima detection in all band derivatives around 840 K suggests occurrence of additional transition associated with Stage III onset, where partial recrystallization processes with 6–8 eV activation energy (Geisler, 2002) begin to dominate recovery kinetics. Agreement between empirical breakpoints (607 K, 840 K) and derivative secondary minima confirms stage transition identification.

Table 10. Geisler Recovery Stage Breakpoints

Stage	**Thermal Range (K)**	**Thermal Range (°C)**	**Dominant Physical Process**	**Ea (eV)**	**T_maxExtRot (K)**	**T_maxSiO_4 (K)**
I	473–607	200–334	Point defect mobility	2–3	575.4	-
II	607–840	334–567	Domain reorganization	3–4	-	662–684
III	840–1273	567–1000	Partial recrystallization	6–8	-	-

Note: The empirical breakpoints identified were BP_1 = 607.0 K ($\Delta = -66$ K relative to literature) and BP_2 = 839.6 K ($\Delta = -133$ K relative to literature). Ea values based on Ginster et al. (2019) and Geisler (2002).

Table 11. Coefficients of Variation by Geisler Stage

Stage	**CV ExtRot 4 (%)**	**CV ν_1 (%)**	**CV ν_2 (%)**	**CV ν_3 (%)**	**CV SiO_4 average (%)**	**CV Ratio ExtRot/SiO_4**
I	12.90	12.79	2.82	9.18	8.27	1.56
II	13.46	14.15	3.64	9.58	9.12	1.48
III	18.12	25.27	17.46	16.43	19.72	0.92

Note: Levene's test presented W statistics (non-parametric test statistic for variance homogeneity) ranging from 55.79 to 119.15, with $p < 0.001$ in all stages, confirming significant variance heterogeneity.

3.1.2.3 Vibrational Coupling and Mechanism Differentiation (Hypothesis H4)

3.1.2.3.1 Coupling Hypothesis Formulation and Testing

Refined Hypothesis H4 assessment investigated whether the $\nu_2(SiO_4)$ angular deformation vibrational mode presents preferential coupling with ExtRot 4 external rotation mode compared to ν_3 stretching mode. This hypothesis was motivated by consideration that both modes (ν_2 and ExtRot 4) involve angular deformations, though at distinct spatial scales: ν_2 corresponds to O-Si-O bond angle variation within the SiO_4 tetrahedron, while ExtRot 4 involves tetrahedron rotation as rigid unit relative to neighboring tetrahedra in the crystalline lattice. The underlying theoretical premise proposed that if tetrahedron internal geometry is affected by its spatial orientation in the damaged lattice, then thermal recovery should coordinately restore both modes, resulting in preferential ν_2-ExtRot coupling.

The statistical procedure employed Paired Bootstrap methodology with 10,000 resamples, applied to 1,489 valid observations after spectral quality filtering (peak fit $R^2 \geq 0.95$ and signal-to-noise ratio ≥ 3). Empirical Geisler thresholds ($BP_1 = 607.0$ K; $BP_2 = 839.6$ K) were used for recovery stage stratification. Premise verification via Mardia's bivariate normality test revealed significant normality assumption violation in both variable pairs (multivariate skewness $\chi^2 = 1,207.59$ for ν_2-ExtRot and 1,730.72 for ν_2-ν_3, both with $p < 0.0001$), justifying non-parametric bootstrap approach adoption.

Figure 12 presents stratified analysis of refined H4 test via paired bootstrap (10,000 resamples, n = 1,489), investigating whether vibrational modes of distinct nature (internal-external) present superior coupling to modes of same nature (internal-internal).

The dot diagram (Figure12a) compares r(ν_2, ExtRot 4) and r(ν_2, ν_3) for each Geisler stage. In Stage I (n=215, 473–607 K), both correlations are weak: −0.170 for ExtRot 4 and 0.138 for ν_3, indicating modes respond almost independently during initial point defect recovery. In Stage II (n=369, 607–840 K), the pattern persists with −0.094 and 0.219, respectively. The dramatic transition occurs in Stage III (n=905, 840–1273 K), where both correlations become strongly positive: 0.780 and 0.854. Dashed vertical lines indicate global values (ExtRot 4 = 0.662, ν_3 = 0.787), demonstrating that ν_2-ν_3 correlation consistently exceeds ν_2-ExtRot 4 across all stages.

The two-dimensional space (Figure 12b) presents r(ν_2, ExtRot 4) versus r(ν_2, ν_3). The dashed diagonal ($r_1 = r_2$) divides the plane into two regions: H_1 (shaded, below diagonal) where ExtRot 4 would have superior coupling, and H_0 (above) where ν_3 prevails. Points represent Stage I, II, III, and Global result "G". Point trajectory reveals thermal evolution of coupling: in initial stages (I, II), points are situated in lower-left quadrant, reflecting weak or negative correlations with ExtRot 4. During recrystallization (III), the point migrates to upper-right quadrant, approaching the diagonal but remaining in H_0 region. This convergence indicates that although coupling between all modes increases with crystalline recovery, internal SiO_4 modes maintain preferential correlation among themselves.

The 95% bootstrap confidence intervals for $\Delta r = r(\nu_2, \text{ExtRot } 4) - r(\nu_2, \nu_3)$ (Fig.6c) are presented by stage. Stage I: $\Delta r = -0.308$ ($p = 0.964$); Stage II: $\Delta r = -0.313$ ($p = 1.000$); Stage III: $\Delta r = -0.073$ ($p = 1.000$). The dashed red line represents H_0 ($\Delta r = 0$); the purple line indicates global $\Delta r = -0.125$. Notably, Stages I and II present similar differences (~−0.31), while Stage III shows substantial reduction (−0.073), suggesting that recrystallization promotes correlation convergence without inverting hierarchy. The p-values ≥ 0.964 in all stages indicate robust H_1 rejection.

Violin plots (Figure12d) reveal Δr distribution structure by stage. Stage I presents highest dispersion (variance ~0.04), reflecting heterogeneity in vibrational responses during initial annealing phase. Stage II shows more concentrated distribution. Stage III displays narrow distribution centered near zero, indicating more homogeneous behavior during recrystallization. The red star marks observed Δr in each stage. Crucially, no distribution crosses the H_0 line ($\Delta r = 0$), confirming that even considering sampling uncertainty, ν_2-ν_3 correlation remains superior under all conditions.

Effect direction consistency ($\Delta r < 0$ in all stages) and statistical decision (alternative hypothesis rejected in all cases) grounds the conclusion: internal SiO_4 modes (ν_2, ν_3) maintain preferential coupling throughout the entire thermal recovery process, rejecting H_1.

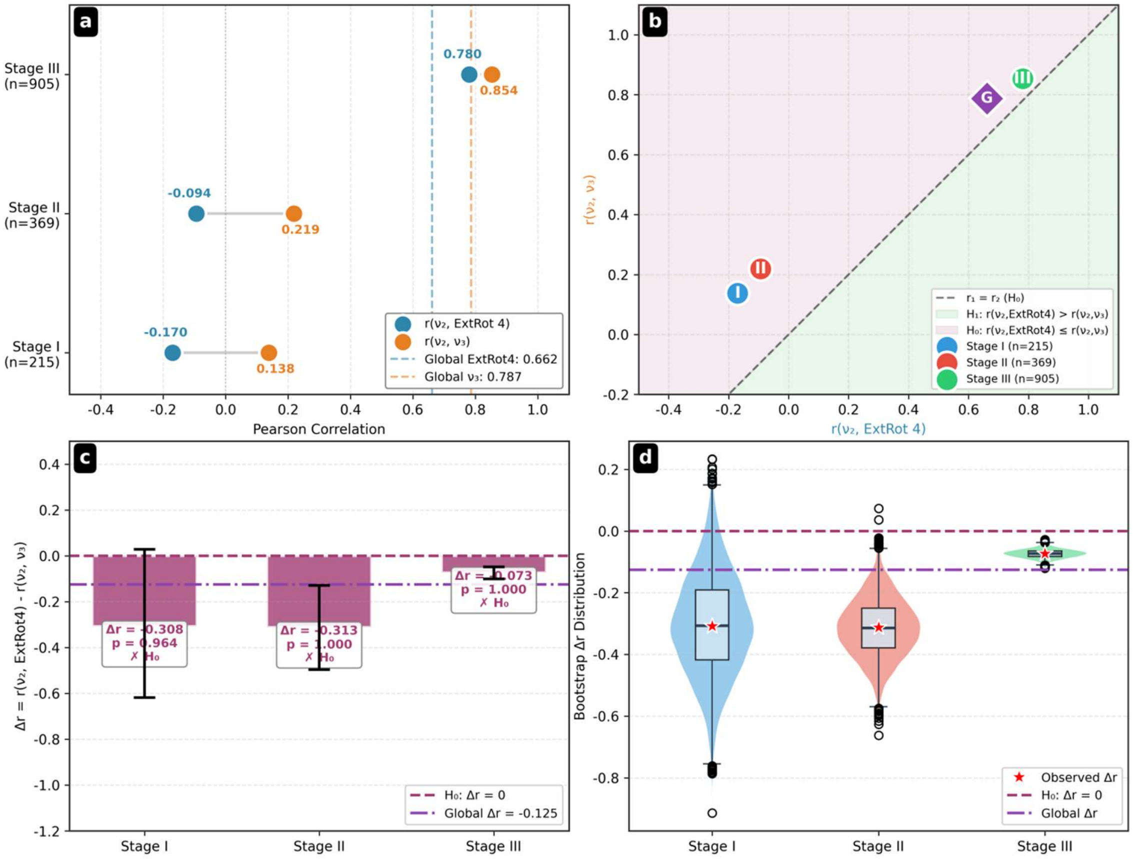

Figure 12 - Correlation analysis by Geisler stage for coupling hypothesis. Correlation Analysis by Geisler Stage for Hypothesis H4.Comparison of Pearson correlations r(ν_2, ExtRot 4) vs r(ν_2, ν_3) stratified by Geisler recovery stages. H_1: r(ν_2, ExtRot 4) > r(ν_2, ν_3) indicates stronger coupling between internal $\nu_2(SiO_4)$ and external rotation modes. (a) Dumbbell plot of correlations by stage with global reference lines. (b) Scatter plot of correlation pairs; diagonal represents H_0 ($r_1 = r_2$); shaded regions indicate H_1 and H_0 zones. (c) Δr = r(ν_2, ExtRot 4) − r(ν_2, ν_3) per stage with 95% CI error bars; bars indicate H_1 confirmation. (d) Bootstrap distributions of Δr by stage with observed values marked. Method: Permutation bootstrap (n = 5000 resamples). Significance assessed via one-tailed p-value (α = 0.05).

3.1.2.3.2 Non-Coupling Results and Interpretation

The correlation between ν_2 and ExtRot 4 (r = 0.662) was inferior to correlation between ν_2 and ν_3 (r = 0.787), resulting in difference Δr = −0.125. The 95% bootstrap confidence interval for this difference was entirely negative ([−0.154; −0.099]), and the one-sided p-value attained 1.0, indicating that the alternative hypothesis of preferential coupling with ExtRot finds no support in observed data. The difference magnitude (−0.125) is substantial in practical terms, corresponding to approximately 16% of ν_2–ν_3 correlation magnitude.

Stratified analysis revealed consistent non-coupling pattern across all stages. In Stage I, $\Delta r = -0.308$ with $p = 0.96$ indicated robust preference for ν_2-ν_3 coupling, even in the low-temperature regime where point defect mobility predominates. In Stage II, $\Delta r = -0.313$ with $p = 1.00$ confirmed the pattern even more robustly, demonstrating that domain reorganization affects tetrahedral internal modes in correlated fashion but independent of external modes. In Stage III, the difference reduced to $\Delta r = -0.073$ with $p = 1.00$, indicating gradual correlation pattern convergence as structure approaches ordered state during partial recrystallization.

The decreasing $|\Delta r|$ magnitude from Stage I to Stage III (from 0.31 to 0.07) suggests that differentiation between recovery mechanisms progressively diminishes with structural restoration. This behavior is physically plausible: as the crystalline lattice recovers its periodicity and SiO_4 tetrahedra return to ideal geometry, correlations among all vibrational modes tend to converge to perfect crystal characteristic values (Nasdala et al., 2001; Härtel et al., 2022), where recovery mechanism distinctions become irrelevant.

The non-confirmation result of preferential ν_2-ExtRot coupling hypothesis indicates that vibrational movement symmetry does not determine correlations during structural recovery. Although ν_2 and ExtRot 4 share angular character, they respond to structural perturbations at fundamentally distinct spatial scales: ν_2 is sensitive to SiO_4 tetrahedron internal distortions, while ExtRot 4 responds to orientational correlation loss between neighboring coordination polyhedra. The preferential correlation observed between ν_2 and ν_3 is consistent with group theory for the zircon lattice, which predicts that modes belonging to the same local symmetry group should exhibit correlated vibrational behavior, regardless of the specific atomic movement type involved.

3.1.2.4 Non-Monotonic Intensity Ratio Behavior (Hypothesis H5)

3.1.2.4.1 GAM Analysis of ExtRot/ν_3 Ratio

Hypothesis H5 investigation examined area ratio behavior between external ExtRot 4 mode and internal ν_3 mode across the annealing temperature range. This ratio was proposed as indicator of temporal differentiation between long-range order and local order recovery processes, with initial expectation of monotonically increasing behavior if long-range order systematically recovered before local order.

Figure 13 presented the fitted ExtRot/ν_3 ratio curve versus temperature with 95% confidence interval (Figure 13a). The first derivative (Figure13b) revealed ratio increase and decrease regions with temperature. Residuals (Figure 13c) demonstrated random dispersion around zero. Comparison with linear regression (Figure 13d) indicated non-linear approach superiority.

The GAM model presented explanatory capacity superior to linear model, with Pseudo-$R^2 = 0.256$ versus $R^2 = 0.026$, representing approximately 873% improvement in explained variance. The GCV score of 0.247 and AIC of 2,162.4 indicate model adequacy to data. GAM model derivative analysis revealed fundamentally non-monotonic behavior, with ExtRot/ν_3 ratio attaining maximum value of 1.445 at temperature of 622.4 K.

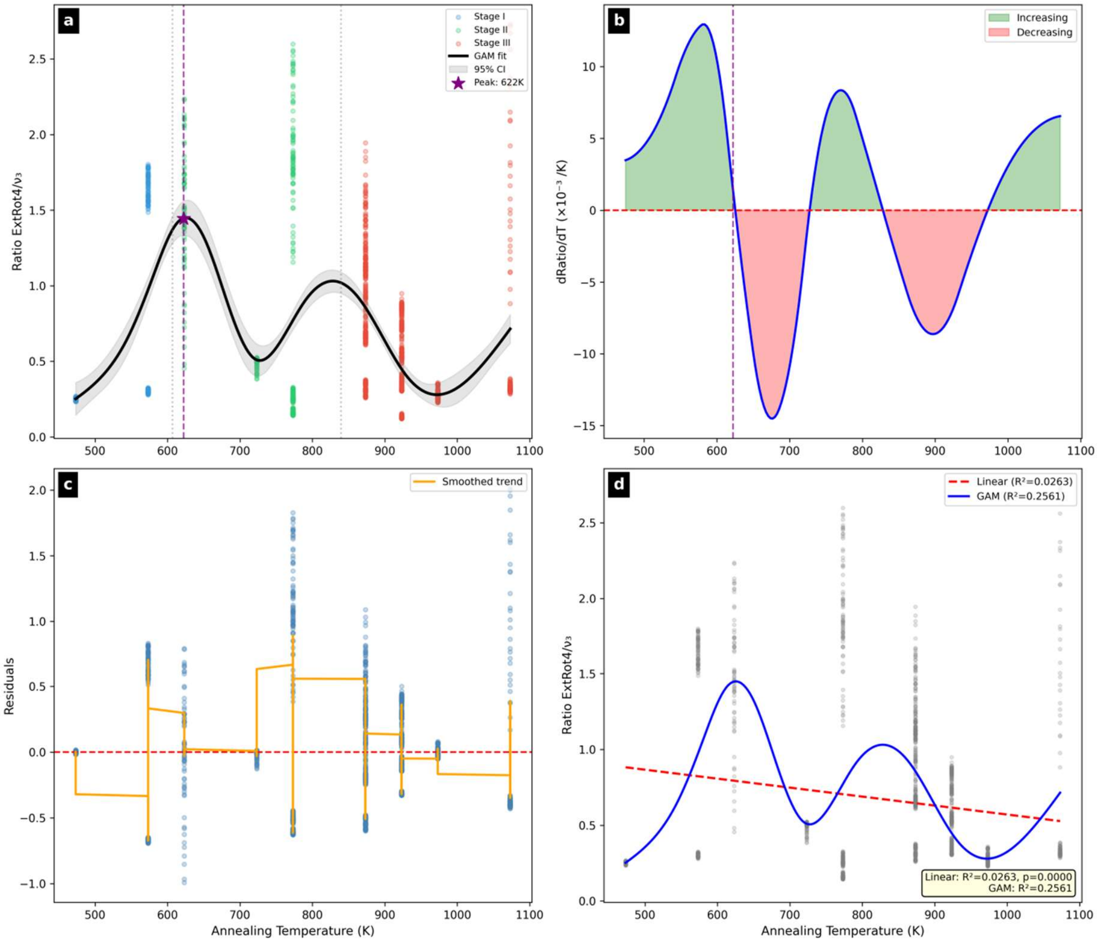

Figure 13 - GAM non-linear analysis of ExtRot/ν_3 ratio. H5 GAM Non-Linear Analysis. (a) GAM Fit with Confidence Interval - Generalized Additive Model fit (black line) with 95% confidence band (gray). Data points colored by Geisler stage. Peak detected at T = 622 K (purple star). (b) First Derivative of GAM - Rate of change of ratio with temperature. Green regions indicate increasing trend, red regions indicate decreasing trend. Zero crossing marks transition point. (c) GAM Residuals- Residuals vs temperature with smoothed trend (orange). Random scatter around zero indicates good fit. (d) Linear vs GAM Comparison - Red dashed: linear regression ($R^2 = 0.0263$). Blue: GAM fit ($R^2 = 0.2561$). GAM captures non-linear

pattern missed by linear model. GAM significantly improves fit over linear model, with peak ratio at ~622 K corresponding to Stage II (Geisler).

3.1.2.4.2 Thermal Peak Identification and Interpretation

The identified peak temperature (622.4 K) is situated precisely in Geisler's Stage II (607–840 K), characterized by crystalline domain reorganization with 3–4 eV activation energy. This location suggests that maximum differentiation between external and internal mode recovery rates occurs during intermediate annealing regime, when domain reorganization processes begin to dominate recovery kinetics.

The ratio increase region extended from 475 K to 622 K, with maximum increase rate of 0.0129 K^{-1}, indicating that in this temperature range long-range order recovery systematically surpasses local order recovery. Physical interpretation of this behavior involves Stage I predominant processes: point defect mobility preferentially affects lattice translational periodicity, which is detected by external rotation modes, resulting in faster ExtRot 4 FWHM narrowing relative to ν_3 FWHM. Local order recovery (Härtel et al., 2021; Fan et al., 2023) requires higher temperatures.

The decrease region occurred from 625 K to 969 K, with maximum decrease rate of −0.0145 K^{-1}, demonstrating that at higher temperatures ν_3 mode recovery accelerates and surpasses ExtRot 4 mode recovery. Physical interpretation of this second phase involves Stage II and III predominant processes: domain reorganization and partial recrystallization are more efficient in restoring local tetrahedral geometry, which is detected by internal stretching modes, resulting in accelerated ν_3 mode recovery.

The GAM versus linear comparison p-value (0.18) did not attain statistical significance at $\alpha = 0.05$ level, justifying hypothesis classification as partially confirmed. However, the fit improvement magnitude (Pseudo-$R^2 = 0.256$ versus $R^2 = 0.026$) and observed pattern physical consistency suggest that non-monotonic behavior represents genuine recovery dynamics characteristic, whose statistical confirmation would require increased sample power in transition regions.

3.1.2.5 Recovery Heterogeneity by Stage (Hypothesis H6)

3.1.2.5.1 Stratified Coefficient of Variation Analysis

Stage stratification employed empirically determined Geisler thresholds (Section 3.1.2.2) rather than fixed literature values, ensuring consistency with the thermal regime boundaries identified from experimental data.

Hypothesis H6 assessment investigated whether external vibrational modes present greater recovery heterogeneity (variability) compared to internal modes during thermal treatment. Levene's test results revealed statistically significant variance heterogeneity in all three analyzed stages, with Kruskal-Wallis W statistics (non-parametric ANOVA test statistic) ranging from 55.79 (Stage I) to 119.15 (Stage II) and p-values below 10^{-32}, confirming that normalized FWHM dispersion systematically differs among vibrational modes across all investigated temperature ranges.

Stage-stratified empirical cumulative distribution functions (Figure 14) revealed compact distributions in Stage I with visible band separation (Figure14a), similar pattern in Stage II with slight dispersion increase (Figure14b), and substantial dispersion increase in Stage III especially for $\nu_1(SiO_4)$ (Figure 14c). Consolidated overlay (Figure14d) enabled distributional evolution comparison along the thermal gradient.

ECDF analysis revealed that Stage III curves systematically shift leftward (lower mean FWHM values), indicating greater sample crystallinity after high-temperature thermal treatments. Simultaneously, Stage III curves present less steep slope, reflecting greater measurement variability in this stage. Separation between ExtRot and SiO_4 ECDFs is particularly pronounced in Stages I and II, graphically visualizing normalized FWHM distribution difference grounding hypothesis confirmation in these initial stages.

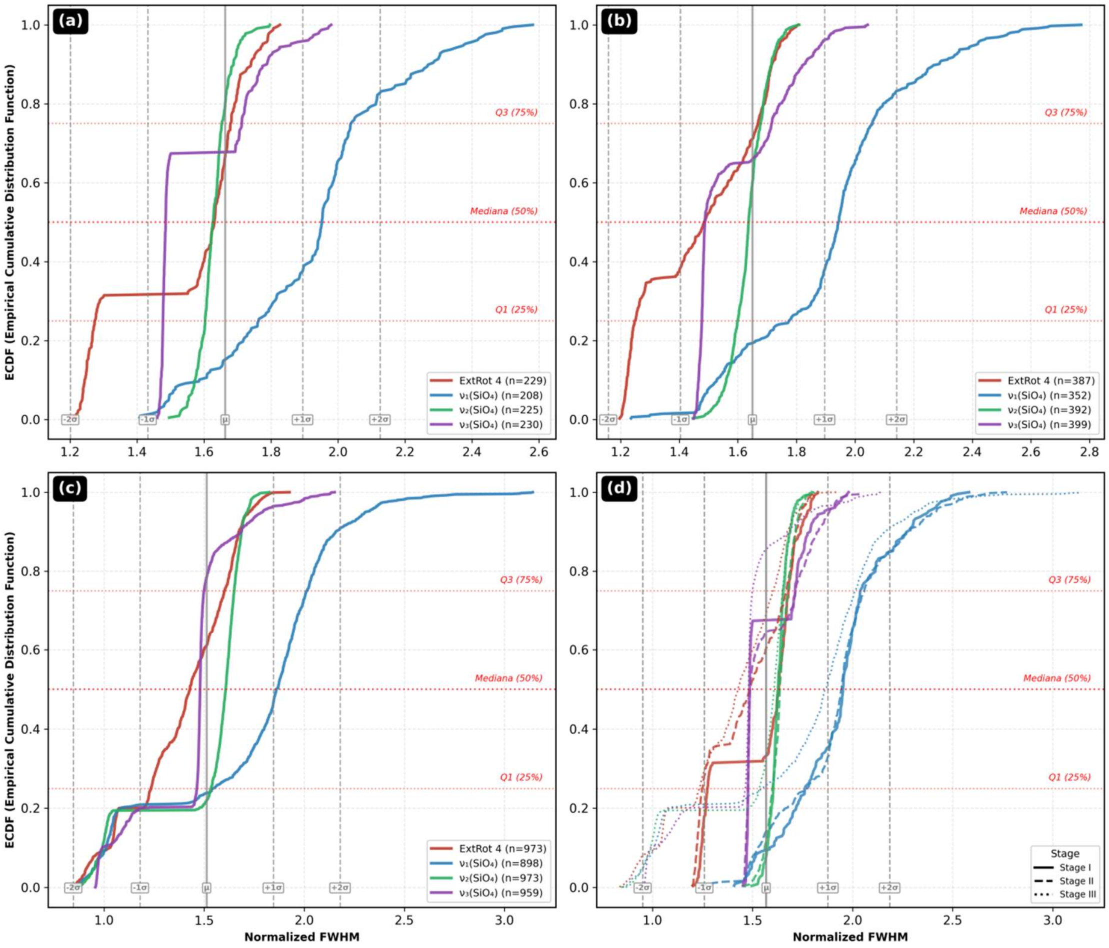

Figure 14 - ECDF analysis of normalized FWHM by Geisler stage. ECDF Dashboard of Normalized FWHM by Geisler Stage for Hypothesis H6.Empirical cumulative distribution functions (ECDF) of normalized FWHM for each Raman band, stratified by Geisler recovery stage. Horizontal reference lines indicate quartiles (Q1, Median, Q3). Panel (d) consolidates all stages with line style differentiation. (a) Stage I. (b) Stage II. (c) Stage III. (d) Consolidated comparison across stages. Steeper ECDF curves indicate lower dispersion; rightward shifts indicate higher mean FWHM values. Separation between band curves reflects differential recovery kinetics.

3.1.2.5.2 Results by Geisler Stage

In Stage I (473–607 K), the ExtRot 4 mode coefficient of variation was 12.90%, while mean SiO_4 modes CV was 8.27%, resulting in ratio of 1.56. This greater external mode heterogeneity in low-temperature regime indicates that long-range order is more sensitive to structural defect density and distribution variations. Physical interpretation suggests that small differences in point defect concentration produce proportionally greater variations in translational periodicity than in local tetrahedron geometry, since long-range order results from correlation among atomic positions in multiple unit cells, amplifying local perturbation effects (Ewing et al., 2003).

In Stage II (607–840 K), values were 13.46% (ExtRot) versus 9.12% (mean SiO_4), with ratio of 1.48. The observed pattern was similar to Stage I, with ExtRot presenting more dispersed distribution, though with slight convergence indicated by CV ratio reduction. Differentiated heterogeneity persistence in this stage suggests that domain reorganization processes also preferentially affect long-range order, possibly because correlated orientation restoration between neighboring tetrahedra requires coordinated defect elimination varying in concentration among different sample regions.

3.1.2.5.3 Pattern Inversion in Stage III

Contrary to initial stages, Stage III (840–1273 K) presented heterogeneity pattern inversion. ExtRot 4 mode CV was 18.12%, while mean SiO_4 modes was 19.72%, resulting in ratio of 0.92. This inversion indicates that during partial recrystallization characteristic of Stage III with 6–8 eV activation energy, internal SiO_4 modes present greater response variability than external modes.

Physical interpretation of this inversion involves recrystallization heterogeneous nature: crystalline domain nucleation occurs preferentially at sites with local defect concentration (Capitani et al., 2000; Geisler et al., 2001), resulting in bimodal crystallinity degree distribution (Nasdala et al., 2002; Ribeiro et al., 2025). This structural heterogeneity affects local tetrahedral geometry (Ewing et al., 2003) (detected by internal modes) more intensely than average long-range order (detected by external modes), since internal modes directly respond to local SiO_4 tetrahedron distortion variations, while external modes integrate contributions from multiple domains with different restoration degrees.

CV absolute value evolution from Stage I to Stage III demonstrated progressive heterogeneity increase in all bands (CV evolution table). The most pronounced increase was observed in $\nu_2(SiO_4)$ band, which presented 519% CV growth between extreme stages (from 2.82% to 17.46%), indicating that angular deformation mode is particularly susceptible to structural heterogeneities emerging during partial recrystallization. This differentiated sensitivity can be exploited as diagnostic recovery stage indicator in thermochronology applications.

3.1.2.6 Integrated Discussion

3.1.2.6.1 Principal Evidence Consolidation

Integrated analysis of six investigated hypothesis results enables establishment of a comprehensive framework for crystalline recovery dynamics in zircon via Raman spectroscopy. Principal evidence converges to the central conclusion that metamict zircon structural restoration involves differentiated mechanisms operating at multiple spatial and thermal scales, with recovery trajectories that differ qualitatively between external and internal SiO_4 tetrahedral modes.

Before proceeding, it is essential to clarify the role of the Generalized Additive Models employed throughout this work. GAMs are semi-parametric empirical tools designed to capture non-linear relationships without imposing a specific kinetic law. They are not intended to replace classical Arrhenius-based models or physically derived rate equations. Rather, their purpose here is to reveal the shape of recovery trajectories, identify critical thermal thresholds, and provide quantitative constraints that can subsequently inform the development of mechanistic models. This distinction is particularly relevant when comparing the empirical breakpoints reported below with activation energies from the literature.

Statistically significant GAM curve difference between ExtRot and SiO_4 ($\Delta AIC = 292$; Pseudo-$R^2 = 0.334$) grounds the conclusion that external and internal modes do not respond uniformly to thermal annealing, reflecting operation of distinct recovery mechanisms at each spatial scale. Differentiated maximum recovery temperature positioning, with ExtRot 4 attaining inflection at 575 K (Stage I) and SiO_4 modes between 662–684 K (Stage II), indicates that long-range order recovers approximately 100 K before local tetrahedral geometry. This temporal sequence is consistent with Geisler's activation energy hierarchy, where lower-energy processes are activated first and progressively replaced by higher-energy mechanisms as temperature increases.It should be noted, however, that the present spectroscopic and scattering data provide indirect evidence for this mechanistic interpretation. Direct elucidation of the connection between recovery mechanisms at different spatial scales would require complementary imaging techniques, such as transmission electron microscopy, which were beyond the scope of this study.

Non-monotonic behavior detection in ExtRot/ν_3 ratio, with peak at 622 K situated in Stage II, reveals that recovery dynamics involves competition between mechanisms with distinct kinetics, resulting in relative process dominance inversion at intermediate temperature. Preferential coupling between ν_2 and ν_3, to the detriment of ExtRot, with $\Delta r = -0.125$ consistently negative across all stages, indicates that internal tetrahedral modes share restoration mechanisms distinct from processes affecting coordination polyhedra spatial orientation.

3.1.2.6.2 Hypothesis Correlation and Internal Consistency

Systematic comparison of results among hypotheses reveals correlation patterns strengthening individual conclusions and demonstrating internal consistency of the observation set. Curve form difference documented in H1 analysis, with only 56% confidence interval overlap, is coherent with differentiated breakpoints by band identified in H2 analysis, both results pointing to existence of recovery mechanisms with distinct kinetics.

The ExtRot/ν_3 ratio peak temperature (622 K) identified in H5 analysis is situated precisely between BP_1 (607 K) and BP_2 (840 K) breakpoints determined in H2 analysis, demonstrating that recovery mechanism dominance inversion occurs during Stage II characterized by domain reorganization. Heterogeneity inversion documented in H6 analysis, with CV ratio passing from 1.56 (Stage I) to 0.92 (Stage III), occurs precisely in the temperature range where activation energies increase to 6–8 eV, suggesting that partial recrystallization processes differentially affect internal mode variability. Non-coupling between ν_2 and ExtRot demonstrated in H4 analysis is consistent with different recovery forms evidenced in H1 GAM curves, both results indicating that mechanisms operating at tetrahedron scale are distinct from those affecting lattice periodicity.

3.1.2.6.3 Implications for Raman Thermochronology

Results present direct implications for Raman spectroscopy application in low-temperature thermochronology. Non-linear behavior demonstration between spectral parameters and temperature grounds need for non-linear approaches in Raman thermometer calibration (Härtel et al., 2021), a behavior also documented in thermal maturity evaluations of sedimentary organic matter (Kibria et al., 2020), invalidating models assuming linear relationship between band width and thermal history. Transdimensional Bayesian thermal history inversion via MCMC (Gallagher, 2012) offers appropriate methodological framework for incorporating such non-linearities in thermochronological reconstruction. Specific critical temperature identification (575 K, 622 K, 662–684 K) suggests existence of multiple partial closure temperatures for each vibrational mode (Dodson, 1973; Härtel et al., 2021), with implications for thermochronological reconstruction temporal resolution. This behavior is analogous to relationship between metamorphic peak temperatures and cooling trajectories documented in continental collision contexts (Berger et al., 2020).

Stage-observed heterogeneity dependence indicates that uncertainty associated with Raman measurements varies significantly (Härtel et al., 2022) with sample thermal history, requiring differentiated error bar treatment as function of inferred annealing temperature. Greater dispersion in Stage III, especially for internal tetrahedral modes, suggests that Raman thermometry based on SiO_4 bands may present greater uncertainty in samples experiencing elevated annealing temperatures.

Band selection for thermochronological calibration should consider not only individual damage sensitivity but also degree of inter-band coupling. For multi-band thermochronological reconstructions, internal band selection (ν_1, ν_2, ν_3) may offer greater interpretive consistency than internal and external band combination, given the more robust coupling between internal modes observed in the study.

3.1.2.6.4 Literature Consistency and State of the Art

Systematic comparison demonstrated generalized consistency with published zircon spectroscopic literature data. Band annealing sensitivity hierarchy (ν_3 > ν_2 >ExtRot in amplitude, as documented in GAM metrics tables) reproduces Härtel and collaborators' observations (Härtel et al., 2021; Härtel et al., 2022), confirming that stretching modes are more sensitive to structural perturbations than external rotation modes.

Geisler's three-stage model was validated by breakpoint detection at empirically consistent positions (607 K and 840 K), though with systematic deviations relative to reference values that may reflect experimental condition or sample composition differences. Variance convergence observed in Stage III corroborates structural homogenization interpretation during recrystallization, behavior predicted by phenomenological model and consistent with transmission electron microscopy observations in partially recrystallized zircons (Capitani et al., 2000; Vonlanthen et al., 2012). DSC calorimetric measurements (Pidgeon et al., 2017) demonstrated exothermic events associated with structural recovery, providing complementary thermodynamic evidence to spectroscopic data.

3.1.2.6.5 Methodological Limitations

Identified methodological limitations must be considered in result interpretation and future investigation planning. Moderate GAM Pseudo-R^2 (0.334) for H1 indicates that approximately two-thirds of data variability is not explained by relationship with annealing parameter, suggesting influence of additional factors such as compositional variations, radiation damage distribution heterogeneity, or measurement errors (Nasdala et al., 2001) not captured by the model.

Observation concentration in Stage III (905 of 1,489 for H4) introduces greater uncertainty in initial stage estimates, where limited point number reduces statistical power for subtle pattern detection. Limited external band availability, restricted to ExtRot 4 mode only (Zhang et al., 2000; Nasdala et al., 2008), limits conclusion generalization about external mode behavior during annealing. The low-frequency spectral range (195-230 cm^{-1}), corresponding to ExtRot 1, 2, and 3 modes, presents particular challenges for automatic spectrum processing due to polarization-dependent shift related to crystallinity increase during annealing, as documented by Dias et al. (2020). This behavior, involving shifts from approximately 202 cm^{-1} to 224 cm^{-1} with structural recovery, reflects changes in zircon global structural order and constitutes subject for later study with neural network and machine learning application in attempt to obtain reliable data from this spectral range.

Relatively wide bootstrap confidence intervals (350–600 K for T_max in H2) reflect a fundamental limitation despite the experimental design optimization. Although experimental conditions were guided by D-optimal planning to maximize global statistical information for kinetic parameter estimation, the D-optimality criterion operates in the space of global Arrhenius model parameters and is not specifically optimized to constrain the precise position of local extrema of derivatives that define T_max. Thus, while complete bootstrap convergence indicates internal statistical stability and robustness in identifying kinetic regimes, thermal resolution remains insufficient for precise determination of point temperatures directly comparable to literature values.

Moreover, the use of T × t as a single annealing parameter implies the Time-Equivalent Principle (PET), which is not strictly valid across stages with different activation energies. Consequently, the empirical GAM model, while capturing the shape of recovery trajectories, inherits the PET limitation and does not account for path-dependent thermal histories.

In this context, T_max values should be interpreted as central estimates of broad thermal domains rather than strict closure temperatures. The limited number of experimental temperature points (n = 9) imposes this constraint.

Future studies should adopt hierarchical experimental design strategies, combining an initial global exploration stage based on D-optimality with a subsequent local thermal refinement stage guided by the curvature of spectral trajectories, thereby reducing uncertainty associated with critical temperatures and strengthening inter-experimental comparability.

Propagation of uncertainties in critical thermal parameters constitutes a recurring methodological challenge in organic and inorganic geochemistry (Yang & Horsfield, 2020). Stratification by Geisler stage (Geisler, 2002) depends on thresholds derived from empirical data that consider discrepancies of at least 100 K relative to literature values, introducing additional uncertainty in classification of observations by stage.

3.2 SAXS

Figure 15 presents the SAXS scattering intensity curves obtained for seven zircon samples after swift heavy-ion irradiation. The experimental data were fitted using the hard cylinder model with Gaussian polydispersity, and the extracted track parameters are summarized in Table 12.

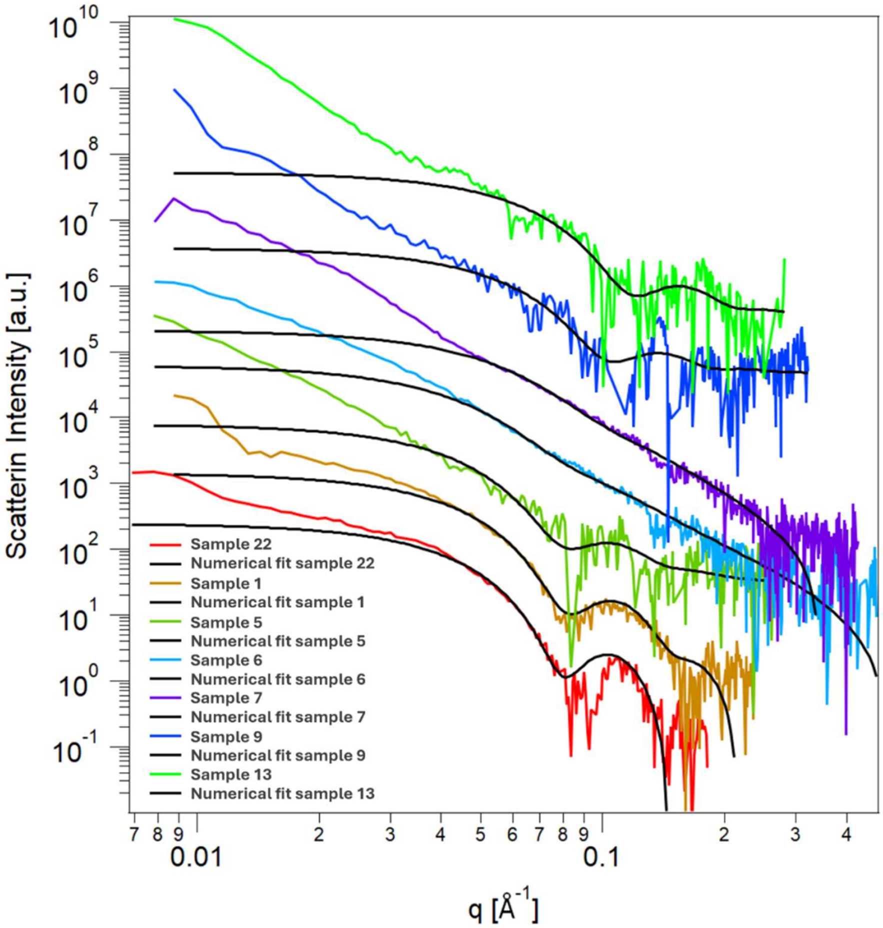

Figure 15 -SAXS scattering curves for irradiated zircon samples. SAXS scattering intensity curves as a function of scattering vector q for seven swift heavy-ion irradiated zircon samples. Experimental data (colored lines) and corresponding numerical fits using the hard

cylinder model with Gaussian polydispersity (black lines) are displayed on a log-log scale. Curves are vertically offset for clarity. Samples shown: 22 (red), 1 (orange), 5 (olive), 6 (cyan), 7 (purple), 9 (blue), and 13 (green). The characteristic oscillations at higher q values arise from the cylindrical form factor and reflect differences in ion track radii between samples, ranging from 3.32 nm (Sample 13) to 4.99 nm (Sample 22).

Table 12: SAXS and Raman Parameters for Irradiated Zircon Samples

Sample	Radius [nm]	σ [nm]	FWHM $\nu_3(SiO_4)$ [cm^{-1}]
22	4.99	0.58	7.38
1	4.85	0.61	13.11
5	4.95	0.77	10.99
6	4.55	1.15	10.90
7	3.96	0.96	10.86
9	3.75	0.41	10.89
13	3.32	0.39	13.05

3.2.1 Ion Track Formation and Thermal Spike Mechanism

The formation of ion tracks in zircon ($ZrSiO_4$) occurs through the thermal spike mechanism, wherein intense electronic excitation produced by swift heavy ions leads to localized melting and amorphization along the ion trajectory. The subsequent rapid cooling, with characteristic timescales of 10^{-11} to 10^{-9} seconds, quenches the molten material into an amorphous phase before crystallization can occur (Kluth et al., 2008).

The dimensions of the resulting ion track are determined by the spatial distribution of energy deposition. The electronic stopping power (dE/dx) of the incident ion is the primary factor controlling track radius. Experimental measurements demonstrate an approximately linear relationship between track radius and electronic stopping power in the regime relevant to fission track thermochronology (approximately 10 to 30 keV/nm). The threshold for track formation in zircon has been estimated at approximately 5 keV/nm (Afra et al., 2012).

SAXS measurements have established that ion tracks in zircon exhibit cylindrical morphology with characteristic radii in the 3-5 nanometer range for typical fission fragment energies. The shape of ion tracks varies with ion velocity, with faster ions producing more elongated tracks (Schauries et al., 2014). For example, irradiation with 2.2 GeV Au ions ($dE/dx \approx 22$ keV/nm) produces tracks with radii of approximately 4-5 nm in zircon (Afra et al., 2011). Studies on apatite have shown that track dimensions exhibit temperature dependence during formation, with radius variations of approximately 0.1 nm per 100 K change in temperature (Schauries et al., 2013).

The electron density contrast between amorphous track and crystalline matrix has been determined to be approximately 1-2% lower in the track region (Afra et al., 2011).

3.2.2 Annealing Behavior of Ion Tracks

Upon heating, ion tracks undergo structural modifications leading to recovery of the original crystalline structure. The annealing behavior of ion tracks typically exhibits two distinct stages with different temperature dependencies and physical mechanisms (Afra et al., 2011).

The first stage of annealing occurs at relatively low temperatures (typically below 300°C in apatite) and is characterized by rapid initial recovery with a low activation energy of approximately 0.23 ± 0.05 eV. The rate of radius reduction during this stage can be approximately 0.02 nm/minute in early phases of annealing (Afra et al., 2011).

The second stage of annealing, occurring at higher temperatures (above 300°C), involves recrystallization through interface-controlled growth with a higher activation energy of approximately 0.72 ± 0.02 eV. The recrystallization rate is significantly slower, typically on the order of 0.003 nm/minute after the first 15 minutes of annealing at 350°C (Afra et al., 2011).

Recent studies reveal more complex annealing behavior in amorphous materials, with significant depth-dependent effects. Investigation of ion tracks in amorphous silicon dioxide (a-SiO_2) demonstrates that annealing proceeds preferentially from the sample surface inward above approximately 250°C. The depth-dependent annealing is characterized by distinct activation energies: approximately 0.108 eV at the surface, 0.157 eV at depths around 210 nm, and 0.204 eV at depths of approximately 500 nm (Dutt et al., 2023).

The electron density contrast between ion tracks and the surrounding matrix evolves during thermal annealing, providing additional information about the recovery process. At temperatures sufficiently high for complete annealing (approximately 500°C for apatite), no residual scattering from tracks can be detected (Afra et al., 2011).

3.2.3 Analysis of Zircon Sample Data

Quantitative analysis of the SAXS fitting results presented in Table 12 and illustrated in Figure 15 reveals distinct patterns providing insights into the relationship between nanoscale ion track morphology and local vibrational disorder in zircon. Sample 22 exhibits the largest track radius (4.99 nm) combined with the lowest FWHM value (7.38 cm^{-1}), indicating the highest degree of crystallinity. In contrast, Sample 13 presents the smallest track radius (3.32 nm) but a relatively high FWHM value (13.05 cm^{-1}), suggesting that smaller track radius is not necessarily correlated with lower vibrational disorder. Samples 5, 6, 7, and 9 form an intermediate group with track radii ranging between 3.75 and 4.95 nm and relatively consistent FWHM values around 10.9 cm^{-1}.

The relationship between SAXS-derived track radii and Raman FWHM across the seven samples is not simply linear. Sample 22 exhibits the largest track radius (4.99 nm) and the lowest FWHM (7.38 cm^{-1}), consistent with a high degree of crystalline order and well-preserved track morphology. At the opposite extreme, Sample 13 presents the smallest radius (3.32 nm) but a relatively high FWHM (13.05 cm^{-1}), contradicting any simple expectation that smaller tracks correlate with lower vibrational disorder. This apparent anomaly suggests that track radius and local vibrational coherence, though both products of the radiation damage process, respond to different structural features: SAXS is sensitive to the nanoscale electron-density contrast of the damage cylinder, whereas Raman FWHM reflects short-range Si–O bond distortions within the surrounding matrix. The decoupling observed in Sample 13 could arise from compositional heterogeneity, residual strain fields beyond the SAXS-resolved track core, or incomplete recovery of the tetrahedral network despite partial track shrinkage. These observations underscore the need for caution when calibrating Raman thermochronometer against track dimensions, as the two techniques probe structurally distinct aspects of radiation damage (Anderson et al., 2020).

4. CONCLUSIONS

4.1 RAMAN SPECTROSCOPY APPROACH

4.1.1Evaluating Raman spectral preprocessing strategies for radiation damage assessment in zircon

Mode-specific optimization established quantitative principles for personalized preprocessing method selection in zircon Raman spectroscopy. The $\nu_3(SiO_4)$ mode demonstrated optimal performance with Spline_Min_max ($R^2 = 0.999$, CV FWHM = 4.48%), while ν_1 and $\nu_2(SiO_4)$ modes achieved superior results with Polynomial_Area ($R^2 = 0.999$-1.000). Statistical validation confirmed Min-Max normalization superiority (H2 confirmed).

H1 was rejected globally on the basis of performance equivalence ($\Delta R^2 = 0.001$), consistent with the observation that polynomial and spline baselines yield comparable fit quality; mode-specific analysis, however, revealed that spline baseline correction outperforms polynomial for $\nu_3(SiO_4)$, grounding the recommendation for mode-dependent preprocessing optimization. Optimized combinations reduced line width variability and increased high-quality fit percentages (H3 and H4 confirmed).

The adaptive damage categorization framework, validated by ECDF analysis of normalized FWHM values, enables quantitative radiation damage assessment across the full zircon spectrum. The sensitivity hierarchy reveals specific patterns: External Mode 4 exhibits the narrowest FWHM distribution (12.12 cm^{-1}), while External Mode 1 shows the broadest (20.26 cm^{-1}), demonstrating mode-specific sensitivity that enhances analytical precision. These results establish foundations for advances in spectroscopic analysis for radiation damage assessment and geochronological applications, with implications for materials science and mineralogy, where systematic preprocessing optimization enhances analytical precision and inter-laboratory comparability.

4.1.2Zircon Annealing Dynamics

Systematic investigation of crystalline recovery in zircon via Raman spectroscopy, based on statistical analysis of 6,225 valid observations, enabled establishment of conclusions about structural restoration mechanisms in partially metamict materials. The methodological approach employing complementary techniques (GAM, segmented regression, paired bootstrap, stratified variance analysis) enabled capture of different aspects of spectral parameter and thermal history relationship, resulting in comprehensive recovery process framework.

Hypothesis H1-GAM was confirmed, demonstrating that normalized FWHM recovery trajectories differ qualitatively between external (ExtRot) and internal (SiO_4) modes, with ΔAIC = 292 and only 56% confidence interval overlap. This differentiation reflects operation of distinct recovery mechanisms at each spatial scale, with long-range order responding preferentially to low activation energy processes characteristic of Stage I.

Hypothesis H2-Breakpoints was confirmed, with inflection points identified at 575 K (ExtRot, Stage I) and 662–684 K (SiO_4, Stage II), and stage transition breakpoints located at 607 K and 840 K. These values validate the three-stage structure of Geisler's phenomenological model, though with systematic deviations relative to reference temperatures reflecting experimental system specificities.

Hypothesis H4-Coupling was not confirmed, with $\Delta r = -0.125$ difference ($p = 1.0$) demonstrating that ν_2 correlates more strongly with ν_3 than with ExtRot. This result indicates that internal tetrahedral modes share recovery mechanisms independent of processes affecting coordination polyhedra spatial orientation, with implications for understanding zircon damage and restoration physical mechanisms.

Hypothesis H5-Monotonicity was partially confirmed, with ExtRot/ν_3 ratio presenting non-monotonic behavior characterized by peak at 622 K, situated in Stage II. This pattern reveals competition between recovery mechanisms with distinct kinetics, resulting in dominance inversion at intermediate temperature.

Hypothesis H6-Heterogeneity was partially confirmed, with ExtRot CV exceeding SiO_4 in Stages I and II (ratios 1.56 and 1.48) but presenting inversion in Stage III (ratio 0.92). This inversion indicates that partial recrystallization processes affect internal mode variability more intensely, suggesting bimodal structural heterogeneity at local tetrahedron scale.

Results are consistent with Geisler's three-stage phenomenological model and corroborate differentiated Raman band sensitivity to thermal annealing, grounding low-temperature thermochronology applications and establishing quantitative basis for spectral thermometer calibration. Qualitative differentiation between external and internal modes suggests that multi-band approaches offer advantages over single-band analysis, enabling extraction of complementary information about thermal history and metamictization state of zircon samples.

Finally, it should be noted that the use ofT×t as a single annealing parameter implies the Time-Equivalent Principle, which is not strictly valid across stages governed by different activation energies. Future thermochronological applications of the framework developed here will therefore require explicit treatment of time–temperature paths, ideally through Bayesian trans dimensional inversion.

4.2 SAXS APPROACH

SAXS results complement information obtained from Raman spectroscopy. The integration of these techniques offers more complete characterization of track structure than either technique alone. The FWHM of Raman bands increases with accumulated radiation damage, reflecting progressive loss of crystalline order. This damage indicator correlates with track radius and density contrast measured by SAXS (Tamer et al., 2017).

The static SAXS characterization of seven irradiated zircon samples yielded track radii in the range 3.32–4.99 nm, consistent with expectations for the accumulated dose range studied. The non-linear relationship between track radius and Raman FWHM — particularly the anomalous behaviour of the sample with the smallest radius but relatively high vibrational disorder — indicates that nanoscale track morphology and short-range vibrational coherence respond to structurally distinct aspects of radiation damage. Future work incorporating SAXS annealing series, as performed by Afra et al. (2011) for apatite, would allow kinetic parameterization of track recovery at the nanoscale and strengthen the integration of SAXS and Raman thermochronology.

Transmission electron microscopy (TEM) was included in the original scope of this thesis and is reflected in its title. However, the TEM stage could not be performed because the irradiated samples sent to the Australian Synchrotron for SAXS characterization were not returned to the author. The absence of TEM data limits the conclusions about nanoscale track morphology to what SAXS can resolve — track radii and polydispersity. Direct crystallographic imaging, which TEM would have provided, remains necessary to characterize domain boundaries, defect clusters, and amorphization gradients at the atomic scale. Future work should prioritize TEM analysis of samples spanning the three annealing stages identified in this thesis.

REFERENCES

AFRA, B. et al. Annealing kinetics of latent particle tracks in Durango apatite. **Physical Review B**, v. 83, 064116, 2011.

AFRA, B. et al. SAXS study of ion tracks in San Carlos olivine and Durango apatite. **Nuclear Instruments and Methods in Physics Research Section B**, v. 277, p. 76-80, 2012.

ANDERSON, A. J. et al. Mapping radiation damage zoning in zircon using Raman spectroscopy: Implications for zircon chronology. **Chemical Geology**, v. 538, 119494, 2020. DOI: https://doi.org/10.1016/j.chemgeo.2020.119494

BAEK, S. J. et al. Baseline correction using asymmetrically reweighted penalized least squares smoothing. **Analyst**, v. 140, n. 1, p. 250–257, 2014. DOI: https://doi.org/10.1039/C4AN01061B

BANERJEE, R. H. et al. Spectroscopic insights on defects in self-irradiated natural Zircon. **Spectrochimica Acta Part A**, v. 312, 124089, 2025. DOI: https://doi.org/10.1016/j.saa.2024.124089

BARBARAND, J. et al. Compositional and structural control of fission-track annealing in apatite. **Chemical Geology (Isotope Geoscience Section)**, v. 198, p. 107-138, 2003.

BERGER, A. et al. The relation between peak metamorphic temperatures and subsequent cooling during continent–continent collision (western Central Alps, Switzerland). **Swiss Journal of Geosciences**, v. 113, n. 1, 4, 2020. DOI: https://doi.org/10.1186/S00015-020-00356-4

BERRY, L. N.; HELWIG, N. E. Cross-validation, information theory, or maximum likelihood? A comparison of tuning methods for penalized splines. **Stats**, v. 4, n. 3, p. 701-724, 2021. DOI: https://doi.org/10.3390/stats4030042

BIERSCHENK, T. et al. Latent ion tracks in amorphous silicon. **Physical Review B**, v. 88, 174111, 2013.

BJERGA, A. et al. Radiation damage allows identification of truly inherited zircon. **Communications Earth &Environment**, v. 3, 68, 2022. DOI: https://doi.org/10.1038/s43247-022-00372-2

BOCKLITZ, T. et al. How to pre-process Raman spectra for reliable and stable models? **AnalyticaChimica Acta**, v. 704, n. 1–2, p. 47–56, 2011. DOI: https://doi.org/10.1016/J.ACA.2011.06.043

BURGER, D. A.; VAN DER MERWE, S.; VAN STADEN, P. J. Addressing outliers in mixed-effects logistic regression: a more robust modeling approach. **Journal of Applied Statistics**, 2025. DOI: https://doi.org/10.1080/02664763.2025.2538076

BURNHAM, K. P.; ANDERSON, D. R. **Model Selection and Multimodel Inference: A Practical Information-Theoretic Approach**. 2. ed. New York: Springer, 2002. DOI: https://doi.org/10.1007/b97636

CAMERON, J. A test for heteroscedasticity in functional linear models. **TEST**, v. 31, p. 875–898, 2022. DOI: https://doi.org/10.1007/s11749-021-00786-8

CAPITANI, G. C. et al. A TEM investigation of natural metamict zircons: structure and recovery of amorphous domains. **Physics and Chemistry of Minerals**, v. 27, n. 8, p. 545-556, 2000. DOI: https://doi.org/10.1007/s002690000100

CHEN, X. et al. Adaptive Raman spectral unmixing method based on Voigt peak compensation for quantitative analysis of cellular biochemical components. **Biomedical Optics Express**, v. 16, n. 3, p. 1284–1298, 2025. DOI: https://doi.org/10.1364/BOE.553461

CHESNAYE, N. C. et al. Non-linear relationships in clinical research. **Nephrology Dialysis Transplantation**, v. 40, n. 2, p. 244–254, 2025. DOI: https://doi.org/10.1093/ndt/gfae187

CHICCO, D.; WARRENS, M. J.; JURMAN, G. The coefficient of determination R-squared is more informative than SMAPE, MAE, MAPE, MSE and RMSE in regression analysis evaluation. **PeerJ Computer Science**, v. 7, e623, 2021. DOI: https://doi.org/10.7717/peerj-cs.623

CROWLEY, K. D.; CAMERON, M.; SHAEFER, R. L. Experimental studies of annealing of etched fission tracks in fluor apatite. **Geochimica et Cosmochimica Acta**, v. 55, p. 1449-1465, 1991.

DAMMANN, L. M. et al. Gradient-based smoothing parameter estimation for neural P-splines. **Computational Statistics**, 2025. DOI: https://doi.org/10.1007/s00180-024-01593-z

DAWSON, P.; HARGREAVE, M. M.; WILKINSON, G. R. The vibrational spectrum of zircon (ZrSiO4). **Journal of Physics C: Solid State Physics**, v. 4, n. 2, p. 240–256, 1971. DOI: https://doi.org/10.1088/0022-3719/4/2/014

DE BOOR, C. **A Practical Guide to Splines**. 1. ed. New York: Springer, 2001.

DIAS, A. N. C. et al. Micro-Raman spectroscopy and SEM/EDX applied to improve the zircon fission track method used for dating geological formations. **Journal of Raman Spectroscopy**, v. 40, n. 1, p. 101–106, 2009. DOI: https://doi.org/10.1002/jrs.2088

DIAS, A. N. C. et al. Micro-Raman Spectroscopy of Zircon (ZrSiO4) Mineral at Annealing Conditions Usually Applied in Zircon Fission-Track Annealing Dataset. **Journal of Nanoscience and Nanotechnology**, v. 20, n. 3, p. 1884–1891, 2019. DOI: https://doi.org/10.1166/JNN.2020.17172

DODSON, M. H. Closure temperature in cooling geochronological and petrological systems. **Contributions to Mineralogy and Petrology**, v. 40, n. 3, p. 259-274, 1973. DOI: https://doi.org/10.1007/BF00373790

DONG, Z. **Arsenic Contamination in Nova Scotias Private Well Water: A Spatial-Temporal Statistical Analysis**. 2024. Tese (Doutorado) – Dalhousie University, Halifax, 2024.

DUTT, S. et al. Annealing of swift heavy ion tracks in amorphous silicon dioxide. **Applied Surface Science**, 157370, 2023.

EFRON, B.; TIBSHIRANI, R. J. **An Introduction to the Bootstrap**. Boca Raton: Chapman & Hall/CRC, 1993. DOI: https://doi.org/10.1201/9780429246593

ENDE, M. et al. Dry annealing of radiation-damaged zircon: Single-crystal X-ray and Raman spectroscopy study. **Lithos**, v. 406–407, 106523, 2021. DOI: https://doi.org/10.1016/J.LITHOS.2021.106523

EWING, R. C. et al. Radiation effects in zircon. **Reviews in Mineralogy and Geochemistry**, v. 53, n. 1, p. 387-425, 2003. DOI: https://doi.org/10.2138/rmg.2003.53.14

FAN, M. et al. Effect of chemical composition on zircon radiation damage dating: Implications for low-temperature thermochronology. **Geoscience Frontiers**, v. 14, n. 6, 101675, 2023. DOI: https://doi.org/10.1016/j.gsf.2023.101675

FAN, M. et al. Optimization of standard zircon U–Pb dating: insights into high-temperature thermal annealing. **Journal of Analytical Atomic Spectrometry**, v. 39, p. 512-525, 2024. DOI: https://doi.org/10.1039/D3JA00407D

FATIMA, A. et al. Towards normalization selection of Raman data in the context of protein glycation: application of validity indices to PCA processed spectra. **Analyst**, v. 145, n. 8, p. 2945–2957, 2020. DOI: https://doi.org/10.1039/C9AN02155H

GALLAGHER, K. Transdimensional inverse thermal history modeling for quantitative thermochronology. **Journal of Geophysical Research: Solid Earth**, v. 117, B2, B02408, 2012. DOI: https://doi.org/10.1029/2011JB008825

GAO, S.; HEIDE, G. Influence of metamictization on the gemological properties of natural zircon: A Raman spectroscopic study of zircons in the gemological collection of Abraham Gottlob Werner. **Journal of Raman Spectroscopy**, v. 52, n. 1, p. 71–77, 2020. DOI: https://doi.org/10.1002/jrs.6041

GAUTAM, R. et al. Review of multidimensional data processing approaches for Raman and infrared spectroscopy. **EPJ Techniques and Instrumentation**, v. 2, n. 1, p. 8, 2015. DOI: https://doi.org/10.1140/EPJTI/S40485-015-0018-6

GEISLER, T. Isothermal annealing of partially metamict zircon: Evidence for a three-stage recovery process. **Physics and Chemistry of Minerals**, v. 29, n. 6, p. 420–429, 2002. DOI: https://doi.org/10.1007/S00269-002-0249-3

GEISLER, T. et al. Kinetics of thermal recovery and recrystallization of partially metamict zircon: a Raman spectroscopic study. **European Journal of Mineralogy**, v. 13, n. 6, p. 1163–1176, 2001. DOI: https://doi.org/10.1127/0935-1221/2001/0013-1163

GEISLER, T. et al. Leaching and differential recrystallization of metamict zircon under experimental hydrothermal conditions. **Contributions to Mineralogy and Petrology**, v. 141, p. 53-65, 2001. DOI: https://doi.org/10.1007/s004100000202

GEORGIEV, D. et al. RamanSPy: An Open-Source Python Package for Integrative Raman Spectroscopy Data Analysis. **Analytical Chemistry**, v. 96, n. 21, p. 8492–8500, 2024. DOI: https://doi.org/10.1021/ACS.ANALCHEM.4C00383

GINSTER, U. et al. Annealing kinetics of radiation damage in zircon. **Geochimica et Cosmochimica Acta**, v. 249, p. 225–246, 2019. DOI: https://doi.org/10.1016/j.gca.2019.01.033

GLACE, M. et al. Iterative Regression of Corrective Baselines (IRCB): A New Model for Quantitative Spectroscopy. **Journal of Chemical Information and Modeling**, v. 64, n. 13, p. 5006–5015, 2024. DOI: https://doi.org/10.1021/ACS.JCIM.4C00359

GLEADOW, A. J. W. et al. Fission Track Dating of Phosphate Minerals and the Thermochronology of Apatite. **Reviews in Mineralogy and Geochemistry**, v. 48, n. 1, p. 579–630, 2002.

GÖTZE, J. Application of cathodoluminescence microscopy and spectroscopy in geosciences. **Microscopy and Microanalysis**, v. 18, n. 6, p. 1270–1284, 2012. DOI: https://doi.org/10.1017/S1431927612001122

GREEN, P. F. et al. Thermal annealing of fission tracks in apatite, 1. A Qualitative description. **Chemical Geology (Isotope Geoscience Section)**, v. 59, p. 237-253, 1986.

GU, L. et al. Application of FIB-SEM Techniques for the Advanced Characterization of Earth and Planetary Materials. **Scanning**, v. 2020, n. 1, 8406917, 2020. DOI: https://doi.org/10.1155/2020/8406917

GUO, S.; POPP, J.; BOCKLITZ, T. Chemometric analysis in Raman spectroscopy from experimental design to machine learning–based modeling. **NatureProtocols**, v. 16, n. 12, p. 5426–5459, 2021. DOI: https://doi.org/10.1038/s41596-021-00620-3

GUO, S.; POPP, J.; BOCKLITZ, T. Key Steps in the Workflow to Analyze Raman Spectra. **Spectroscopy**, v. 38, p. 30–33, 2023. Disponível em: https://www.spectroscopyonline.com/view/key-steps-in-the-workflow-to-analyze-raman-spectra.

GUO, S. et al. Long-term device stability for Raman spectroscopy. **Analyst**, v. 150, n. 13, p. 2854–2864, 2025. DOI: https://doi.org/10.1039/D5AN00255A

GUZIK, P.; WIĘCKOWSKA, B. Data distribution analysis – a preliminary approach to quantitative data in biomedical research. **Journal of Medical Science**, v. 92, n. 1, e869, 2023. DOI: https://doi.org/10.20883/medical.e869

HAN, M.; DANG, Y.; HAN, J. Denoising and Baseline Correction Methods for Raman Spectroscopy Based on Convolutional Autoencoder: A Unified Solution. **Sensors**, v. 24, n. 10, 3161, 2024. DOI: https://doi.org/10.3390/S24103161

HÄRTEL, B.; JONCKHEERE, R.; WAUSCHKUHN, B.; RATSCHBACHER, L. The closure temperature(s) of zircon Raman dating. **Geochronology**, v. 3, n. 1, p. 259–272, 2021. DOI: https://doi.org/10.5194/GCHRON-3-259-2021

HÄRTEL, B.; JONCKHEERE, R.; RATSCHBACHER, L. Multi-Band Raman Analysis of Radiation Damage in Zircon for Thermochronology: Partial Annealing and Mixed Signals. **Geochemistry, Geophysics, Geosystems**, v. 23, n. 1, 2022. DOI: https://doi.org/10.1029/2021GC010182

HEIT, D. R. et al. Generalized nonlinearity in animal ecology: Research, review, and recommendations. **Ecology and Evolution**, v. 14, e11387, 2024. DOI: https://doi.org/10.1002/ece3.11387

HEYDE, C. C.; SENETA, E. When Heavy Tails Disrupt Statistical Inference. **The American Statistician**, v. 78, n. 4, p. 404–412, 2024. DOI: https://doi.org/10.1080/00031305.2024.2402898

HOSKIN, P.; RODGERS, K. A. Raman spectral shift in the isomorphous series (Zr1-xHfx)SiO4. **European Journal of Solid State and Inorganic Chemistry**, 1996.

KAMATH, A.; POOJARI, S.; VARSHA, K. Assessing the robustness of normality tests under varying skewness and kurtosis: a practical checklist for public health researchers. **BMC Medical Research Methodology**, v. 25, 123, 2025. DOI: https://doi.org/10.1186/s12874-025-02641-y

KANEKI, S. et al. An automatic peak deconvolution code for Raman spectra of carbonaceous material and a revised geothermometer for intermediate- to moderately high-grade metamorphism. **Progress in Earth and Planetary Science**, v. 11, n. 1, p. 1–14, 2024. DOI: https://doi.org/10.1186/S40645-024-00637-8

KIBRIA, M. G. et al. Thermal maturity evaluation using Raman spectroscopy for oil shale samples of USA: comparisons with vitrinite reflectance and pyrolysis methods. **Petroleum Science**, v. 17, n. 3, p. 567–581, 2020. DOI: https://doi.org/10.1007/S12182-020-00443-Z

KLUTH, P. et al. Fine structure in swift heavy ion tracks in a-SiO_2. **Physical Review Letters**, v. 101, 175503, 2008.

KOHN, B. P. et al. Interpreting and reporting fission-track chronological data. **GSA Bulletin**, v. 136, p. 3891–3920, 2024. DOI: https://doi.org/10.1130/B37245.1

KOLESOV, B. A.; GEIGER, C. A.; ARMBRUSTER, T. The dynamic properties of zircon studied by single-crystal X-ray diffraction and Raman spectroscopy. **European Journal of Mineralogy**, v. 13, n. 5, p. 939–948, 2001. DOI: https://doi.org/10.1127/0935-1221/2001/0013-0939

KRUSKAL, W. H.; WALLIS, W. A. Use of Ranks in One-Criterion Variance Analysis. **Journal of the American Statistical Association**, v. 47, n. 260, p. 583–621, 1952. DOI: https://doi.org/10.1080/01621459.1952.10483441

LAMMER, L. et al. Generalized additive mixed models to discern data-driven theoretically informed strategies for public brain, cognitive and mental health. **European Journal of Epidemiology**, 2025. DOI: https://doi.org/10.1007/s10654-025-01296-9

LEE, S. W. Methods for testing statistical differences between groups in medical research: statistical standard and guideline of Life Cycle Committee. **Life Cycle**, v. 2, e1, 2022. DOI: https://doi.org/10.54724/lc.2022.e1

LENZ, C.; BELOUSOVA, E.; LUMPKIN, G. R. The In-Situ Quantification of Structural Radiation Damage in Zircon Using Laser-Induced Confocal Photoluminescence Spectroscopy. **Minerals**, v. 10, n. 1, 83, 2020. DOI: https://doi.org/10.3390/min10010083

LEVENE, H. Robust tests for equality of variances. In: OLKIN, I. et al. (ed.). **Contributions to probability and statistics: Essays in honor of Harold Hotelling**. Stanford: Stanford University Press, 1960. p. 278-292.

LIU, X. et al. Selective iteratively reweighted quantile regression for baseline correction. **Analytical and Bioanalytical Chemistry**, v. 406, n. 7, p. 1985–1998, 2014. DOI: https://doi.org/10.1007/S00216-013-7610-X

MCKANNA, A. J. et al. Chemical abrasion: the mechanics of zircon dissolution. **Geochronology**, v. 5, n. 1, p. 127–151, 2023. DOI: https://doi.org/10.5194/GCHRON-5-127-2023

MIDWAY, S.; WHITE, J. W. Testing for normality in regression models: mistakes abound (but may not matter). **Royal Society Open Science**, v. 12, n. 4, 241904, 2025. DOI: https://doi.org/10.1098/rsos.241904

MILLER, D. L. Bayesian views of generalized additive modelling. **Methods in Ecology and Evolution**, v. 16, n. 3, e14498, 2025. DOI: https://doi.org/10.1111/2041-210X.14498

MITTAL, R. et al. Lattice dynamics calculations and phonon dispersion measurements of zircon, ZrSiO4. **Physical Review B (Condensed Matter)**, v. 62, n. 18, p. 12089–12094, 2000. DOI: https://doi.org/10.1103/PHYSREVB.62.12089

MOERHUIS, N. et al. Zircon Morphology and Geochemical Diversity During Closed-System Crystallization of the Skaergaard Intrusion. **Journal of Petrology**, v. 66, n. 4, 30, 2025. DOI: https://doi.org/10.1093/PETROLOGY/EGAF030

MOREIRA, P. A. F. P. et al. D-optimal design of fission-track annealing experiments. **Nuclear Instruments and Methods in Physics Research Section B: Beam Interactions with Materials and Atoms**, v. 240, n. 4, p. 881-887, 2005. DOI: https://doi.org/10.1016/j.nimb.2005.06.212

MOTA-SANTIAGO, P. et al. Nanoscale density variations induced by high energy heavy ions in amorphous silicon nitride and silicon dioxide. **Nanotechnology**, v. 29, 144004, 2018.

MOTA-SANTIAGO, P. et al. Nanoscale density variations induced by high energy heavy ions in amorphous silicon nitride and silicon dioxide. **Journal of Physics D: Applied Physics**, v. 55, 145301, 2022.

MURAKAMI, T. et al. Alpha-Decay Event Damage in Zircon. **American Mineralogist**, v. 76, n. 9-10, p. 1510-1532, 1991.

NASDALA, L.; IRMER, G.; WOLF, D. The degree of metamictization in zircon: a Raman spectroscopic study. **European Journal of Mineralogy**, v. 7, n. 3, p. 471–478, 1995.

NASDALA, L. et al. Metamictisation of natural zircon: accumulation versus thermal annealing of radioactivity-induced damage. **Contributions to Mineralogy and Petrology**, v. 141, p. 125-144, 2001. DOI: https://doi.org/10.1007/s004100000235

NASDALA, L. et al. Annealing radiation damage and the recovery of cathodoluminescence. **Chemical Geology**, v. 191, n. 1-3, p. 121-140, 2002. DOI: https://doi.org/10.1016/S0009-2541(02)00152-3

NASDALA, L. et al. Spectroscopic methods applied to zircon. **Reviews in Mineralogy and Geochemistry**, v. 53, n. 1, p. 427–467, 2003. DOI: https://doi.org/10.2113/0530427

NASDALA, L.; MILETICH, R.; RUSCHEL, K.; VÁCZI, T. Raman study of radiation-damaged zircon under hydrostatic compression. **Physics and Chemistry of Minerals**, v. 35, p. 597-602, 2008. DOI: https://doi.org/10.1007/s00269-008-0251-5

OSÓRIO A, A. M. et al. Fission-track dating of Macusanite glasses using natural uranium and thorium thin films neutron dosimetry. **Geotemas**, v. 4, p. 125-127, 2002.

PALENIK, C. S.; NASDALA, L.; EWING, R. C. Radiation damage in zircon. **American Mineralogist**, v. 88, n. 5–6, p. 770–781, 2003. DOI: https://doi.org/10.2138/am-2003-5-606

PELL, R. J. Multiple outlier detection for multivariate calibration using robust statistical techniques. **Chemometrics and Intelligent Laboratory Systems**, v. 52, n. 1, p. 87–104, 2000. DOI: https://doi.org/10.1016/S0169-7439(00)00082-4

PIATT, J. Overlapping confidence intervals. **Journal of Neurosurgery**, v. 137, n. 4, p. 1195, 2022. DOI: https://doi.org/10.3171/2022.1.JNS212795

PIDGEON, R. T. et al. Dry annealing of metamict zircon: A differential scanning calorimetry study. **American Mineralogist**, v. 102, n. 5, p. 1015–1023, 2017. DOI: https://doi.org/10.2138/am-2017-5901

REZVUKHINA, O. V. et al. Zircon from diamondiferous kyanite gneisses of the Kokchetav massif: Revealing growth stages using an integrated cathodoluminescence, Raman spectroscopy and electron microprobe approach. **Mineralogical Magazine**, v. 84, n. 6, p. 949–958, 2020. DOI: https://doi.org/10.1180/MGM.2020.95

RIBEIRO, C. V. A.; DANTAS, E. L.; FUCK, R. A. Effects of high-temperature annealing and low-temperature metamictization on Archean zircon. **American Mineralogist**, v. 110, p. 234-248, 2025. DOI: https://doi.org/10.2138/am-2024-9502

RIMPLER, A.; KIERS, H. A. L.; VAN RAVENZWAAIJ, D. To interact or not to interact: The pros and cons of including interactions in linear regression models. **Behavior Research Methods**, 2025. DOI: https://doi.org/10.3758/s13428-025-02613-6

RÍOS, S.; BOFFA-BALLARAN, T. Microstructure of radiation-damaged zircon under pressure. **Journal of Applied Crystallography**, v. 36, n. 4, p. 1006–1012, 2003. DOI: https://doi.org/10.1107/S0021889803008574

ROMO-CHAVERO, M. A. et al. Median Absolute Deviation for BGP Anomaly Detection. **Future Internet**, v. 16, n. 5, 146, 2024. DOI: https://doi.org/10.3390/FI16050146

RYABCHYKOV, O. et al. Errors and Mistakes to Avoid when Analyzing Raman Spectra. **Spectroscopy**, v. 37, n. 4, p. 48–50, 2022. DOI: https://doi.org/10.56530/SPECTROSCOPY.ZZ8373X6

SADAT, A.; JOYE, I. J. Peak Fitting Applied to Fourier Transform Infrared and Raman Spectroscopic Analysis of Proteins. **Applied Sciences**, v. 10, n. 17, 5918, 2020. DOI: https://doi.org/10.3390/APP10175918

SADERGASKI, L. R.; HAGER, T. J.; ANDREWS, H. B. Design of Experiments, Chemometrics, and Raman Spectroscopy for the Quantification of Hydroxylammonium, Nitrate, and Nitric Acid. **ACS Omega**, v. 7, n. 8, p. 7287–7296, 2022. DOI: https://doi.org/10.1021/ACSOMEGA.1C07111

SÁENZ, C. A. T. et al. Effects of Etching on Zircon Grains and its Implications for the Fission Track Method. **Applied Spectroscopy**, v. 66, n. 5, p. 545–551, 2012. DOI: https://doi.org/10.1366/11-06260

SÄFKEN, B.; KNEIB, T.; WOOD, S. N. On the degrees of freedom of the smoothing parameter. **Biometrika**, v. 112, n. 1, asae052, 2025. DOI: https://doi.org/10.1093/biomet/asae052

SALES, A. S. W. et al. **Systematic Optimization of Raman Spectral Preprocessing for Zircon Geochronology: A Comprehensive Framework for Radiation Damage Assessment**. 2026. (in preparation).

SALJE, E. K. H.; RÍOS, S. Mineral physics: the atomic, mesoscopic and macroscopic perspective. **Mineralogical Magazine**, v. 66, n. 5, p. 733–744, 2002. DOI: https://doi.org/10.1180/0026461026650058

SAVITZKY, A.; GOLAY, M. J. E. Smoothing and Differentiation of Data by Simplified Least Squares Procedures. **Analytical Chemistry**, v. 36, n. 8, p. 1627–1639, 2002. DOI: https://doi.org/10.1021/AC60214A047

SCHAUER, J. M.; HEDGES, L. V. Reconsidering statistical methods for assessing replication. **Psychological Methods**, v. 26, n. 1, p. 127-139, 2021. DOI: https://doi.org/10.1037/met0000302

SCHAURIES, D. et al. Temperature dependence of ion track formation in quartz and apatite. **Journal of Applied Crystallography**, v. 46, p. 1558-1563, 2013.

SCHAURIES, D. et al. The shape of ion tracks in natural apatite. **Nuclear Instruments and Methods in Physics Research Section B**, v. 326, p. 117-120, 2014.

SCHAURIES, D. et al. Structure, morphology and annealing behavior of ion tracks in polycarbonate. **European Polymer Journal**, v. 106, p. 136-148, 2018.

SCHWARZ, W. The Ancova model for comparing two groups: a tutorial emphasizing statistical distribution theory. **Frontiers in Psychology**, v. 16, 1600764, 2025. DOI: https://doi.org/10.3389/fpsyg.2025.1600764

SERVÉN, D.; BRUMMITT, C. **pyGAM: Generalized Additive Models in Python (v0.4.1)**. Zenodo, 2018. DOI: https://doi.org/10.5281/zenodo.1208724

SHCHAPOVA, Y. V. et al. Short-range order and electronic structure of radiation-damaged zircon according to X-ray photoelectron spectroscopy. **Physics and Chemistry of Minerals**, v. 47, 52, 2020. DOI: https://doi.org/10.1007/s00269-020-01120-8

SHCHAPOVA, Y. V.; KRYLOV, A. S.; VOTYAKOV, S. L. Structural characteristics of radiation-amorphized $ZrSiO_4$:U,Th according to Raman spectroscopy of Boson peak. **Journal of Raman Spectroscopy**, v. 54, n. 6, p. 662–673, 2023. DOI: https://doi.org/10.1002/jrs.6525

SHI, G. et al. A zircon classification scheme for sedimentary provenance analysis using radiation damage. **Geological Journal**, v. 58, n. 8, p. 3087–3095, 2023. DOI: https://doi.org/10.1002/GJ.4751

SHIMIZU, Y. Multiple Desirable Methods in Outlier Detection of Univariate Data With R Source Codes. **Frontiers in Psychology**, v. 12, 2022. DOI: https://doi.org/10.3389/fpsyg.2021.819854

SMIRNOV, M. B.; SUKHOMLINOV, S. V.; SMIRNOV, K. S. Vibrational spectrum of reidite ZrSiO4 from first principles. **Physical Review B**, v. 82, n. 9, 094307, 2010. DOI: https://doi.org/10.1103/PhysRevB.82.094307

SPARAVIGNA, A. C. **q-Gaussian and q-BWF functions for the deconvolution of Raman and infrared spectra of Calcite**. 2024. DOI: https://doi.org/10.26434/CHEMRXIV-2024-NSMCH

STORN, R.; PRICE, K. Differential Evolution - A Simple and Efficient Heuristic for Global Optimization over Continuous Spaces. **Journal of Global Optimization**, v. 11, n. 4, p. 341–359, 1997. DOI: https://doi.org/10.1023/A:1008202821328

SU, K. et al. Quantification of radiation damage in natural and synthetic zircon by Raman spectroscopy: application to low-temperature thermochronology. **Acta Geochimica**, v. 42, p. 623-637, 2023. DOI: https://doi.org/10.1007/s11631-023-00606-w

SYME, D. J. LOCKWOOD; KERR, H. J. Raman spectrum of synthetic zircon (ZrSiO4) and thorite (ThSiO4). **Journal of Physics C: Solid State Physics**, v. 10, n. 8, p. 1335, 1977. DOI: https://doi.org/10.1088/0022-3719/10/8/036

TAGLIAFERRO, A. et al. Introducing the Novel Mixed Gaussian-Lorentzian Lineshape in the Analysis of the Raman Signal of Biochar. **Nanomaterials**, v. 10, n. 9, 1748, 2020. DOI: https://doi.org/10.3390/NANO10091748

TAMER, Y.; GOLD, R.; DUMOND, G. SAXS analysis of the annealing behavior of fission tracks in apatite. **Chemical Geology**, v. 459, p. 43-55, 2017.

THÉRIAULT, R. et al. Check your outliers! An introduction to identifying statistical outliers in R with easy stats. **Behavior Research Methods**, v. 56, n. 4, p. 4162–4172, 2024. DOI: https://doi.org/10.3758/S13428-024-02356-W

THIELMANN, A.; KNEIB, T.; SÄFKEN, B. Enhancing adaptive spline regression: An evolutionary approach to optimal knot placement and smoothing parameter selection. **Journal of Computational and Graphical Statistics**, 2025. DOI: https://doi.org/10.1080/10618600.2025.2450458

TORIBIO, M. R.-H. et al. A Novel Approach to Speed Up Hampel Filter for Outlier Detection. **Sensors**, v. 25, n. 11, 3319, 2025. DOI: https://doi.org/10.3390/S25113319

UTSUNOMIYA, S.; WANG, L. M.; EWING, R. C. Ion irradiation effects in natural garnets: Comparison with zircon. **Nuclear Instruments and Methods in Physics Research Section**

B: Beam Interactions with Materials and Atoms, v. 191, n. 1–4, p. 600–605, 2002. DOI: https://doi.org/10.1016/S0168-583X(02)00618-3

VONLANTHEN, P. et al. Recrystallization rims in zircon (Valle d'Arbedo, Switzerland): An integrated cathodoluminescence, LA-ICP-MS, SHRIMP, and TEM study. **American Mineralogist**, v. 97, n. 2-3, p. 369-377, 2012. DOI: https://doi.org/10.2138/am.2012.3978

VOTYAKOV, S. L. et al. CATHODOLUMINESCENCE AND RAMAN SPECTROSCOPY AS A BASIS FOR THE SELECTION OF REFERENCE SAMPLES FOR LA-ICP-MS ANALYSIS OF ZIRCON. **Geodinamika i Tektonofizika**, v. 13, n. 2, 2022. DOI: https://doi.org/10.5800/GT-2022-13-2S-0603

WANG, C. et al. Zircon Trace Elements as Indicators of Physicochemical Conditions and Mineralisation Potential in the Nannihu Porphyry Mo–W Deposit, East Qinling, China. **Geological Journal**, 2025. DOI: https://doi.org/10.1002/GJ.70024

WEBER, W. J. Alpha-Decay-Induced Amorphization in Complex Silicate Structures. **Journal of the American Ceramic Society**, v. 76, n. 7, p. 1729–1738, 1993. DOI: https://doi.org/10.1111/J.1151-2916.1993.TB06641.X

WEBER, W. J.; EWING, R. C.; WANG, L. M. The radiation-induced crystalline-to-amorphous transition in zircon. **Journal of Materials Research**, v. 9, n. 3, p. 688–698, 1994. DOI: https://doi.org/10.1557/JMR.1994.0688

WILKS, D. S. **Statistical Methods in Atmospheric Sciences**. 4. ed. Amsterdam: Elsevier, 2019. DOI: https://doi.org/10.1016/C2017-0-03921-6

WOOD, S. N. **Generalized additive models: An introduction with R**. 2. ed. Boca Raton: CRC Press, 2017. DOI: https://doi.org/10.1201/9781315370279

YANG, S.; HORSFIELD, B. Critical review of the uncertainty of Tmax in revealing the thermal maturity of organic matter in sedimentary rocks. **International Journal of Coal Geology**, v. 225, 103500, 2020. DOI: https://doi.org/10.1016/J.COAL.2020.103500

YUAN, X.; MAYANOVIC, R. A. An Empirical Study on Raman Peak Fitting and Its Application to Raman Quantitative Research. **Applied Spectroscopy**, v. 71, n. 10, p. 2325–2338, 2017. DOI: https://doi.org/10.1177/0003702817721527

ZAMYATIN, D. A. Application of Raman Spectroscopy for Studying Shocked Zircon from Terrestrial and Lunar Impactites: A Systematic Review. **Minerals**, v. 12, n. 8, 969, 2022. DOI: https://doi.org/10.3390/MIN12080969

ZHANG, M. et al. Metamictization of zircon: Raman spectroscopic study. **Journal of Physics: Condensed Matter**, v. 12, n. 9, p. 1915–1925, 2000.

ZHANG, M. et al. Annealing of α-decay damage in zircon: a Raman spectroscopic study. **Journal of Physics: Condensed Matter**, v. 12, p. 3131–3148, 2000. DOI: https://doi.org/10.1088/0953-8984/12/13/321

ZHENG, N.; CADIGAN, N. Improved confidence intervals for nonlinear mixed-effects and nonparametric regression models. **Annals of the Institute of Statistical Mathematics**, v. 77, p. 105–126, 2025. DOI: https://doi.org/10.1007/s10463-024-00909-6

APPENDIX 1

Information about the code/algorithm developed and presented in sections 1.1.1, 2.2.1, 3.1.1, and 4.1.1.

- Name of the code/library: ZIRCON RAMAN SPECTRAL ANALYSIS – Version 7.0 (batch_raman_backup_v7.0.py)
- Contact: Advisor – Prof. Dr. Airton Natanael Coelho Dias – diasanc@ufscar.br – Federal University of São Carlos (UFSCar) – Sorocaba, Brazil.
- Hardware requirements: Standard desktop or laptop computer with at least 8 GB RAM and a multi-core processor (Intel i5/equivalent or higher). No specialized hardware is required.
- Program language: Python 3.9 or higher.
- Software required: Python packages: NumPy (≥1.24), pandas (≥2.0), SciPy (≥1.10), Matplotlib (≥3.7).
- Standard Python libraries: pathlib, json, datetime, logging, os, re, glob, statistics.
- Program size: Main script: ~2000 lines of code. Full project (including configuration files, examples, and documentation) ~500 KB.
- The source codes are available for downloading at the link:https://github.com/AntonioSales254/Zircon_Geochronology_Raman_Spectral_Preprocessing.git

APPENDIX 2

Supplementary Material

Systematic Evaluation of Preprocessing Methods for Zircon Raman Spectroscopy: Comprehensive Analysis of Vibrational Modes and Radiation Damage Sensitivity

SECTION 1: PREPROCESSING METHODOLOGY

Table S1: Baseline and Normalization Method Combinations for Systematic Raman Spectrum Preprocessing

Method Combination	Baseline Type	Normalization Type
Polynomial + Area	Polynomial	Area
Polynomial + Min-Max	Polynomial	Min-Max
Polynomial + Peak	Polynomial	Peak
Polynomial + Vector	Polynomial	Vector
Spline + Area	Spline	Area
Spline + Min-Max	Spline	Min-Max
Spline + Peak	Spline	Peak
Spline + Vector	Spline	Vector
AirPLS + Area	AirPLS	Area
AirPLS + Min-Max	AirPLS	Min-Max
AirPLS + Peak	AirPLS	Peak
AirPLS + Vector	AirPLS	Vector

SECTION 2: HYPOTHESIS VALIDATION

Table S2: Test Parameters for Hypothesis Validation

Hypothesis	Test Parameter
H1	Global mean R^2
H2	Global mean R^2
H3	Best FWHM CV
H4	Best %R^2>0.9

SECTION 3: QUALITY ASSESSMENT AND OUTLIER DETECTION

Table S3: Outlier Detection Criteria

Criterion	**Description**	**Threshold**	**Quality Impact**
$R^2 < 0.3$	Very poor Gaussian fits	0.3	Elimination of inadequate fits
IQR method for FWHM	Values outside 1.5×IQR quartiles	Q_1-1.5×IQR to Q_3+1.5×IQR	Removal of statistical extreme values
Z-score > 3 for FWHM	Statistically extreme values	Z-score > 3.0	Elimination of extreme outliers
FWHM > 60 cm^{-1}	Physically implausible for zircon	60 cm^{-1}	Filter of non-physical values
Unclassified peaks	Alternative criteria	$R^2 < 0.5$ or FWHM > 50 cm^{-1}	Treatment of special cases

Note: Multiple criteria were applied sequentially to ensure complete removal of inconsistent data.

Table S4: Outlier Removal Summary by Spectral Region

Spectral Region	**Wavenumber Range (cm^{-1})**	**Initial Peaks**	**Outliers Removed**	**Final Peaks**	**% Removed**
$\nu_3(SiO_4)$	990-1020	80	0	80	0.0%
$\nu_1(SiO_4)$	965-985	61	2	59	3.3%
$\nu_2(SiO_4)$	430-450	80	1	79	1.2%
External Mode 1	195-210	80	0	80	0.0%
External Mode 3	220-230	80	0	80	0.0%
External Mode 4	350-365	80	2	78	2.5%
Total	-	461	5	456	1.1%

Table S5: Comparative Analysis Before vs After Cleaning

Spectral Region	FWHM Before (cm^{-1})	FWHM After (cm^{-1})	CV Before (%)	CV After (%)	R² Before	R² After	Final FWHM Range
ν_1(SiO$_4$)	15.15 ± 2.91	15.15 ± 2.62	17.8	16.3	0.997	0.997	[11.46 - 22.23]
ν_3(SiO$_4$)	-	13.32 ± 0.44	-	4.1	-	0.995	-
ν_2(SiO$_4$)	17.01 ± 0.63	17.03 ± 0.60	3.7	3.5	1.000	1.000	[15.25 - 18.31]
External Mode 1	-	20.26 ± 0.84	-	5.2	-	0.997	-
External Mode 3	-	16.12 ± 0.27	-	3.1	-	0.998	-
External Mode 4	12.15 ± 0.22	12.14 ± 0.20	1.8	1.6	0.988	0.988	[11.77 - 12.66]

Note: Regions with no outliers removed (ν_3, External Mode 1, External Mode 3) do not present before-cleaning statistics.

Table S6: FWHM Reference Ranges by Vibrational Mode (Literature-Based)

Vibrational Mode	Wavenumber Range (cm^{-1})	Typical FWHM Range (cm^{-1})	Physical Interpretation & Key References
ν_3(SiO$_4$)	990-1020	8-25	Principal stretching mode, highly sensitive to radiation damage. [Zhang et al. (2000): 5→>20 cm^{-1} crystalline→metamict; Nasdala et al. (2001): radiation dose correlation; Ginster et al. (2019): 4.9-17.8 cm^{-1} experimental data]
ν_1(SiO$_4$)	965-985	6-20	Secondary stretching mode. [Dawson et al. (1971): fundamental vibrational characterization]
ν_2(SiO$_4$)	430-450	15-35	Angular deformation mode, naturally broader peaks. [Gucsik et al. (2004): high-pressure effects, structural damage analysis]
External modes	195-365	10-40	Lattice vibrations, highest natural variation. [Bjerga et al. (2022): thermal history analysis; Härtel et al. (2021): external mode closure temperatures]

Table S7: Data Quality Improvement Assessment

Spectral Region	CV Reduction (%)	Improvement Assessment	Analysis Impact
$\nu_1(SiO_4)$	-1.5	MINIMAL	Small
$\nu_3(SiO_4)$	-	NOT APPLICABLE	No outliers
$\nu_2(SiO_4)$	-0.2	MINIMAL	Minimal
External Mode 1	-	NOT APPLICABLE	No outliers
External Mode 3	-	NOT APPLICABLE	No outliers
External Mode 4	-0.2	MINIMAL	Minimal

Note: The “MINIMAL” assessment indicates that the cleaning method removed only extreme outliers, preserving the natural variability of the data. This demonstrates the initial quality of the spectra and the robustness of the acquisition methodology.

SECTION 4: METHOD VALIDATION AND PERFORMANCE ANALYSIS

Table S8: Method Dispersion Analysis

Spectral Region	ΔFWHM Between Methods (cm^{-1})	ΔCV Between Methods (%)	Dispersion Level	Recommendation
$\nu_3(SiO_4)$	0.041	1.53	LOW	Any method acceptable
$\nu_1(SiO_4)$	0.260	6.64	MODERATE	Careful method selection
$\nu_2(SiO_4)$	0.066	0.80	LOW	Small differences
External Mode 1	0.028	0.23	LOW	Methods equivalent
External Mode 3	0.139	0.45	LOW	Small differences
External Mode 4	0.000	0.82	MINIMAL	Methods highly equivalent

SECTION 5: PEAK DETECTION ROBUSTNESS ANALYSIS

Table S15: Peak Detection Configuration Parameters

Parameter	Value	Unit	Purpose
Minimum height	8% of maximum intensity	%	Filter low-intensity artifacts
Minimum prominence	4% of maximum intensity	%	Ensure peak distinguishability
Minimum distance	2 points	points	Prevent double counting
Minimum width	2 points	points	Eliminate narrow spikes

Table S16: Peak Distribution by Spectral Region

Spectral Region	Peaks Detected	Percentage (%)	Mean R^2	FWHM (cm^{-1})	Expected Range Status
$\nu_3(SiO_4)$	80	16.2	0.996	13.1 ± 0.5	100% within typical range (8-25 cm^{-1})
$\nu_1(SiO_4)$	61	12.3	0.997	16.3 ± 2.9	85.2% within typical range (6-20 cm^{-1})
$\nu_2(SiO_4)$	80	16.2	1.000	17.0 ± 0.6	100% within typical range (15-35 cm^{-1})
External Mode 1	80	16.2	0.997	20.4 ± 1.1	100% within typical range (10-30 cm^{-1})
External Mode 2	0	0.0	0.000	0.0 ± 0.0	No peaks detected
External Mode 3	80	16.2	0.998	16.4 ± 0.5	100% within typical range (10-28 cm^{-1})
External Mode 4	80	16.2	0.988	12.2 ± 0.2	0% within typical range (15-40 cm^{-1}) - REVIEW
Out of regions	34	6.9	-	-	Artifact detection

Table S17: FWHM Context Analysis and Scientific Interpretation

Spectral Region	Typical FWHM Range (cm^{-1})	Observed Range (cm^{-1})	Out of Range Values	Scientific Interpretation
ν3(SiO_4)	8-25	12.1-14.4	0	Excellent crystallinity, main zircon mode
$\nu_1(SiO_4)$	6-20	11.5-23.8	9 (above)	Moderate radiation damage
$\nu_2(SiO_4)$	15-35	15.1-18.3	0	Low-frequency mode, good quality
External Mode 1	10-30	18.4-22.7	0	External lattice mode
External Mode 3	10-28	15.6-17.7	0	External rotatory mode
External Mode 4	15-40	11.8-12.8	80 (below)	Potential instrumental effect or sample characteristic

Table S19: Processing and Quality Control Summary

Parameter	Original Value	After Cleaning	Improvement
Total peaks detected	492	487	-5
Percentage of outliers removed	-	-	1.0%
Peaks retained for analysis	-	99.0%	+1.0%
Mean coefficient of variation (FWHM)	-	-	-0.6%
Global mean R^2	-	0.995	+0.000

Note: Outlier cleaning was performed using multiple statistical criteria: (i) $R^2 < 0.3$ for fitting quality, (ii) IQR method for FWHM (Q_1-1.5×IQR to Q_3+1.5×IQR), (iii) Z-score > 3, and (iv) physical criterion FWHM > 60 cm^{-1}.

APPENDIX 3

Supplementary Material

Fundamentação Física: Parâmetro de Annealing T×t e Cinética de Arrhenius

1. Introdução

Este documento estabelece a fundamentação matemática e física para o uso do parâmetro T×t (temperatura absoluta multiplicada pelo tempo de tratamento) na seleção e organização de amostras em estudos de recuperação cristalina de zircão metamíctico.

O objetivo não é substituir a descrição cinética fundamental baseada na equação de Arrhenius, mas justificar o uso de T×t como **índice empírico de severidade térmica**, adequado para análise comparativa e ordenação experimental.

2. Cinética de Arrhenius: Fundamentos

2.1 A Equação de Arrhenius

A taxa de uma reação química ou processo termicamente ativado é descrita pela equação de Arrhenius (Arrhenius, 1889):

$$k = A \cdot \exp\left(-\frac{E_a}{RT}\right)$$

Onde: - k = constante de taxa (s^{-1}) - A = fator pré-exponencial ou fator de frequência (s^{-1}) - E_a = energia de ativação (J/mol) - R = constante universal dos gases (8.314 J/mol·K) - T = temperatura absoluta (K)

2.2 Interpretação Física

A equação de Arrhenius expressa que (Arrhenius, 1889; Weber, 1990):

1. **Barreira energética:** Apenas uma fração das partículas possui energia suficiente para superar a barreira de ativação E_a
2. **Distribuição de Boltzmann:** A fração de partículas com energia $\geq E_a$ segue:

$$f = \exp\left(-\frac{E_a}{RT}\right)$$

3. **Dependência exponencial:** Pequenas mudanças em T causam grandes mudanças em k

3. Cinética de Primeira Ordem e Tempo

3.1 Equação Cinética

Para um processo de primeira ordem (como difusão de defeitos), a fração transformada α evolui como:

$$\frac{d\alpha}{dt} = k(T) \cdot (1 - \alpha)$$

3.2 Solução Integrada

Integrando para temperatura constante:

$$\alpha(t) = 1 - \exp(-k \cdot t)$$

Ou, em termos do progresso da reação:

$$-\ln(1 - \alpha) = k \cdot t = A \cdot t \cdot \exp\left(-\frac{E_a}{RT}\right)$$

3.3 O Parâmetro Cinético

Definimos o **parâmetro cinético integrado**Φ:

$$\Phi = k \cdot t = A \cdot t \cdot \exp\left(-\frac{E_a}{RT}\right)$$

Este parâmetro representa a “dose térmica” total aplicada ao sistema.

4. De Arrhenius para T×t: A Aproximação

4.1 Expansão Logarítmica

Tomando o logaritmo do parâmetro cinético:

$$\ln(\Phi) = \ln(A) + \ln(t) - \frac{E_a}{RT}$$

Reorganizando:

$$\ln(\Phi) = \ln(A) - \frac{E_a}{R} \cdot \frac{1}{T} + \ln(t)$$

4.2 Aproximação de Primeira Ordem

Para um intervalo limitado de temperaturas, podemos expandir $1/T$ em torno de uma temperatura de referência T_0:

$$\frac{1}{T} \approx \frac{1}{T_0} - \frac{(T - T_0)}{T_0^2}$$

Substituindo:

$$\ln(\Phi) \approx \text{const} + \frac{E_a}{RT_0^2}(T - T_0) + \ln(t)$$

4.3 Simplificação para T×t

Se definirmos $\beta = E_a/(RT_0^2)$ e assumirmos que as variações em T e t são da mesma ordem de magnitude relativa:

$$\ln(\Phi) \approx \text{const} + \beta \cdot T + \ln(t)$$

Para $\beta \cdot T \ll 1$ (aproximação linear):

$$\Phi \propto T \cdot t$$

Esta é a justificativa matemática para o uso de T×t como proxy do parâmetro cinético.

5. Validade da Aproximação

5.1 Condições de Validade

A aproximação $\Phi \propto T \times t$ é válida quando:

1. Intervalo de temperatura limitado: $\Delta T/T_0 \ll 1$
2. Energia de ativação moderada: $E_a/(RT_0) \sim \mathcal{O}(10)$
3. Regime linear: Longe dos extremos de conversão ($0.1 < \alpha < 0.9$)

5.2 Análise Quantitativa

Para recuperação de zircão metamíctico (Geisler et al., 2002; Capitani et al., 2000): - K (temperatura média) - eV kJ/mol (Estágio I de Geisler) -

O fator exponencial varia por:

$$\frac{k(T_2)}{k(T_1)} = \exp\left[-\frac{E_a}{R}\left(\frac{1}{T_2} - \frac{1}{T_1}\right)\right]$$

Para $T_1 = 473$ K e $T_2 = 1073$ K com $E_a = 250$ kJ/mol:

$$\frac{k(1073)}{k(473)} \approx 10^{14}$$

5.3 Limitação Importante

⚠ **A aproximação T×t NÃO captura a dependência exponencial completa de Arrhenius.**

O parâmetro T×t é útil como **índice de ordenação**, não como descritor quantitativo preciso da cinética.

---

6. Justificativa Física para Seleção de Amostras

6.1 Por que T×t funciona para ordenação?

Mesmo não sendo exato, T×t preserva a ordem relativa das amostras porque:

1. Monotonicidade: Para processos termicamente ativados, maior T×t sempre implica maior conversão (quando $E_a > 0$)

2. Separação de escalas: Diferenças de ordens de magnitude em T×t dominam sobre erros da aproximação
3. Consistência empírica: Os dados de FWHM confirmam a correlação monotônica com T×t

6.2 Verificação Experimental

Amostra	T×t (K·h)	FWHM ν_3 (cm^{-1})	Correlação
1	773	13.11	✓
10	57,315	10.90	✓
20	873,150	8.09	✓
22	∞ (ref)	7.37	✓

A progressão monotônica FWHM ↓ quando T×t ↑ valida o uso do parâmetro.

7. Comparação com Alternativas

7.1 Parâmetro de Arrhenius Completo

$$\Phi_{Arrh} = t \cdot \exp\left(-\frac{E_a}{RT}\right)$$

Vantagem**:** Fisicamente correto Desvantagem**:** Requer conhecimento de E_a, que varia por estágio

7.2 Parâmetro T×t

$$\Phi_{T\times t} = T \cdot t$$

Vantagem**:** Simples, não requer E_a**Desvantagem:** Aproximação, perde dependência exponencial

8. Conclusão

8.1 Resumo Matemático

O parâmetro T×t emerge como aproximação de primeira ordem do parâmetro cinético de Arrhenius (Arrhenius, 1889; Weber, 1990; Geisler et al., 2002):

$$\underbrace{A \cdot t \cdot \exp\left(-\frac{E_a}{RT}\right)}_{\text{Arrhenius exato}} \approx \underbrace{C \cdot T \cdot t}_{\text{Aproximação T×t}}$$

8.2 Aplicabilidade

Para **seleção qualitativa de amostras** representando diferentes estágios de recuperação:

T×t é adequado porque preserva a ordem relativa

T×t é inadequado para cálculos quantitativos de energia de ativação

8.3 Recomendação

O uso de T×t na seleção de amostras para a figura comparativa é fisicamente justificado como índice de ordenação, desde que se reconheça sua natureza aproximada.

Referências

1. ARRHENIUS, S. Über die Reaktionsgeschwindigkeit bei der Inversion von Rohrzucker durch Säuren. *Zeitschrift für Physikalische Chemie*, v. 4, n. 1, p. 226–248, 1889. DOI: https://doi.org/10.1515/zpch-1889-0416
2. *GEISLER, T. et al. Kinetics of thermal recovery and recrystallization of partially metamict zircon: a Raman spectroscopic study. European Journal of Mineralogy, v. 13, n. 6, p. 1163–1176, 2001. DOI: https://doi.org/10.1127/0935-1221/2001/0013-1163*
3. *WEBER, W. J.; EWING, R. C.; WANG, L. M. The radiation-induced crystalline-to-amorphous transition in zircon. Journal of Materials Research, v. 9, n. 3, p. 688–698, 1994. DOI: https://doi.org/10.1557/JMR.1994.0688*
4. *CAPITANI, G. C. et al. A TEM investigation of natural metamict zircons: structure and recovery of amorphous domains. Physics and Chemistry of Minerals, v. 27, n. 8, p. 545-556, 2000. DOI: https://doi.org/10.1007/s002690000100*

AI USAGE DECLARATION

During the preparation of this thesis, the artificial intelligence tool integrated in Grammarly Professional® was used for English spell checking and for more concise aggregation of information, partly in the abstract. The author reviewed and edited all AI-assisted output and takes full responsibility for the final content of this work.